

WFPC Status and Performance Changes 1990-1993

John W. MacKenty¹, Sylvia Baggett¹, John Biretta¹
Christine Ritchie¹ and William Sparks¹

I. Introduction

The Wide-Field Planetary Camera (WFPC) was built by JPL with Jim Westphal of Caltech as PI. It was launched aboard *HST* in April 1990 and returned to Earth on 13 December 1993 following its replacement with the WFPC2 camera. Operations during 3.5 years in orbit was highly successful and the data obtained include many of the highlights of the *HST* mission prior to the First Servicing Mission. Routine operation of WFPC started with the UV flooded conditioning of its Texas Instruments CCD detectors in December 1990. The Science Verification (SV) phase was completed in December 1991 which established the baseline calibration. WFPC has not had any electrical or mechanical problems.

WFPC has returned the largest quantity of data of any of the *HST* scientific instruments. Table 1 shows the numbers of exposures of various types obtained on orbit. The total number of readouts of the camera was 18265, where a single readout might include 1 to 4 CCDs (typically four).

Table 1: Usage History

Type	WFC	PC
External Target	3009	6056
Earth-Calib	2044	2892
Int-flat	1452	1840
Bias	254	223
Dark	192	190
K-spot	48	65
Total	6999	11266

Here we will review the QE_H problem and its correction with UV Flood conditioning. The effect of the UV Flood on the calibration of the instrument will also be briefly discussed. The problems posed by contamination internal to the WFPC are the main subject. Their location(s) and impact on UV observations, their long term growth and the measles and persistent measles phenomena will be addressed. Last, a history of the decontaminations performed on WFPC will be presented.

1. Space Telescope Science Institute, Baltimore, MD 21218

II. QE and UV Flood Conditioning

The WFPC contains 8 Texas Instruments 800 x 800 CCD detectors normally operated at -87°C . During construction of the camera it was discovered that these detectors have exposure history dependent flat fields (i.e. quantum efficiency hysteresis or QE). This problem can be circumvented by charging the detectors with solar UV light via a small, aft looking external mirror and light pipe. This UV Flood conditioning procedure was done once on-orbit in December 1990 and required 20 orbits of pointed spacecraft time and a major recalibration of the WFPC. It left the WFPC with a very small amount of residual QE which appears to have remained stable over the lifetime of the instrument.

Although the UV flood is quite stable when the CCD detectors are maintained at their operating temperatures, unfortunately some fraction of the UV flood is lost whenever CCDs are warmed. This fraction is a poorly understood function of both temperature and time. The WFPC CCDs are normally kept cooled except during major spacecraft safing events and decontaminations of the WFPC.

In August 1992, problems with both *HST* Magnetometers resulted in an anti-sun pointing exclusion which essentially precluded doing another WFPC UV Flood and made the preservation of the initial UV flood a high priority.

III. Effect of UV Flood on Calibration

The UV Flood conditioning has the side effect of increasing the quantum efficiency (QE) of the CCD detectors. This effect is largest between 3000\AA and 5000\AA . This both changes the photometric zero points and, more importantly, the flat field (since it is a strong function of position on the CCD detectors). Unfortunately, a partial removal of the UV Flood results in a corresponding decrease in QE (and change in the zero points and flat fields). Therefore warming the CCD detectors changes the fundamental calibration of the WFPC camera.

Various calibration programs have been undertaken to compensate for the effects of partial removal of the UV Flood. Two extensive sets of flat fields obtained from observations of the sunlit earth have been obtained; the first during SV and early Cycle 1 (both following the initial UV Flood) and the second during Cycle 3. Between these periods exposures have been obtained using the internal lamps which illuminate the backside of the shutter assembly. While not directly suitable as flat field measurements, the ratios of these images (Delta Flats) can be used to remove changes in the flat fields. As these lamps are fairly faint and red, only a limited subset of filters was observed (i.e. broad and medium band filters starting at F439W and longwards). The photometric zero point has been monitored monthly at centers of W2 and P6 in F336W, F439W, F555W, and F785LP (and also F230W and F284W as contamination monitors).

IV. Contamination: Location and Impact on UV Science

Contaminants intrinsic to the WFPC instrument were discovered during Thermal Vacuum testing on the ground prior to launch of *HST*. While significant problems with H₂O ice were overcome, larger molecular contaminants remained as a problem. The CCD detectors in the WFPC are located in camera head assemblies. The CCDs are packaged in 0.1 atmospheres of argon with a field flattening MgF optic 6 mm in front of each CCD. Both the CCD and this window are essentially isothermal and are normally maintained at -87°C . The contaminants are understood to be deposited on the outside (front) surface of this window and to originate from a variety of (poorly determined) locations within the WFPC enclosure (e.g. circuit boards, motor windings, etc.).

It is possible to temporarily remove these contaminants from the windows by warming the CCDs and their camera head assemblies to ~ -10 to $+20^{\circ}\text{C}$. The contaminants will return with a ~ 50 percent decline in sensitivity per day at 1500\AA which seriously limits the UV performance of the WFPC. Decontaminations are undesirable both because of calibration changes and the eventual loss of the (after August 1992 irreplaceable) UV Flood.

V. Contamination: Long Term Growth and Measles

In addition to the problems the contaminants pose for UV observations, their continued accumulation on the windows over several months attenuates light at visible wavelengths. Monthly monitoring of spectrophotometric standards stars is shown in Figure 1. The vertical lines mark the times when the instrument was decontaminated. In addition to the changes in photometric zero points, the contamination causes changes in the effective shape of the passbands (especially F336W and F439W). There is also an increase in the degree of scattered light within the instrument as shown in Figure 2. These trends show that the contaminants build up over time in a monotonic and somewhat repeatable fashion. They appear to be uniform when deposited slowly and do not result in any obvious image structure.

However, a safing of the *HST* can result in loss of power to the WFPC TECs with the camera heads warming to $\sim -35^{\circ}\text{C}$ on the order of 1 hour. Repeated experience has shown that re-cooling camera heads to their -87°C operational temperature leaves a residual contamination in the form of small particles. These result in images covered with small features which were named measles. They sufficiently modulate the MTF and degrade the PSF to the point that WFPC is basically unusable with post safing measles.

Procedures were developed to decontaminate WFPC after periods with the TECs off or when the contaminant buildup limited science observations in the F336W (U) band. These procedures attempt to remove the measles, restore visible light throughput, and cause a minimum loss of UV Flood.

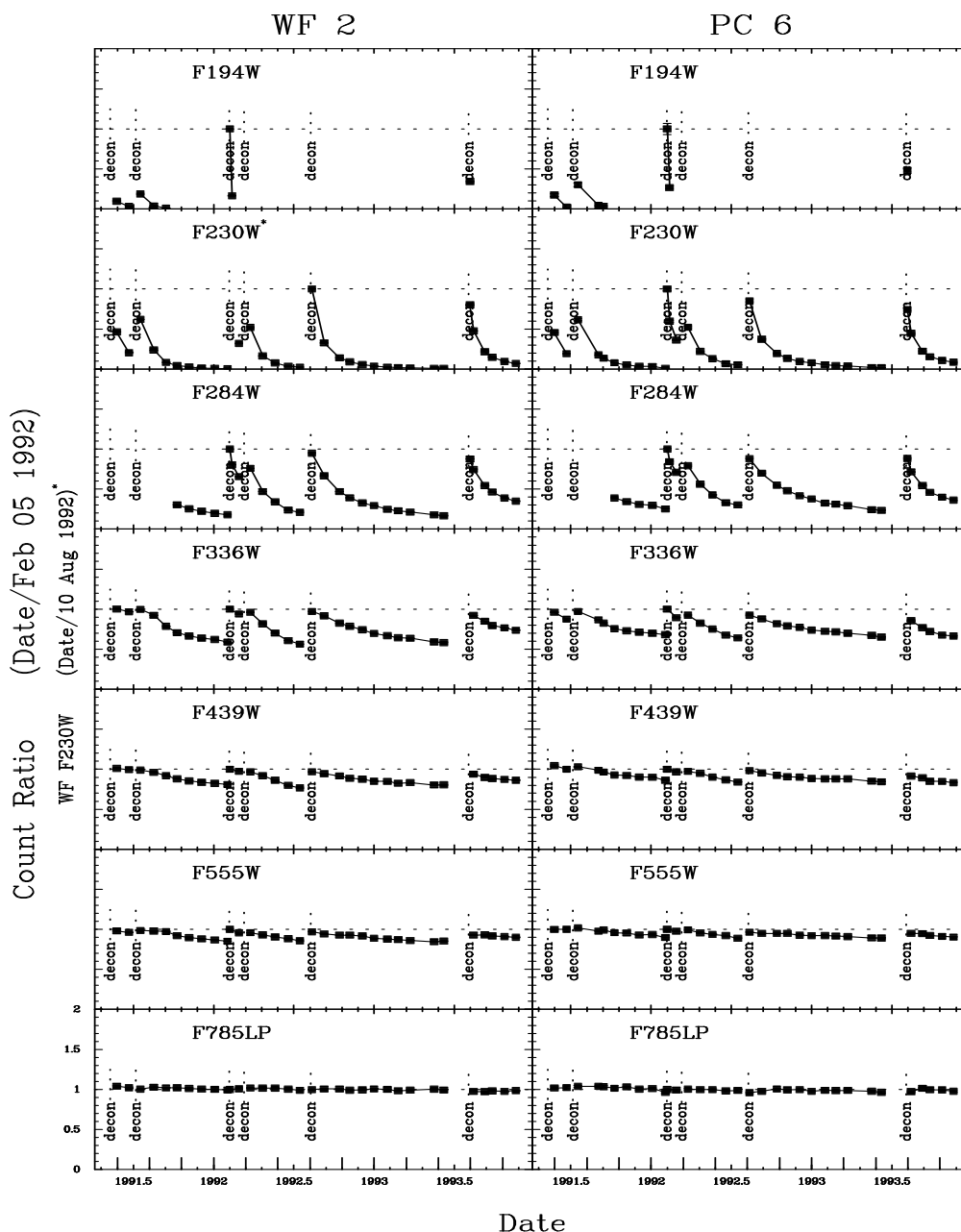


Figure 1: Results from repeated observations of the spectrophotometric standards to monitor the level of contamination of the WFPC.

VI. Contamination: Persistent Measles

Routine decontamination in February 1992 restored UV throughput but left a residue of faint (<<post-safing) measles. Three additional decontaminations, including an alternate procedure designed by JPL, did not remove these persistent measles and they appear to be stable over time. Figure 3 shows a 100 x 100 region of the P6 and P8 detectors (divided by a pre-persistent measles internal flat) at 4 epochs. The third from the left is subsequent to an *HST* safing and illustrates the post-safing measles.

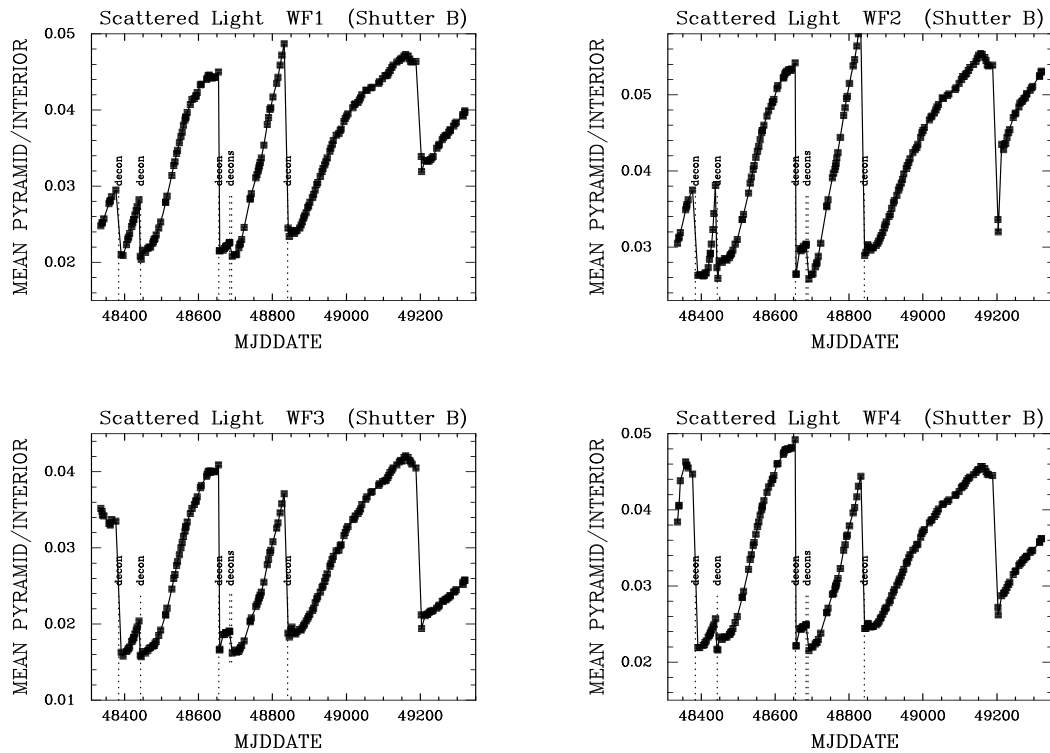


Figure 2: Scattered light changes within the instrument.

The persistent measles exhibit significant variations between the detectors. They are most pronounced on P7, P8 and least on P6 (with P5 and the WFC detectors having intermediate degrees of contamination). With a uniformly illuminated source (i.e. flat field) they produce a 1.1 percent rms modulation with a 4 to 5 percent peak amplitude in their cores. Optical modelling finds them to be consistent with 10 - 15 micron sized particles on the windows.

A probable origin of persistent measles is the usage of the pyramid motor without a sufficient cool down period between motions. This principally occurred during the SV flat field observations (4th QT 1991); the waiting period between pyramid motions has been increased after the problem was recognized.

The effects of the persistent measles on image quality cannot be fully corrected because they are on an out of focus surface. (The same is true of dust and scratches on the windows and the pyramid.) The Delta Flats can be used to locate persistent measles and may achieve a partial correction for extended targets (i.e. targets with similar illumination of the windows as the flat fields). The persistent measles pose significant difficulties for deconvolution since their dimensions are comparable to the PSF. The science programs most impacted are high S/N observations of structures (e.g. planetary atmospheres), large field-of-view observations (where the target cannot be placed on a relatively clean place on the camera — e.g. the center of P6), and precision photometry and astrometry (already difficult due to the spherical aberration).

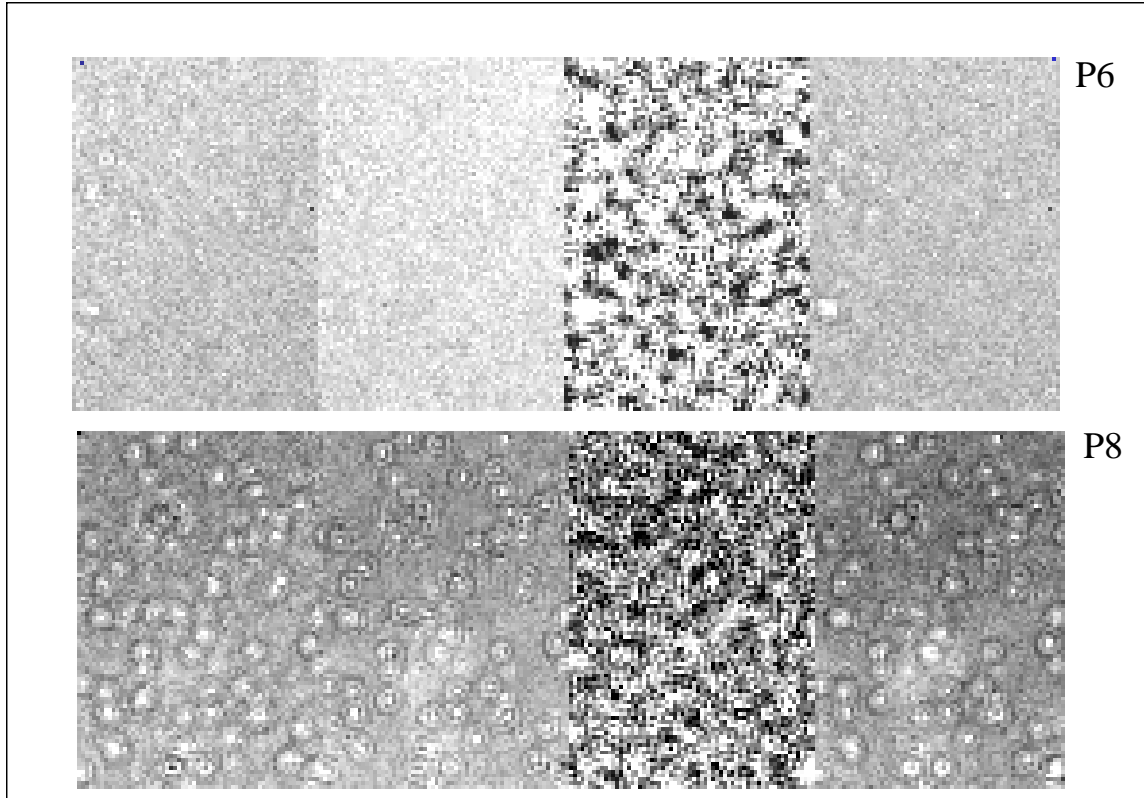


Figure 3

An extensive engineering analysis at GSFC, JPL, and STScI concluded that the removal of the persistent measles was probable if a high temperature ($\sim+20\text{C}$) decontamination was performed. However, such a decontamination would result in loss of the UV flood (which had become irreplaceable) and this was not seen as an acceptable trade-off.

VII. Major Events in the WFPC Operation History

Following the UV Flood conditioning of WFPC at the end of December 1990, the state of the instrument changed a number of times due to *HST* safings and planned decontaminations. A brief history of these is included in Table 2.

Table 2: History of WFPC Safings and Decontaminations

Date (Year.Day)	Event
1991.002	-20°C (mini-lowtemp) after safe
1991.026	-82°C (de-ice) attempt to remove "daisies"
1991.028	-20°C (mini-lowtemp) removed daisies and created measles
1991.029	-15°C (lowtemp) removed measles
1991.122	-35°C (80 hours) during PSEA safe created measles
1991.128	+12°C (hot junction) removed measles
1991.184	-25°C (7 hours) during WFPC safe created measles
1991.186	+6°C (flash) removed measles
1992.034	-2°C (flash) planned decontamination created persistent measles
1992.035	0°C (flash) slight decrease in measles
1992.063	-4°C (mod hot junction) no changes
1992.068	+4°C (warm flash) no changes
1992.212	-35°C PSEA safing created measles
1992.220	+2°C (flash) removed measles; persistent measles unchanged
1993.214	0°C (flash) planned decontamination restored UV and decreased scattered light; slight changes in persistent measles

The WFPC Calibration Pipeline

John A. Biretta¹, Sylvia M. Baggett¹, John W. MacKenty¹,
Christine E. Ritchie¹ and William B. Sparks¹

Abstract

We review the basic functions of, and major changes to, the WFPC calibration pipeline. Known bugs and errors are described. Finally, we summarize situations where later re-calibration might give some improvement over the pipeline calibration.

I. Introduction

The purpose of the WFPC calibration pipeline is to provide an initial calibration of data immediately after each observation is made. The level of calibration is that which is *routinely available at the time of the observation*. The necessity of calibrating every frame in near real time means that little consideration can be given to the science goals of each individual proposal. Observers with unusual programs, or with programs requiring an extremely accurate calibration, may find they need to tailor the calibration to their individual science goals. Furthermore, the calibration algorithms and reference files are routinely updated, so there will be many situations where later re-calibration gives a better result than could be obtained immediately after the observation.

II. Post-Observation Processing and the Calibration Pipeline

There are many important data processing steps which lead up to the actual pipeline calibration. We briefly summarize the more prominent ones here. After readout of the WFPC CCDs, the data initially reside on one of two tape recorders on-board the *HST*. At pre-scheduled times a high baud rate forward link is established between *HST* and a TDRSS satellite, and the tape recorder is then dumped via TDRSS to a ground station at White Sands, NM. The data are recorded there, and then transmitted to STScI via NASCOM satellite. The data arrive at STScI in the form of packets of spacecraft data, wherein the WFPC images are interspersed with other *HST* telemetry, data from other science instruments, and the like.

The Post-Observation Data Processing System (PODPS) assembles raw WFPC images from the spacecraft packets. An assembled raw WFPC data set consists of several headers and data files whose type are indicated by the file name suffix, as shown in Table 1.

1. Space Telescope Science Institute, Baltimore, MD 21218

Table 1: File Name Convention for WFPC Data

Suffix	File Contents	Size (Data Type)
.D0H	Raw image header	(ASCII)
.D0D	Raw image	800x800x4 pixels (I*2)
.Q0H	Data quality file for raw image header	(ASCII)
.Q0D	Data quality file (DQF) for raw image	800x800x4 pixels (I*2)
.X0H	Raw engineering data header	(ASCII)
.X0D	Raw engineering data (includes CCD overscan columns)	14x800x4 pixels (I*2)
.Q1H	DQF for raw engineering data (header)	(ASCII)
.Q1D	DQF for raw engineering data	14x800x4 pixels (I*2)
.SHH	Standard header packet	(ASCII)
.SHD	Standard header packet binary data	965 (I*2)

Each data set is named with a unique prefix which contains an encoded proposal number, spacecraft alignment number, and exposure number. For example, a file name W13L0103t.D0D indicates: W = WFPC data; 13L = sequential executed proposal number encoded in base 36; spacecraft alignment number 01 for this proposal; frame number 03 of this alignment; 't' indicates data path (i.e. tape recorder); and finally .D0D indicates the file contains a raw image.

Once the raw files are assembled, PODPS sets a number of keyword parameters in the header files (.D0H files) which control the pipeline calibration. These parameters include YES / NO switches, as well as the names of the calibration files to be used. Table 2 shows an excerpt of a .D0H header file prepared for calibration.

Table 2: Example of calibration control header keywords in a .D0H file. Note the suffixes on the reference file names (e.g. .r0h) which are specific to each file type.

```

Keyword = Value / Explanation
MASKCORR= 'YES ' / Do mask correction: YES, NO, DONE
ATODCORR= 'YES ' / Do A-to-D correction: YES, NO, DONE
BLEVCORR= 'YES ' / Do bias level correction: YES, NO, DONE
BIASCORR= 'NO ' / Do bias correction: YES, NO, DONE
PREFCORR= 'NO ' / Do preflash correction: YES, NO, DONE
PURGCORR= 'NO ' / Do purge correction: YES, NO, DONE
DARKCORR= 'NO ' / Do dark correction: YES, NO, DONE
FLATCORR= 'NO ' / Do flat field correction: YES, NO, DONE
DOSATMAP= 'NO ' / Output Saturated Pixel Map: YES, NO, DONE
DOPHOTOM= 'NO ' / Fill photometry keywords: YES, NO, DONE
DOHISTOS= 'NO ' / Make histograms: YES, NO, DONE
OUTDTYPE= 'REAL ' / Output image datatype: REAL, LONG, SHORT
MASKFILE= 'bb615191w.r0h' / name of the input DQF of known bad pixels
ATODFILE= 'c2614032w.r1h' / name of the A-to-D conversion file
BLEVFILE= 'wcal$w13l0103t.x0h' / Engineering file with extended register data
    
```

BLEVDFIL= 'wcal\$w13l0103t.q1h' / Engineering file DQF
BIASFILE= 'wref\$c261403gw.r2h' / name of the bias frame reference file
BIASDFIL= 'wref\$c261403gw.b2h' / name of the bias frame reference DQF
PREFFILE= 'wref\$c8e0939jw.r3h' / name of the preflash reference file
PREDFIL= 'wref\$c8e0939jw.b3h' / name of the preflash reference DQF
PURGFILE= 'wref\$9ck1027hw.r4h' / name of the purge reference file
PURGDFIL= 'wref\$9ck1027hw.b4h' / name of the purge reference DQF
DARKFILE= 'wref\$c5t10337w.r5h' / name of the dark reference file
DARKDFIL= 'wref\$c5t10337w.b5h' / name of the dark reference DQF
FLATFILE= 'wref\$a1b0845dw.r6h' / name of the flat field reference file
FLATDFIL= 'wref\$a1b0845dw.b6h' / name of the flat field reference DQF
PHOTTAB = 'wtab\$c7e13087w.cw0' / name of the photometry calibration table

Once the .DOH header is properly set, PODPS performs the actual calibration by running the program CALWFP. This is identical to the CALWFP program in the STSDAS package, so observers can perform the same calibration outside the STScI pipeline.

III. Major CALWFP Pipeline Operations

We now describe the individual calibration steps which can be performed by the pipeline. The normal situation is to perform nearly all these steps. But observers can choose to perform only a subset by setting the appropriate switches to "NO" in the .DOH file and running CALWFP again. The steps are: mask correction, A-to-D correction, bias level subtraction, bias image subtraction, preflash subtraction, CTE correction, residual image correction, dark current subtraction, flat-field correction, and filling of the photometry keywords.

Mask Correction. This step merely marks known bad pixels in the data quality file (DQF) for the output image. It does not alter the data image itself.

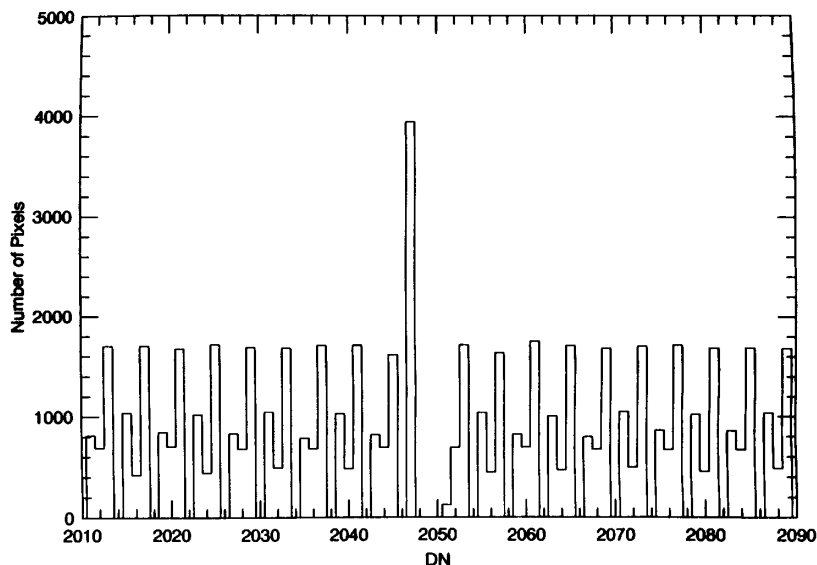


Figure 1. Histogram of digitized pixel values (DN). From Lauer 1992.

A-to-D Correction. A problem in the WFPC “sample and hold” circuitry causes stray signals to corrupt the analog-to-digital conversion process. The result is that some A-to-D converter bits fail to set, which causes a negative bias on the digital output values. The effects can be readily seen in a histogram of output digital values (Figure 1). Instead of a smooth, uniform distribution of digital values, some values are totally absent, while others occur much too often.

This problem impacts science data in two ways: First, many pixel values are systematically too low by an amount of order 1 DN. This can easily be corrected by reassigning pixel values to slightly higher values, and this is what is done during pipeline calibration. A simple look-up table is used to reassign the pixel values based on their raw values. Figure 2 illustrates this process. A second impact is that information regarding the true analog value has been lost, hence noise is effectively added to the data. This increased noise cannot be corrected.

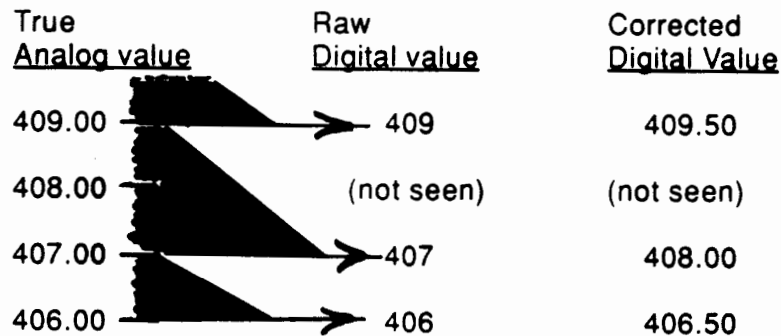


Figure 2: Example of A-to-D correction showing true analog values, raw digital values, and corrected digital values.

Bias Level Subtraction. The purpose of this step is to remove a uniform zero-level offset voltage, or bias level, from the images. The even and odd CCD columns have slightly different bias levels, the difference being about 1 DN. Early in the WFPC observation program it was noticed that this difference changes sign when the WFPC electrical power is interrupted (i.e. during hardware safemode events, etc.). Figure 3 illustrates typical bias levels as a function of CCD column for three different dates.

In February 1992 a change was implemented in the pipeline, wherein separate bias levels are determined, and applied to, the even and odd columns. The two levels are determined from the CCD overscan lines in the .X0D file for each data set. These levels are then subtracted from the image, and recorded in the .C0D file binary header keywords BIASODD and BIASEVEN for each image group (CCD), and may be examined with IRAF task IMHEAD. Note that the name of the header files, .X0H and .C0H, must be specified in IRAF to examine the .X0D and .C0D files, respectively.

Bias Image Subtraction. The purpose of this step is to remove small pixel-to-pixel variations in the zero level, or bias level, which is caused by the CCD readout electronics. Typical features in the bias image include high regions (up to 12 DN high) near the CCD edges; broad bars extending in the row direction on the CCDs which are ~0.05 DN high; and faint ripples with an amplitude of a few times 0.01 DN which are at a small angle to the CCD row direction. Features in the bias frames

have been very stable with time; exceptions are a small region in the corner of WF1 which has varied by ~ 0.1 DN, and a few new hot pixels which are intense enough to appear in the bias frames.

The bias calibration image is an average of a number of ~ 43 second exposures taken with the shutter closed. Early during operation of the pipeline, an average of 18 such on-orbit bias frames was used for calibration. In August 1993 an improved bias calibration image was installed which was the average of 47 on-orbit frames for the WF, and 43 for the PC. These improved bias calibration frames have an RMS noise of about 0.25 DN, and will reduce the noise contributed by calibration, which may be significant if large numbers of science data frames are averaged together.

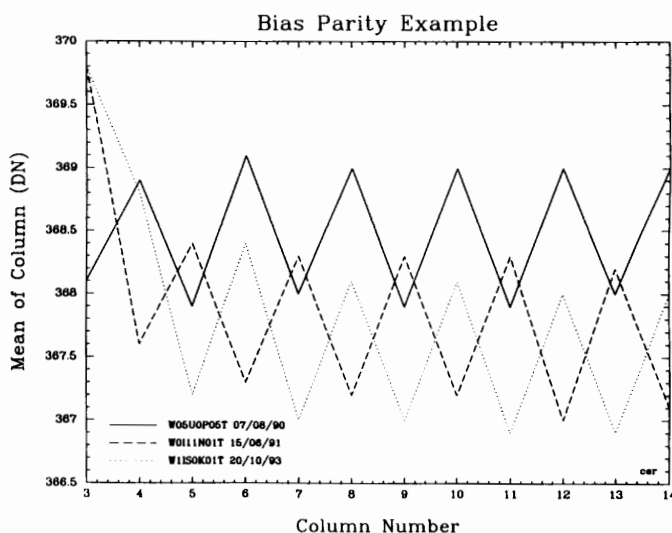


Figure 3: Bias level (in DN) as a function of column number in three typical .X0H files. Observation dates are shown.

Preflash Image Subtraction. Faint images (< 200 electrons per pixel) have poor charge transfer during readout, which causes tails to appear on images in the column direction. To reduce this effect, images can be preflashed with a small amount of light using faint lamps shining on the back of the WFPC shutter blades. Typically images are preflashed to about 50 electrons per pixel, which is sufficient to reduce the tails while only slightly increasing the noise. The purpose of preflash calibration is to remove this faint illumination pattern from the science images.

The preflash illumination pattern is fairly uniform, but does contain a number of features. These include a broad pattern from non-uniform illumination of the shutter blades, and large features associated with markings on the shutter blades. There are also small numbers of hot pixels which are sufficiently intense to appear during the minute or so it requires to perform the preflash. The preflash images have been quite stable, with only a broad region on PC5 showing variations ~ 0.04 DN. There are also new hot pixels which appear over time. Since the preflash is performed with a $\lambda = 1 \mu\text{m}$ filter in place (F1042M or F1083N), they are relatively immune to variations in contamination and quantum efficiency.

The images used to calibrate and remove the preflash pattern are averages of on-orbit preflash exposures made without opening the shutter. Separate calibration images are made for the “A” and “B” shutter blades, since their reflectivities are slightly different. These calibration files are finally scaled to a preflash time (duration of preflash lamp being on) of 1 second.

The science data images are preflash calibrated by first deciding which shutter blade was in place during the preflash. This information is usually stored in the SHUTTER keyword of the .D0H header file by PODPS. (Otherwise it can be determined by running STSDAS tasks ENGEXTR on the .X0H file to construct an IRAF table, which is then displayed with TPRINT, also in STSDAS. Rows 85 and 86 of the table contain the SHUTOPNB and SHUTOPNA keywords, with “open” indicating that shutter was in place at the *start* of the exposure, and hence used for the preflash. This only applies to external observations with one exposure per CCD readout. For exposures of 300 seconds or longer taken before November 1993, it is not possible to determine the preflash shutter blade from the image header information. Instead, this must be determined from the shutter motion in exposures prior to the one in question. Statistically speaking, shutter B is most often used to preflash these exposures, and this is what the pipeline assumes in routine processing.) The correct reference file for that shutter is then multiplied by the preflash duration in seconds (PREFTIME header keyword), and the scaled reference file is finally subtracted from the science data. The preflash durations are 30 seconds for WF images, and 8 seconds for the PC format.

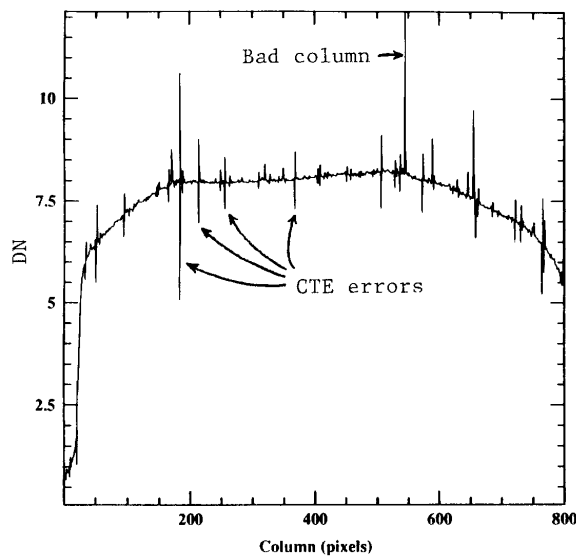


Figure 4: A preflash calibration file for WF1 which has been averaged along the columns, and which shows the typical pattern of adjacent low and high CCD columns.

For much of the WFPC history, the preflash calibration files were the averages of about 10 frames taken early in the mission. In August 1993 an improved, low-noise preflash calibration was installed. The improved WF calibration uses the average of 36 frames for the B shutter. For the A shutter, only 12 on-orbit frames were available, so a low-noise calibration reference file was constructed by using low spacial frequencies from the A blade, and high spacial frequencies from the B blade data.

The PC calibration frames were constructed in a similar manner. These improved files have about half the noise of the older files (~ 0.35 DN RMS), and will reduce the noise in situations where many science images are averaged together. We also removed the hot pixels, since they vary with time.

Charge Transfer Error (CTE) Correction. The WFPC CCDs have several columns where charge lags behind during the horizontal readout, due to charge transfer problems in the horizontal (or serial) readout register. These columns show a typical signature where the count levels are low by about 1 DN, with the following column being high by an equal amount. See Figure 4. The amount of charge which lags behind is insensitive to the exposure level, provided it exceeds a few DN, and is constant along the entire column.

For images which are preflashed, the preflash subtraction automatically corrects for this effect, since it is present in both the preflash calibration image and the science image. For images which are not preflashed, it is still useful to remove the column pattern caused by the CTE effect. In practice, the correction is derived from the preflash calibration images, by averaging along the columns, and then removing the broad illumination patterns, so that only column-to-column variations on scales of a few pixels remain. This correction is then stored in the first row of each preflash calibration frame. The CTE correction will be applied by the CALWFP when the control parameters are set as: PREFCORR = YES, PREFFILE = [normal preflash calibration file name], and PREFTIME = 0. For these settings, CALWFP will subtract the CTE correction from each image column, rather than the preflash image itself. This CTE correction is stored in the first row of the preflash reference file image.

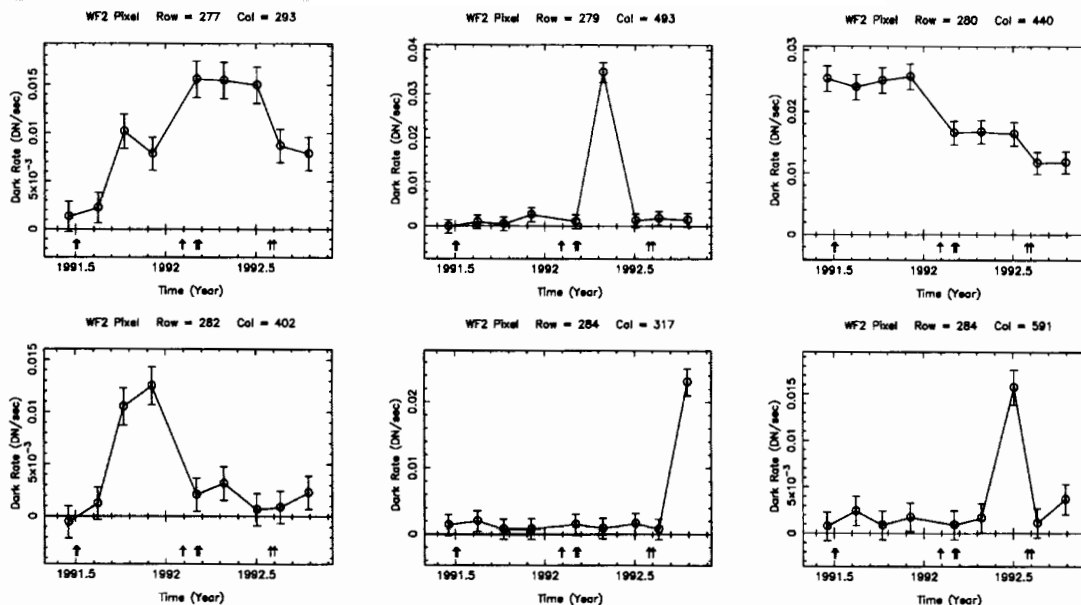


Figure 5: Evolution of dark count rate as function of year for six typical hot pixel pixels on CCD WF2. Vertical arrows indicate CCD decontaminations

Unfortunately, a bug in PODPS has caused PREFCORR to be set to NO for images which are not preflashed, so that, in effect, the CTE correction is never applied by the pipeline. Observers with non-preflashed images of faint targets may wish to perform the CTE correction themselves, by setting the preflash control parameters as above

in the .DOH files, and then running CALWFP again on their data.

Residual Image Correction. The pipeline contains a facility for removing residual images caused by prior over-exposures of the CCDs. This feature has not been used, both because the CCDs are operated above the originally proposed temperature, and because the spherical aberration has resulted in fewer extreme over-exposures.

Dark Current Subtraction. The purpose of this calibration is to remove dark current from long exposure science images. The dark current has several components: a quasi-uniform background around 0.001 DN/sec/pixel; large numbers of “warm” pixels; and several hundred “hot pixels” (>0.01 DN/sec). The pattern of hot pixels is known to vary with time; about 30 new hot pixels appear per CCD per month, while about 30 percent are abruptly lost during decontaminations (Figure 5). There are also a few hot pixels per CCD which flicker on time scales of hours, and cannot be calibrated.

The calibration reference files are constructed from either ~1440 or ~1740 sec duration on-orbit, pre-flashed exposures taken with the shutter closed, and through “crossed” filters to eliminate any light leaks. Typically about ten such frames are calibrated, averaged, and then scaled to 1 second of darktime, to form a dark calibration reference file.

These calibration reference files are then applied by computing the darktime of the science exposure, scaling the reference file by this darktime, and then subtracting the scaled reference file from the data. The darktime is defined as the period of time during which dark current collects, and in practice is the interval between the initial erase of a CCD and the start of its readout. PODPS uses an approximation which is accurate to about 1 minute, and stores this value in the DARKTIME keyword of the .DOH file:

$$\begin{aligned} \text{DARKTIME} &= (\text{exposure time}) + 1 \text{ min} \\ &+ 2 \text{ min (if preflashed)} + 1 \text{ min (if two filters used)} \end{aligned}$$

In situations requiring more accurate dark calibration, observers may wish to re-calibrate using a more accurate darktime estimate. (See Appendix 2 of Biretta, Ritchie, and MacKenty 1993). We note that science images taken with the serial clocks on (CLOCKS=YES; usually for very bright targets) will require a different dark calibration, since the serial clocks modify the dark pattern near the top and bottom of the CCDs, and alter the dark time, as well.

During 1993 we modified the strategy used for dark calibration. Before January 1993 a single dark calibration reference file was used for each CCD, without regard to the observation date. Beginning in January 1993, we went to a new strategy which attempts to minimize the time variations. We generated a new series of calibration reference files, with each file covering a 6 to 12 month period between decontaminations since launch. Further improvements were made in June 1993, when we increased the rate of on-orbit dark calibration exposures from 2 per month to 12 per month, and began delivering monthly dark calibration files.

A known problem with the PODPS dark calibration occurs for exposures which are

interrupted due to loss of guidance system lock, and the like. In these situations, the shutter closes for a brief period of time, but dark current continues to collect. The bug is that PODPS only used the shutter open time, in computing the darktime. Exposure interruptions may be indicated by the EXPFLAG header keyword (though a bug often caused this to be set to NORMAL instead of INTERRUPTED), by unequal values of the WEXPODUR and EXPTIME keywords, and by keyword NSHUTA17 being greater than one.

Flat Field Correction. The purpose of flat field correction is to bring all detector pixels to the same photometric response. This step removes pixel-to-pixel variations in the CCD response, patterns imposed by the filters, optical vignetting, etc.

Each filter / camera combination requires its own calibration reference files. These files are constructed from exposures of the bright earth taken through the filter in question, with a neutral density filter sometimes being used as well. These raw earth-cal frames contain streaks due to the combined effects of spacecraft motion and earth features. The STREAKFLAT code in STSDAS is used to remove the streaks by combining images taken at different streak angles. The combined de-streaked image is then normalized so that all CCDs average to unity, and is finally inverted (1 / image) before being installed in the pipeline. Science images are calibrated simply by selecting the reference file for the appropriate filter / camera, and multiplying the reference file into the data.

Most of the currently available (Dec. 1993) flats were observed between July 1991 and January 1992, and are referred to as either the SV flats or Cycle 1 flats, depending whether they were compiled by the IDT or STScI. In some cases more than one flat is available, where either different raw frames were used, or where earth-cals were taken both with and without a neutral density filter. We have just completed observing 1300 earth-cals as part of the closure calibration, and new flat field reference files should be available early in 1994.

The flat-field calibration, and its short-comings, are the topic of several other papers in this volume.

Filling of Photometric Keywords. This final step merely copies photometric information from a look-up table into the .COD file binary header, but does not alter the image itself. CALWFP examines the image header, sets the PHOTMODE keyword, searches the photometry look-up table (PHOTTAB) for a matching PHOTMODE, and copies this information into the photometry keywords. For example, PHOTMODE="PC,5,F,DN,F1042M,OPEN,CAL" indicates that detector PC5 was used, a calibration in flux units (F) is desired, the raw data are in DN, the filters were F1042M and OPEN (no second filter), and CAL indicates the data were flat-fielded. The matching PHOTMODE entry in the photometry table is then located, and the numbers are copied into the following keywords of the .COD binary header:

PHOTFLAM: inverse sensitivity, defined as F_{λ} in $\text{erg cm}^{-2} \text{sec}^{-1} \text{Angstrom}^{-1}$ for a count rate of 1 DN sec^{-1} .

PHOTZPT: zero point magnitude (Space Telescope Magnitude at $F_{\lambda}=1$).

PHOTPLAM: pivot wavelength for the filter in Angstroms.

PHOTBW: RMS filter bandwidth in Angstroms.

These keywords may be subsequently examined with IMHEAD in IRAF. Separate papers will present more discussion of WFPC photometry.

Summary of Image Calibrations. The above image calibrations may be summarized in a single equation:

$$\begin{aligned} \text{Calibrated image (.COD file)} &= (\text{flat field reference file}) \times \\ &[\text{A-to-D (raw .DOD image file)} \\ &\quad - (\text{bias level correction}) \\ &\quad - (\text{bias reference frame}) \\ &\quad - (\text{preflash reference frame}) \times (\text{PREFTIME}) \\ &\quad - (\text{dark reference frame}) \times (\text{DARKTIME})] \end{aligned}$$

IV. Output of the Calibration Pipeline

The calibrated output from the pipeline consists of the headers and data files shown in Table 3. The calibrated data appear in the .COD files, and the data quality is indicated by the .C1D files. The histograms can be optionally output by setting the DOHISTOS keyword.

We also include a note regarding the data quality files, or DQF files. These are used to track problems occurring during the observations, data transmission, or calibration, which might adversely affect the science data. The DQF files are 16-bit integer images, and the pixel value bits are set to indicate problems. A setting of all bits to zero (i.e. pixel value zero) indicates good data. Setting of different bits indicates different problems, as shown in Table 4.

Table 3: Calibrated WFPC Data Files

Suffix	File Contents	Size (Data Type)
.C0H	Header for calibrated image	(ASCII)
.C0D	Calibrated image	800x800x4pixels(R*4)
.C1H	Data quality file for calibrated image (header)	(ASCII)
.C1D	Data quality file for calibrated image	800x800x4 pixels (I*2)
.C2H	Histograms of calibrated images (header)	(ASCII)
.C2D	Histograms of calibrated images	4096x3x4 pixels(I*4)
.CGR	ASCII copy .C0D binary header info. (group parameters keywords)	(ASCII)
.TRL	PODPS history text	(ASCII)

Table 4: DQF pixel bit settings and problems they indicate

Image Bit	Problem indicated
1's bit	Reed Solomon corrected pixel
2's bit	Poor calibration (variable hot pixel, bias, or preflash level; not enough preflash, poor flat fielding, etc.)
4's bit	Permanent CCD defect.
8's bit	A-to-D converter saturated (>4095 DN in raw image).
16's bit	Data lost during transmission to ground. These pixels are usually filled with value -100 DN
32's bit	Data bad for other reason.

V. When is the Post-Pipeline Re-Calibration Useful?

There are many situations where observers may be able to improve upon the standard pipeline calibration. Whether it is worthwhile to perform such re-calibration will depend on the nature and science goals of the observations. Observations of bright targets (planets, bright galaxy nuclei, star clusters) are likely to be limited by the accuracy of the flat fielding. On the other hand, very deep exposures of faint stars of galaxies are likely to be limited by the dark current and noise, including readout noise and noise in the bias and preflash calibration files.

The centers of the default detectors, WF2 and PC6, are already relatively flat, so for small targets there, the pipeline flat fielding is probably good to a few percent, and very little improvement beyond this can be expected. For larger targets covering all four CCDs, there are various problems limiting the accuracy of flat fielding, with errors in the most serious cases near 20 percent. One major problem is that many broadband pipeline flats are taken through neutral density (ND) filters, which impose their own pattern on the flattened data. For some filters, flats have been taken both with and without neutral density filters, and it might be worthwhile to re-flatten using alternate flats lacking the ND filter. Another approach is to flatten the data with narrow band filter flats at nearby wavelengths, which are taken without ND filters, because of their lower throughput. Or alternatively, to derive the ND filter pattern using narrow band filter flats, and then to remove this pattern from the science data.

At short wavelengths (<5000 Angstroms), the measles contamination pattern can cause localized flat field errors exceeding 5 percent. The measles are perhaps best dealt with by using DELTAFLATS (MacKenty and Baggett 1992) to locate these artifacts, and then deciding whether they impact the location of the science target on the CCDs. The DELTAFLATS can also be multiplied into the science data as a correction, but they are likely to make only a partial correction due to differing illumination patterns of the flat and science data.

We hope to remedy some of these problems in creating the closure flats, which will be available in early 1994, so that re-calibration at that time might give some improvement in the flat fielding.

In order to obtain an optimal dark current calibration, it is necessary to know the dark current both before and after the science observation, so that a reasonable interpolation can be made to eliminate the time variations. Hence, the dark reference files used for pipeline calibration immediately after the observations are never quite optimal. In cases where the dark current is a serious limiting factor, it would be worthwhile to re-calibrate later, when a better reference file is available for that epoch. It would also be possible to tailor-make a dark calibration to the exact observation date, though that task is left to the observer.

In situations where large numbers of science exposures are averaged (≥ 4 frames), the new low-noise bias and preflash calibration files should give an appreciable reduction in noise. For example, an average of 4 preflashed exposures will have the noise reduced by ~15 percent, and for 10 exposures reduced by ~28 percent. In these cases it may be worthwhile to re-calibrate with the new reference files.

VI. Further Information

Additional information regarding the WFPC calibration pipeline may be found in:

- Calibration reference file header history texts. These contain descriptions of how the reference files were derived.
- Selected WFPC Instrument Science Reports and Memos, available from STScI Science Instruments Branch.
- Space Telescope Electronic Information Service (STEIS) Memos, which are available by anonymous FTP to internet node stsci.edu. These contain up-to-date information on calibration reference files, and the like.
- STSDAS Calibration Guide, available from STScI User Support Branch.
- WFPC Handbook, available from STScI User Support Branch.
- WFPC Final Orbital / Science Verification Report, 1992, ed. S. Faber, available from STScI User Support Branch.
- WFPC Instrument Science Reports and Memos, available from STScI Science Instruments Branch.
- HST Data Handbook, available from STScI.
- WFPC Data Products Guide, available from STScI Research Support Branch.

VII. References

Biretta, J.A., Ritchie, C. E., and MacKenty, J. W. 1993, The Evolution and Treatment of Hot Pixels in the WFPC, WFPC Instrument Science Report 93-01.
Lauer, T. 1992, in WFPC Final Orbital / Science Verification Report, ed. S. Faber.
MacKenty, J. W. and Baggett, S. B. 1992, Measle Contamination and Compensation with Delta Flats, (WFPC Instrument Science Report 92-04).

WFPC Observed PSF Image Library

S. Baggett¹ and J. MacKenty¹

Abstract

Wide Field Planetary Camera (WFPC) point spread functions (PSFs) are briefly discussed and the contents of the WFPC PSF Image Library are described. Details of the processing and extraction of PSF images from WFPC observations are given and the header format is presented. The filter and chip coverage are summarized along with a description of the original data used as a source for the PSFs. A complete list of all PSFs in the Library is included in the Appendix.

I. Introduction

With the current spherical aberration, PSF images for the WFPC have become an essential element in the deconvolution of WFPC data. The *HST* PSF is known to have a sharp 0.1 arcsec radius core which contains only about 15 percent of the energy, while the remaining 85 percent is contained within broad wings which extend out to about 4 arcseconds. In addition, the WFPC PSF is 1) position dependent due to camera vignetting, 2) wavelength dependent due to diffraction effects, and, 3) dependent on the telescope's focus position (see Burrows et al., 1991). Thus, one would ideally like to obtain observed PSFs in a gridwork of positions on each chip, for all filters used and close in time to the observations requiring deconvolution. Longer exposures are required for sufficient signal to noise in the wings, however shorter exposures are needed to avoid having the sharp core of the PSF saturate the cameras. For these reasons, model PSFs will generally be required in addition to the available observed PSFs. For producing model PSFs, the STScI Telescope Image Modelling Package or TIM (Burrows and Hasan, 1993; and this volume) is available, however, it was not specifically designed for computing deconvolution PSFs and is fairly slow. Another software package, Tiny Tim (Krist, 1993), was developed for generating model PSFs and may be obtained from STEIS.

Any of the extracted PSF images in the library may be retrieved directly from DMF in the same manner as other *HST* data (see archive manual in STEIS documents directory or email archive@stsci.edu); note that the archive class should be specified as CDB and extension as R7*. PSFs may also be requested from the STScI User Support Branch (USB) following the same procedures used for requesting calibration data.

1. Space Telescope Science Institute, Baltimore, MD 21218

This report presents a description of the growing contents of the STSci Library of observed WFPC PSFs; updated versions of the tables in this report will be maintained in the STEIS WFPC PSF Memo. The processing and extraction procedure used to obtain the PSF images for the library and the header format of the PSF images are described in §II. The filter and chip coverage of the Library images are presented in §II, followed by a summary of the data from which the PSFs are obtained. Finally, the Appendix contains tables of all PSF names along with filter used, position on chip, original observation name and date, exposure time, target name, and spectral type.

II. Library Images

Processing and Extraction

As an aid in the deconvolution of WFPC observations, a library of WFPC point spread function (PSF) images has been established in the STSCI Calibration Database (CDB). Rather than storing entire WFPC datasets which already reside in the *HST* archives, the library consists of smaller, typically 256x256, sub-sections centered on the PSF star if possible.

In preparation for PSF extraction, the original WFPC datasets were retrieved from DMF and reprocessed with the most up to date reference files (note that cosmic rays have not been removed and deltaflat corrections have not been applied). For images taken in a relatively non-standard way (for example, obtaining PSFs on multiple chips without reading out each time), it was also necessary to properly set the science data file's preflash-related keywords (PREFCORR, PREFFILE, PREFDFIL, SHUTTER) before re-calibrating, since the initial pipeline processing is unaware of the multiple exposures and erroneously sets PREFCORR to NO. The shutter in place during the preflash was derived using the IRAF task 'ENGEXTR' on the associated extracted engineering files (.X0H/.X0D); the values of the W06X135B and W06X136B mnemonics (SHUTOPNB and SHUTOPNA, respectively) indicate the shutter in place at the end of the exposure.

Header Keywords

The headers of the extracted PSF images contain information listed in the tables in the Appendix (and in the STEIS memo) as well as keywords for the camera, mode, origin, exposure time, modified Julian date, calibration flag and flatfield filename if the image was calibrated, PSFSCALE (divisor used to normalize the image), observation mode for use with SYNPHOT, a reference spectrum, and the secondary mirror actuator positions. The actuator position keywords were populated using the results presented in the OTA Instrument Science Report #7 (Burrows, 1992).

Table 1: PSF Image Header

keyword	sample value	description
GROUPS	T	group image?
GCOUNT	1	number of groups
PCOUNT	12	number of group keywords
PSIZE	512	number of bits allowed for all the group parameters
DATAMIN	-8.25279	minimum of all pixels
DATAMAX	1574.536	maximum of all pixels
CRVAL1	122.7054583333	right ascension of reference pixel (deg)
CRPIX1	111.	x-coordinate of reference pixel
CD1_1	1.125227E-5	partial of RA with respect to x
CTYPE1	'RA--TAN'	
CD1_2	4.800087E-6	partial of RA with respect to y
CRVAL2	74.96597222222	declination of reference pixel (deg)
CRPIX2	164.	y coordinate of reference pixel
CD2_2	-1.125227E-5	partial of declination with respect to y
CTYPE2	'DEC--TAN'	
CD2_1	4.800085E-6	partial of declination with respect to x
FILTNAM1	F785LP	first ST ScI filter name
FILTNAM2	"	second ST ScI filter name
CAMERA	PC	WF or PC
MODE	FULL	full or area
DETECTOR	6	1-4 for WF, 5-8 for PC
ROOTNAME	W15E100T	rootname of observation containing psf image
DATA_FIL	D9F15215W.R7H	name of psf image file
TARGNAME	BD+75D325	target
ORIGIN	HST	date source e.g., 'HST', 'TIM', or other
SPECTRAL	O5p	spectral type of source, if known
EXPTIME	0.8	exposure time in seconds
DATE_OBS	13/08/93	UT date (E.G. 28 Jan 1991)
MJD	49212.	modified Julian date (= JD-2400000.5)
XCORNER	362	x pixel of (1,1) corner in psf image
YCORNER	249	y pixel (1,1) corner in psf image
XCENTER	490.	x coordinate of psf center on chip
YCENTER	377.	y coordinate of psf center on chip
CALIBRAT	T	has this image been calibrated? (flat, etc)
FLATFILE	lclSc1916444w.r6h	name of flatfield used
PSFSCALE	1.	divisor used to normalize psf, otherwise 1
OBSMODE	PC,6,F,DN,F785LP	obsmode for synphot (e.g., WF,4,F,DN,F555W)
REFSPEC	"	ref spectrum (CRCALSPEC:AGK_81D266_002.TAB)
ACTUAT25	-1468	position of secondary mirror actuator 25
ACTUAT26	1306	position of secondary mirror actuator 26
ACTUAT27	-833	position of secondary mirror actuator 27
ACTUAT28	1023	position of secondary mirror actuator 28
ACTUAT29	-857	position of secondary mirror actuator 29
ACTUAT30	851	position of secondary mirror actuator 30

General Characteristics

Specific PSF image names are listed in the Appendix; this section presents the filter and spatial coverage of the Library contents. Table 3 summarizes the number and type of PSF images available from the PSF Library, sorted by filter and detector.

Table 2: Statistics on PSF Image Filters

filter	PC 5	PC 6	PC 7	PC 8	WF 1	WF 2	WF 3	WF 4
F230W	1	22	1	1		25		
F284W	1	30	1	1	1	33	1	1
F336W	3	41	4	1	2	34	1	1
F439W	1	35	1	1	1	33	1	1
F487N		17						
F502N		5						
F547M	1	5						
F555W	64	118	68	36	1	58	1	1
F588N		5						
F673N		5						
F702W	3	8	1	3	1	2	1	1
F718M	1	5						
F785LP	64	111	70	38	1	58	1	1
F889N	2	24	2		1	6	1	1

NOTE: there is one PSF, in P6 only, for each of the following filters: F368M, F375M, F437N, F413M, F469N, F492M, F517N, F569W, F656N, F658N, F606W, F622W, F631N, F664N, F648M, F675W, F725LP, F791W, F814W, F850LP, F875M, F1042M, F1083N.

The plots below illustrate the spatial coverage achieved for PC 5-8 and WF 2.

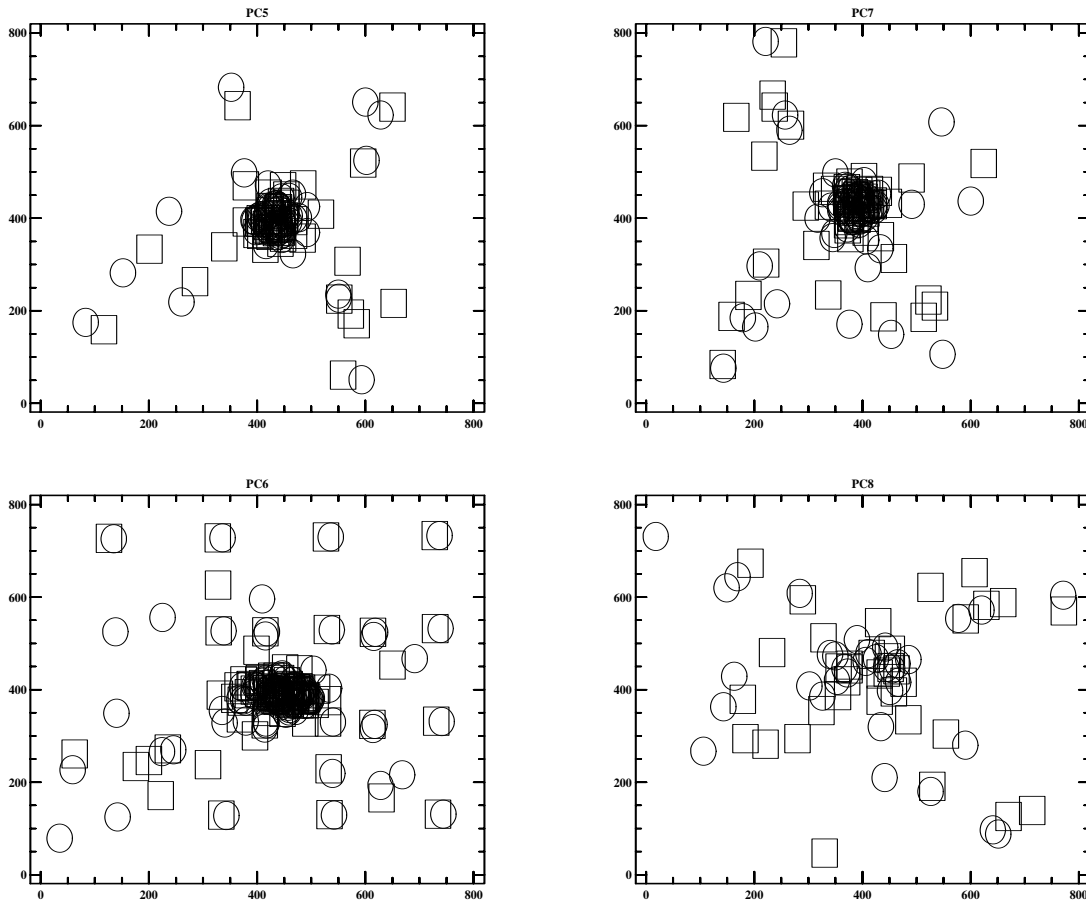


Figure 1: PSF coverage on PC chips. F555W PSFs are indicated with circles, F785LP PSFs with boxes.

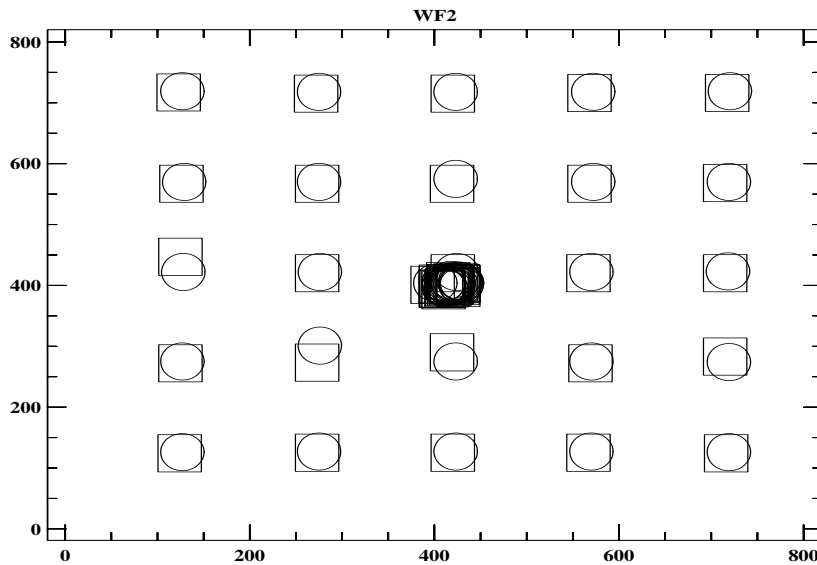


Figure 2: PSF Coverage on WF2 Chip. F555W PSFs are indicated with circles, F785LP PSFs with boxes.

Sources of PSFs

Data from a variety of proposals are used as sources for the PSF images; they are summarized in the table below.

Table 3: Proposals from which PSF Data Has Been Obtained

prop	proposal title	description of observations
3230	PC PSF and Focus Monitoring	PC 5 - 8 F555W and F785LP variety of targets/spectral types one-two stars imaged ~once/week
3241	Mapping Position Dependence of WFPC PSF	WF 2 with F555W, F785LP PC 6 with F336W, F413M, F439W, F487N, F502N, F547M, F555W, F588N, F673N, F718M, F785LP, and F889N two targets: HD151406(F0) and HD144470(B1)
4809	PSF Calibration Proposal	WF 1-4 and PC 5-8 F336W, F555W, F702W, F785LP, and F889N variety of targets/spectral types (chosen from proposals 3230 and 3241)
5025 4207 2877	Photometric Calibration Monitor	WF 2 and PC 6, executed ~once per month F230W, F284W, F336W, F439W, F555W, and F785LP target is UV standard (usually BD+75D325; when unavailable, alternates BD+28D4211 or A+81D266 are used)
4785 5269	Interchip Photometric Calibration	WF 1-4 in F336W, F284W, F439W, F555W, F702W, F785LP, F1042M PC 6 in most WFPC filters (33) PC 5,7,8 in subset (11) of the PC 6 filters executed Fall 1993 target: UV standard BD+75D325
4739	Single Chip UV Calibration	executed once after Aug 1993 decontamination WF2, PC6 : F194W, F230W, F284W target: UV standard BD+75D325
2875	QE Calibration	executed once after Feb 1992 decontamination WF2, PC6 F336W, F439W, F555W, F791W, F702W, F785LP, F889N, F1042M target: UV standard BD+75D325

Notes to table:

3230 - All of the Prop 3230 data has been ingested into the library. This includes the initial delivery as made to STSCI by the WFPC Instrument Definition Team (~100), as well as all observations obtained since then (~340). One or two stars were imaged roughly once per week in PC 5-8, usually 0.11 second exposures taken with F555W and 0.23 second exposures taken with F785LP. Note that 0.11 second exposures may be of limited usefulness due to obscuration of the light beam by the shutter blade (for additional details and discussion of these PSF observations, see the Final OV/SV Report (WFPC IDT, 1992)).

3241 - All of the PSF images from the OTA Calibration Proposal (#3241) 'Mapping the Position Dependence of the WFPC PSF' have been ingested into the Library. The PC 6 observations were taken through a variety of filters (F336W, F413M, F439W, F487N, F502N, F547M, F555W, F588N, F673N, F718M, F785LP, and F889N). Spatial coverage was obtained by imaging the star in 4x4 grids across the chip (F487N and F889N) and in 2x2 grids on the chip for the other filters. The WF 2 observations, taken in F555W and F785LP, imaged the target star in 5x5 grids across the chip.

4809 - All PSF images from the 'PSF Calibration Proposal' obtained so far have been extracted and archived into the library. Images from this proposal are being taken on all four chips, for a subset of filters (F336W, F555W, F702W, F785LP, and F889N). In addition, some spatial coverage is obtained via 2x2 grids of PSF images, taken in these same five filters, in P6 and W2 (see also ISR 92-13, PSF Calibration Plan, S.Baggett and J.MacKenty; note however, that not all observations planned may be taken by the time of the servicing mission).

5025/4207/2877 - Current PSF library installations will include data from the WFPC Cycle 1, Cycle 2, Cycle 3 'Photometric Calibration Monitor' proposals (#2877, #4207, #5025 respectively). These programs obtain WF 2 and PC 6 observations of a UV flux standard about once a month, in F230W, F284W, F336W, F439W, F555W, and F785LP; the PSF memo on STEIS will continue to be updated as necessary to reflect the growing contents of the PSF library.

4785/5269 - The 'WFPC Cycle 2 Interchip Photometric Calibration Proposal' will be taking exposures of usual UV standard BD+75D325 in a variety of popular filters (F284W, F336W, F439W, F555W, F702W, F785LP, and F1042M) for all WF and PC chips as well as exposures in PC6 in most other filters. Many of the images are already in the library; as the final observations are obtained, they will be processed and extracted in the same manner and archived into the library.

4739/2875 - Data from the Single Chip UV Calibration and QE Calibration proposals, which were executed once after the 1993 and 1992 decontamination procedures respectively, will be added to the Library in the near future.

We thank C. Ritchie for providing calibrated images of the Proposal 4785/5269 data.

References

- Baggett, S. M., and MacKenty, J. W., WFPC PSF Image Library Memo, copies available on STEIS.
- Burrows, Christopher, OTA Instrument Science Report #7, "HST Focus and Collimation", Feb 20, 1992.
- Burrows, Christopher, and Hasan, Hashima, Tim Users Manual (Version 30, November 11, 1993).
- Burrows, Christopher J., Holtzman, Jon A., Faber, S.M., Bely, Pierre Y., Hasan, Hashima, Lynds, C.R., and Schroeder, Daniel, ApJ 369, L21, 1991.
- Krist, John, The Tiny Tim User's Manual (Version 2.4, August 1993).
- WFPC IDT, Final Orbital/Science Verification Report, Faber et al., Feb. 1992.

Appendix - Image Names

The tables in this Appendix, one for each detector, summarize the contents of the library at the time of writing; the PSF memo on STEIS will continue to be updated with new deliveries. The information provided in the tables consists of

d : detector (WF=1-4, PC=5-8)

filter : filter name

data_file : rootname of the extracted PSF image (extension .r7h and .r7d)

date_obs : date of the observation (dd/mm/yy)

rootname : name of the original dataset from which PSF was extracted

targname : name of the observed star if known

exp : exposure time (sec)

sp : spectral type of the star (U for unknown)

xc : x pixel of PSF peak in original chip coordinates

yc : y pixel of PSF peak in original chip coordinates

peak : maximum counts in peak of PSF (DN)

All of these keywords except 'peak' are also contained in the individual PSF image headers.

WFPC Flat Field Calibration: Flats and Delta Flats

John A. Biretta¹, Sylvia M. Baggett¹, John W. MacKenty¹
Christine E. Ritchie¹ and William B. Sparks¹

Abstract

We review WFPC flat field calibration, as well as the removal of time-dependent effects with Delta flats. Emphasis is placed on various flat fielding problems and their solutions.

I. Introduction

The purpose of flat field calibration is to bring all detector pixels to the same photometric response. The method usually employed is to divide the observed images by exposures of a uniformly illuminated source. While observers will be familiar with this process, there are some differences between flat fielding of ground-based data and WFPC data which should be kept in mind. First, unlike ground-based imaging where one is attempting to flatten a large sky pedestal, most WFPC observations have little or no sky pedestal. Hence, the illumination pattern of the data frames will generally be quite different from those of the flat field calibration images. A related effect is that WFPC images often seem less “flat” after flat fielding, since the uniform readout noise becomes modulated by variations in the calibration flats, even though the flat field calibration is working properly. Another difference is that diffraction effects are much more important for flat fielding WFPC data, as compared to ground-based data. For example, features not in the focal plane (e.g. particles on CCD windows), will not flatten as well as features on the CCDs themselves. Furthermore, differences in color (spectrum) and illumination between the observation target and the flat field light source will be more important.

II. Features and Structures in WFPC Flat Fields

There are many features which appear in WFPC calibration flats. Here we briefly describe some of these, roughly in order of occurrence along the optical path. We will use the WFC F555W calibration flat as an example, since it is one of the more popular filters. Figure 1a shows the entire field of the four WFC CCDs, while Figures 1b and 1c show the center of CCD WF2 at various enlargements. This illustration shows an *observed* flat; the data would be effectively *divided* by this image during calibration. (The actual calibration flats used in the pipeline and CALWFP are inverted, and are multiplied into the data.)

1. Space Telescope Science Institute, Baltimore, MD 21218

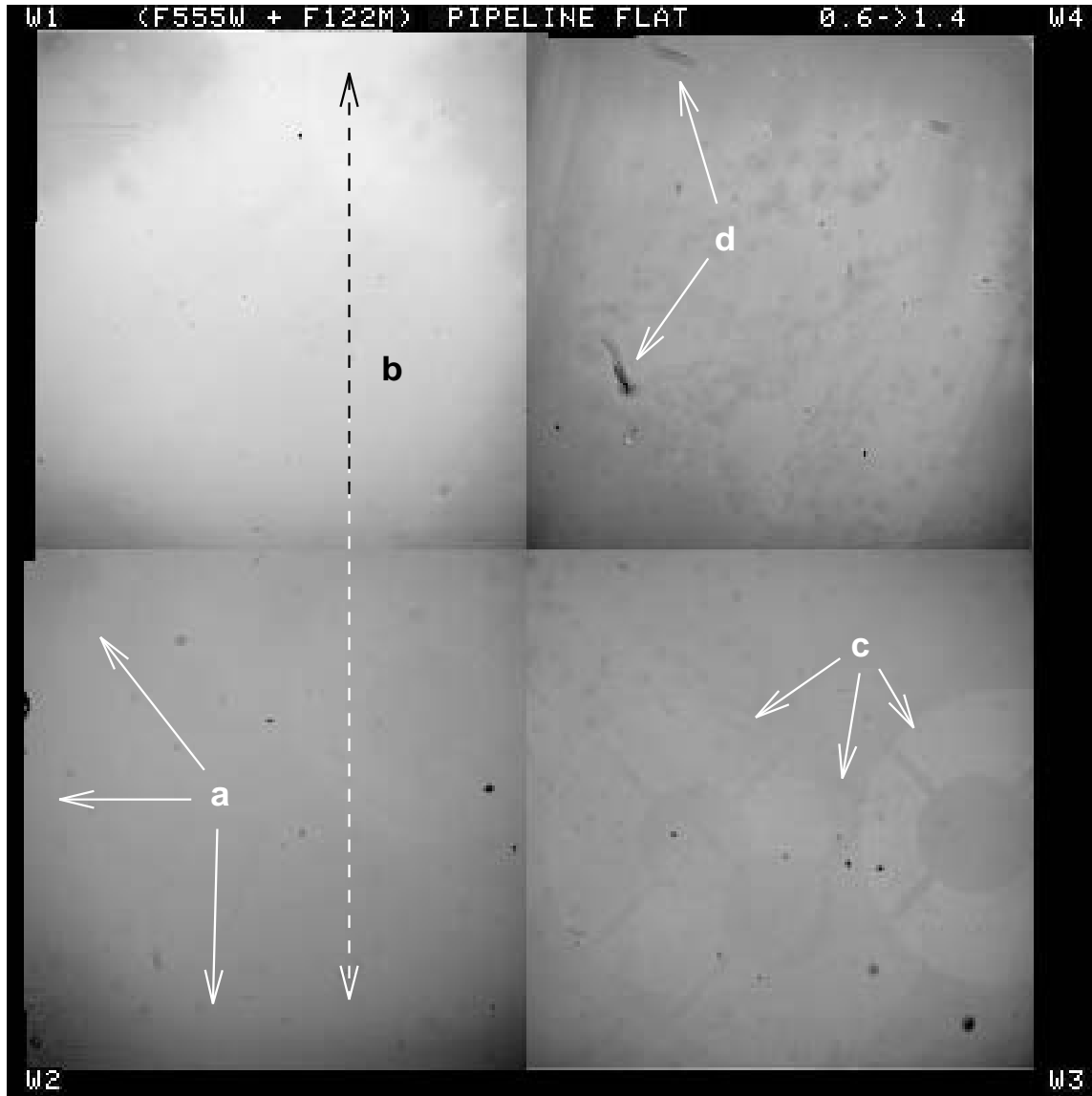


Figure 1a: Flat field used in the calibration pipeline for filter F555W in the WFC mode. The four CCDs have been mosaicked together as they would appear on the sky, and are labeled in their corners. As with many broad-band flats, this one has been observed using the F122M filter to provide neutral density. Labeled features include (a) an intensity fall off at the CCD edges due to vignetting in the camera relay optics, (b) ~30 percent intensity gradient running from the bottom (dark) to top (bright) of the image, which is caused by the neutral density filter, (c) bright “donuts” caused by pinholes in the neutral density filter, and (d) large dust particles on the CCD windows. Display range is from 0.6 (black) to 1.4 (white).

Vignetting in the WFPC relay optics cause the CCD edges to see only a portion of the telescope primary mirror. This causes an illumination drop-off of about 15 percent between the CCD centers and edges, as seen in Figure 1a.

A similar but much smaller effect involves an interaction of the OTA and WFPC obscurations. Near the CCD centers, the OTA spider and WFPC relay secondary support posts have coincident shadows, but at the field edges all seven obscurations appear separately. The amplitude of this effect is only a few percent, and is difficult to discern in the flats.

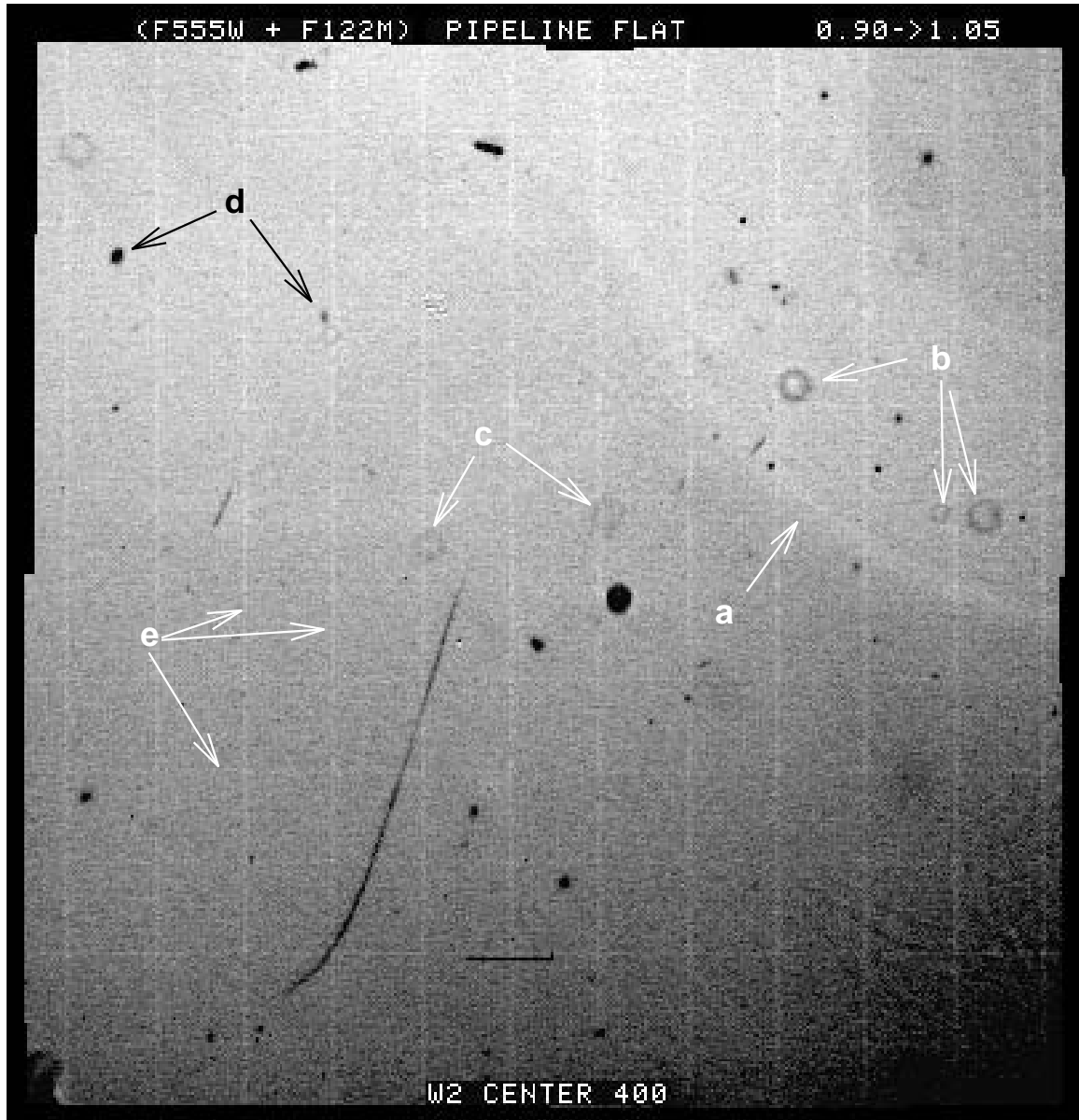


Figure 1b: Enlargement of central 400×400 pixels of WF2 for the image shown in Figure 1a. Labeled features are (a) circular arc caused by pinhole in neutral density filter, (b) small dust spots and (c) measles features on the CCD windows, (d) small dust particles on the CCD, and (e) 33 column / row manufacturing defect in the CCD itself. The display range is from 0.90 (black) to 1.05 (white).

Irregularities in the WFPC filters also contribute features. Perhaps the most important features are those contributed by the F122M filter. The red-leak in this filter is commonly used as a neutral density filter when observing many of the broadband calibration flats (see discussion below). In the case of the F555W calibration flat, the F122M filter contributes a 20 to 30 percent intensity gradient across the four WF CCDs. This is visible as an overall increase in the illumination between the bottom and top of Figure 1a. Small pinholes in the F122M filter also contribute large donut-shaped features which are several percent high. These donuts are images of the WFPC Cassegrain relay pupils.

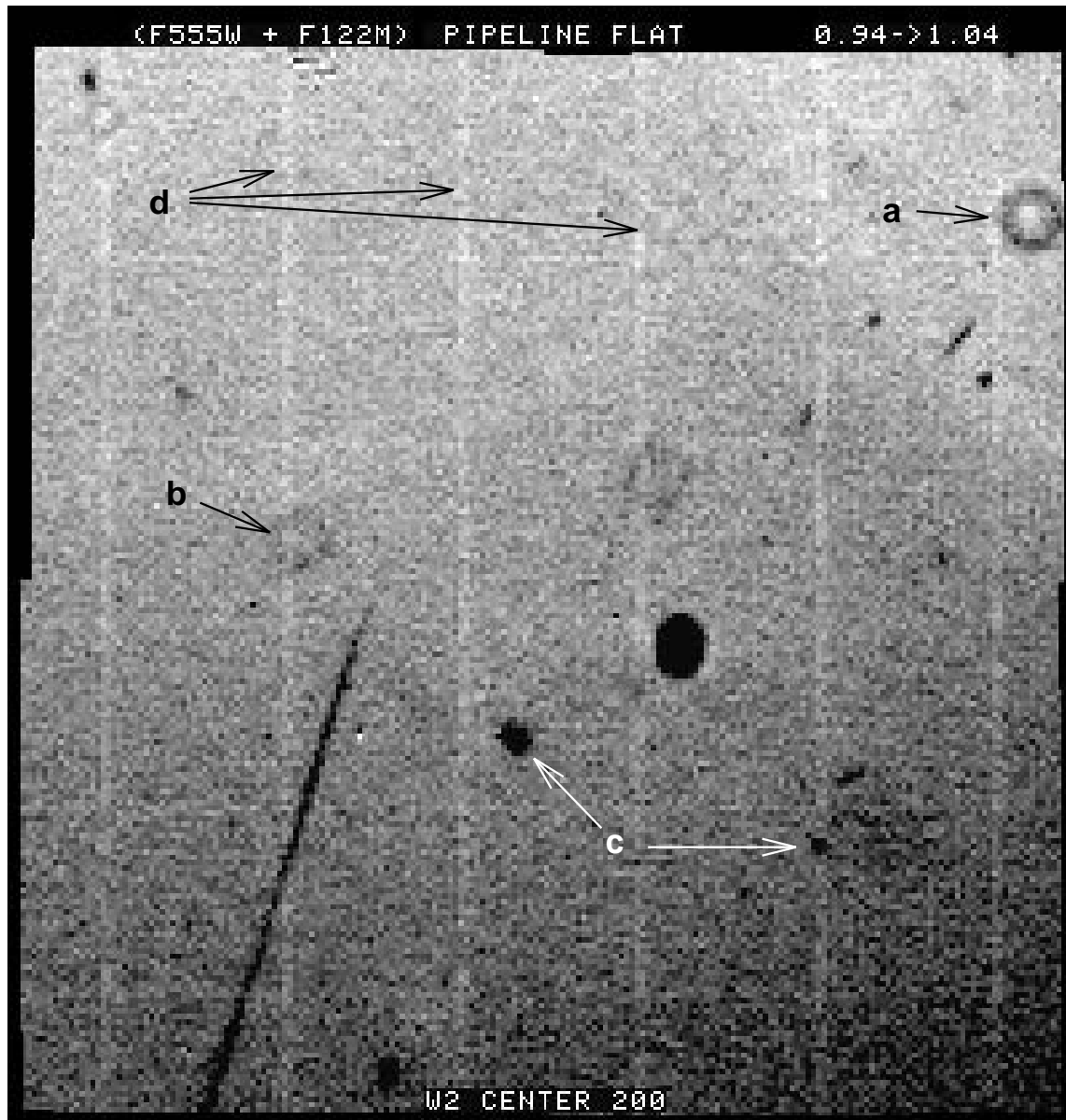


Figure 1c: Enlargement of central 200×200 pixels of WF2 for the image shown in Figure 1a. Labeled features are (a) small dust spots and (b) measle features on the CCD windows, (c) small dust particles on the CCD, and (d) 33 column / row manufacturing defect in the CCD itself. The display range is from 0.94 (black) to 1.04 (white).

Contamination on the CCD windows comes in many forms, and can generally be distinguished from other features as they are slightly out-of-focus. Fibers and dust particles tend to cause large features (e.g. as seen on WF4 in Figure 1a). Low volatility contaminants which remain on the CCD windows after decontaminations cause “persistent measles” (Figures 1c and 2). These appear as bright or dark spots several pixels in diameter, surrounded by concentric bright and dark rings totaling ~ 10 pixels in diameter. The amplitude of these features is typically 1 or 2 percent about the local level, but can reach ± 5 percent. While their exact composition is unknown, they are consistent with particles 10 to 15 microns in diameter.

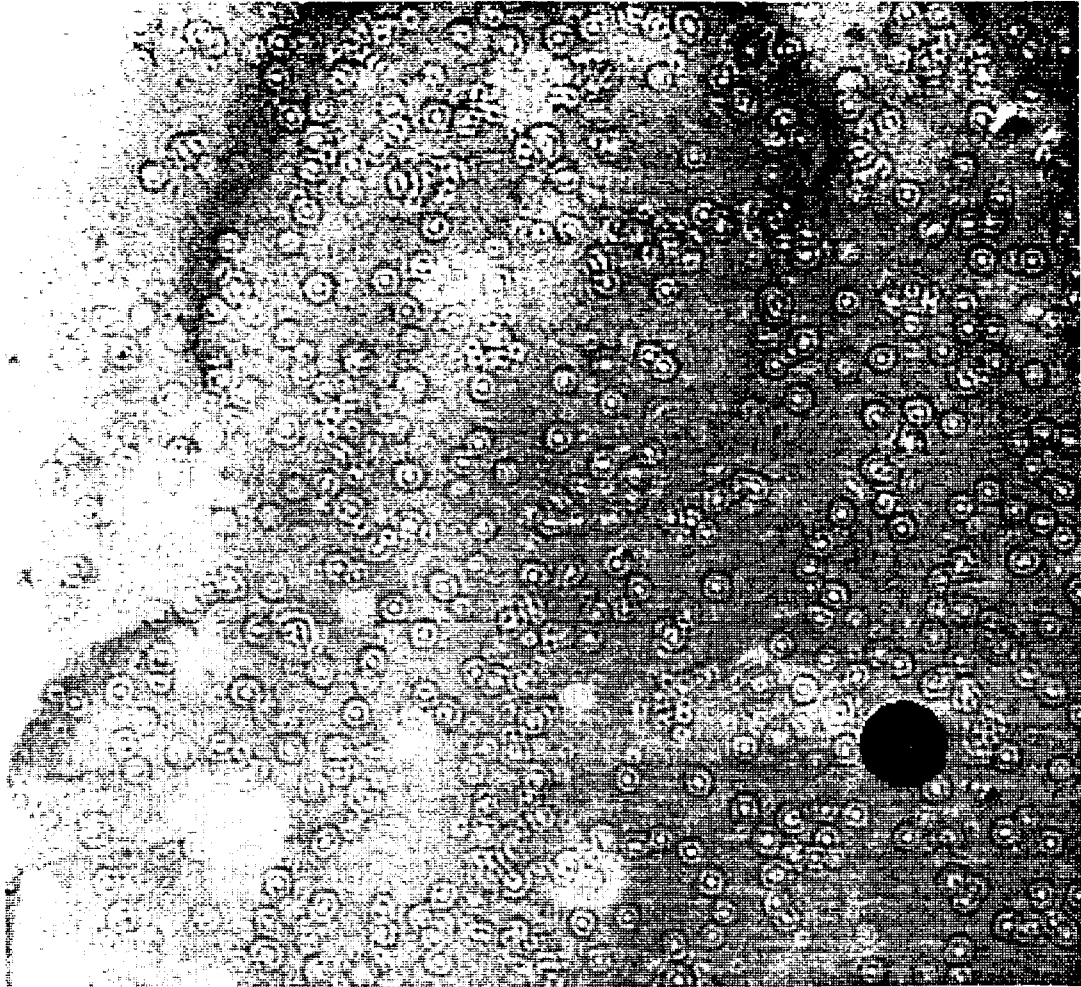


Figure 2: Illustration of an extreme case of measles. This is an Earth calibration flat for PC8 in the F517N filter. The display range is about ± 7 percent about the mean. From MacKenty, et al. 1992.

High volatility material slowly collects on the windows in a quasi-uniform layer between decontaminations. This material scatters light at short wavelengths, which has the effect of reducing the total illumination (direct + scattered light) at the CCD edges, so that the CCD edges droop in the flat fields. This quasi-uniform layer also alters the properties of the measles and reduces the throughput at UV and blue wavelengths.

Fibers and dust particles on the CCDs themselves tend to be in sharp focus and have a large intensity amplitude (Figures 1b and 1c). Some of these features may also arise on the pyramid mirror, which lies near the OTA focal plane.

The CCDs themselves have sensitivity variations which are apparent in the flat fields. Every 33 pixel columns, there is a pair of columns whose sensitivity is a few percent higher than average (Figures 1b and 1c). A similar pattern occurs every 33 rows. These features result from errors in the CCD manufacturing process. Other features include spots and large regions with anomalous sensitivity due to partial loss of the UV flood, variations in chip thickness, and variations in the Coronene coating.

III. Flat Field Calibration Images

The flat fields currently in use are short exposures of the bright sun-lit Earth. Due to the combination of Earth features and spacecraft motion, these raw Earth-cals often contain patterns of bright and dark streaks which must be removed from the images. This is done using an STSDAS program called STREAKFLAT, which uses many Earth-cals taken at different streak angles to disentangle the flat field pattern from the streaks. Once a suitable destreaked flat is obtained, it is normalized to a mean level of unity, bad areas are clipped out, and the image is inverted using NORMCLIP (also in STSDAS). The resulting calibration flat is then *multiplied* into the data during normal pipeline calibration.

The current library of Earth calibration flats in the Calibration Data Base System (CDBS) were all observed during the baseline epoch between August 1991 and January 1992 (Figure 3). There are two groups of flats, distinguished solely by their origin. The Science Verification or SV flat group contains 36 flats for popular filters, and were supplied by the WFPC Investigation Definition Team (IDT). The second group contains 40 flats for most remaining filters, and were generated by STScI. Besides these Earth-cal flats, there are a variety of other flats available from pre-launch tests, etc. A detailed list of the available flats is maintained on STEIS, and also appears in various WFPC Instrument Science Reports (see references).

While the Earth flats provide the most efficient flat field calibration, they do suffer a number of problems which compromise the final calibration. The most serious problem is that the Earth is too bright, so that either neutral density (ND) filters must be used, or very short exposures (<1 sec) are necessary. The former is problematic, since the ND filters contribute their own pattern and can cause reflections, while short exposures result in very strong streaks which are more difficult to remove from the images. Furthermore, the Earth's albedo is highly variable and unpredictable, so that most of the raw Earth flats are either underexposed or saturated. This low yield makes it very difficult to get enough flats for reliable streak removal. Finally, the Earth color is poorly known and probably does not match that of the celestial targets one wishes to calibrate. Blue oceans, green trees, and red houses are all possible Earth-cal targets.

IV. Internal Flats and Delta Flats

Since the Earth flats only cover a small portion of the camera's history, it is useful to have some other means of checking for, and correcting, time-variability in the flat fields. For this purpose monitoring programs have been undertaken using the internal flat field capability of the WFPC.

Internal flats are exposures taken with faint lamps illuminating the back side of a closed shutter blade. There are two shutters, A and B, either one of which may be in the closed position. The reflectivities of the two are slightly different, so only data from the same shutter should be compared when looking for changes in the flat fields. These internal flats are taken every few weeks in nearly twenty popular filters for each camera. In general, these internal flats are useful only for tracking changes, since their illumination pattern is quite different from that of the OTA, making them unsuitable for use as calibration flats.

WF/PC FLAT FIELD CALIBRATION HISTORY

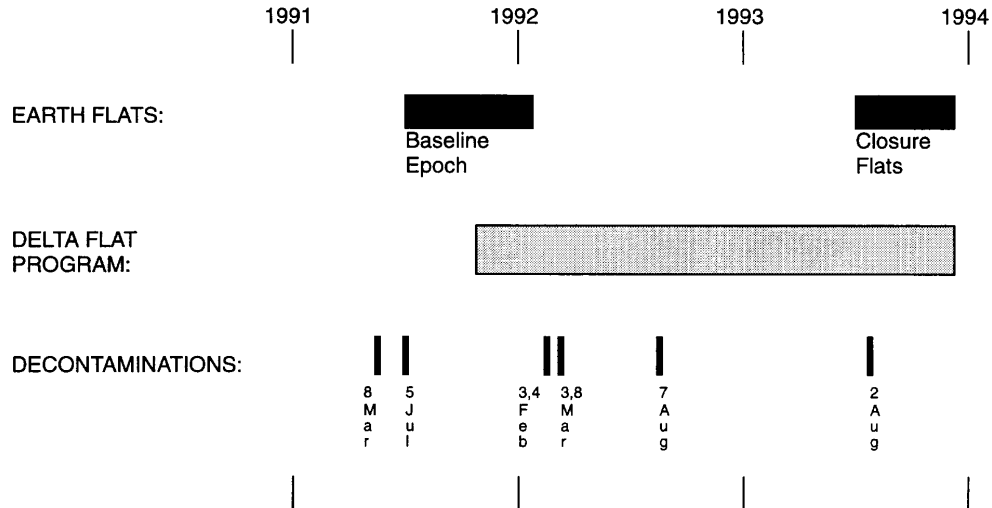


Figure 3: Timeline illustrating the history of the WFPC flat field calibration. The existing Earth calibration flats were observed during the baseline epoch in late 1991 and January 1992. New Earth flats are currently being observed and will be delivered early in 1994 (closure flats). The Deltaflat program spans the interval between the baseline and closure flats. Decontamination events are marked along the bottom of the Figure.

When searching for time variations in the flat fields, it is very helpful to compute ratios of these internal flats. Delta flats are defined to be ratios of single internal flats taken at different epochs (MacKenty and Baggett 1992). Since we are primarily interested in changes since the epoch of the Earth flats, an internal flat from the epoch of the Earth flats, or baseline epoch, is used in the numerator. Hence, Delta flats are computed as:

$$\text{Deltaflat} = (\text{Baseline epoch internal flat}) / (\text{new internal flat})$$

where baseline epoch refers to the period August 1991 to January 1992 (Figure 3). Strictly defined, these are ratios of *single* short exposures, so they tend to contain small numbers of cosmic rays. Average Delta flats are defined to be ratios of *averaged* internal flats. Since the measles tend to be constant between decontaminations, the usual procedure is to average all the internal flats between decontaminations for a given filter. This averaging reduces both the cosmic rays and noise in the images. Some effects, like the CCD edge droop at short wavelengths, do vary between decontaminations, so in some cases it may be better to use the Delta flats rather than the Average Delta flats.

Both types of Delta flats may be used to either check for flatfield variations, or to correct calibrated images. A Deltaflat close in time and wavelength to the science

observation should be used. In the case of a single small target, it may be easiest to merely examine the Deltaflat to insure there are no appreciable changes at the target position on the CCD. In other cases it may be desirable to actually correct the data by multiplying the Deltaflat into the calibrated data. That is:

$$\text{Corrected data} = (\text{Calibrated and flattened data}) \times \text{Deltaflat}.$$

These Deltaflat corrections will often be imperfect, however, since many of the time-variable features arise on out-of-focus surfaces in the cameras. For example, the persistent measles which remained after the February 1992 decontamination result from contaminants on the CCD windows (Figure 2). Because these contaminants are not in the focal plane, the measles pattern will depend on both the illumination and color of the target (diffraction effects, etc.). Unless the target is uniformly illuminated (i.e. planets) one can expect only a partial correction. A general rule of thumb is that the Delta flats will reduce flat fielding errors due to measles by a factor of about two.

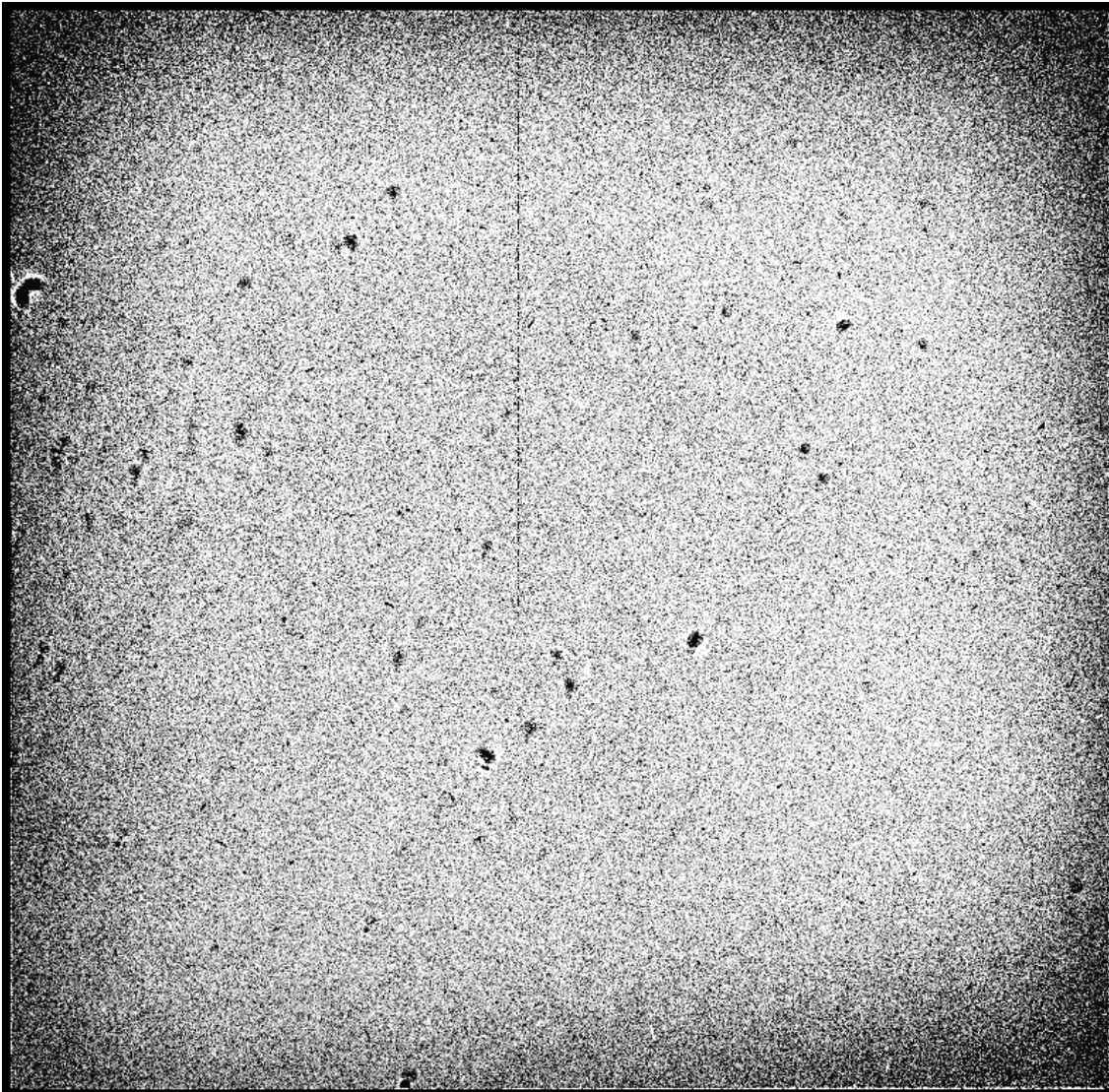


Figure 4: A ratio of PC6 internal flat fields showing the edge droop effect at 439 nm wavelength. Display range ± 2.5 percent about the mean.

Another effect appearing in Delta flats, as well as Earth flats, is the flat field edge droop mentioned in Section 2. The quasi-uniform contaminant layer on the CCD windows scatters light. Near the CCD centers, this scattered light is detected in nearby pixels, so there is little apparent effect on the illumination. But at the CCD edges, the predominant effect is for light to be scattered out of the field of view, causing the edges to be dim or droop (Figure 4). This effect increases gradually between decontaminations as material builds up on the windows, and then largely disappears immediately after decontaminations. The effect is also strongly dependent on wavelength, and is greatest in the blue and UV. For science images the effect will depend on the target illumination pattern. For small stellar targets, there is little droop effect, since the scattered light is lost into the noise of nearby pixels; but for uniformly illuminated targets the effect will be quite similar to that in the flats.

A library of both Delta flats and Average Delta flats is maintained in the CDBS. See STEIS memos for listings of available files (Baggett and MacKenty 1993a).

V. Problems Limiting Flat Field Accuracy — and Solutions

Neutral density filter patterns.

The red leak in the F122M filter has been used as a neutral density filter when observing many of the broad-band Earth flats. Flats observed through the F122M include F555W, F606W, F675W, F702W, F725LP, F814W, and F850LP. It is important to note that intensity variations and patterns caused by the F122M filter *have not been removed from the Calibration Data Base flats!* Since the F122M is not used for science observations, of course, its pattern will corrupt science images during normal calibration.

A solution to this problem is to derive the F122M pattern by taking ratios of flats observed with and without F122M, and then using this derived pattern to correct calibrated science images. The narrow-band filter flats will work best for deriving the F122M pattern, since they have long exposures which minimize streaks and reciprocity effects. For example, we can derive the pattern using F502N flats in the Calibration Data Base System (CDBS), by computing the ratio $(F502N+F122M)/(F502N)$, with the result shown in Figure 5.

Here we see clear evidence for ~25 percent intensity gradient running across all four CCDs. This gradient was first reported by Hester (1992). There are also a number of bright donuts which are caused by pinholes in the F122M filter. These are images of the camera relay pupils; shadows of the Cassegrain secondaries and their three support posts are visible inside each donut. The amplitude of the donuts is about 2 percent, though in some cases they overlap, producing a stronger effect.

This derived pattern can then be used to remove the F122M pattern from calibrated science images. To illustrate this process, we have used the F122M pattern in Figure 5 to correct an F588N flat taken with F122M, and then divided the result by a bare F588N flat. The resulting image, computed as $(F588N+F122M)/(F588N)$ (Fig. 5) is shown in Figure 6. If this process were perfect, we would expect the result to be

perfectly flat. From Figure 6 it is clear that it works quite well. The gradient across the four CCDs has been reduced from ~25 percent to about 4 percent peak-to-peak. The pinhole donuts have been reduced from 2 percent to about 0.5 percent. The fluctuations over the entire WFC field are now about 1.6 percent RMS. We can also begin to see streaks at the 1 to 2 percent level, which are presumably residual streaks from the Earth flats.

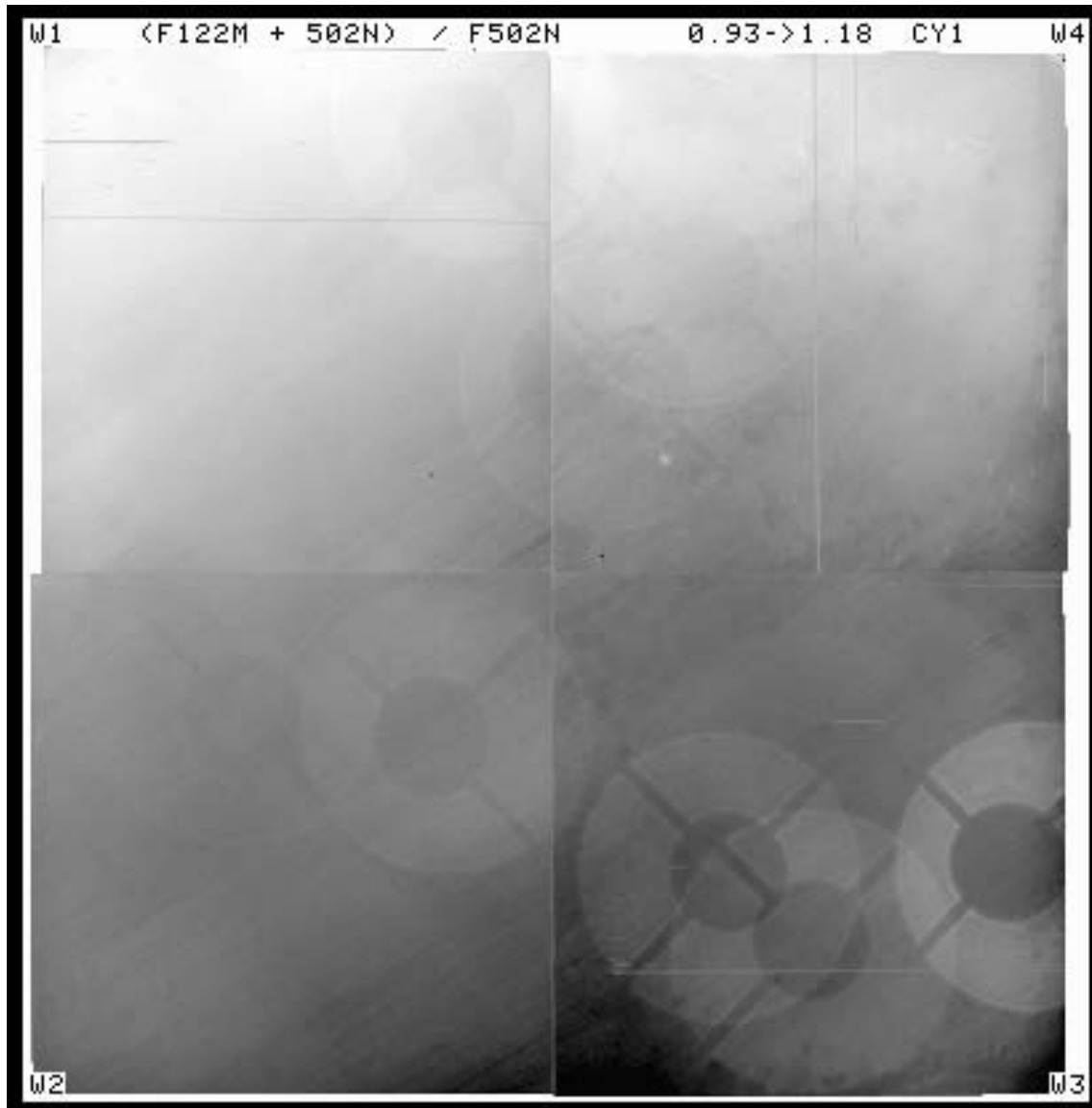


Figure 5: F122M filter pattern derived from existing F502N flats for the WFC. All four WFC CCDs are mosaicked together as they would appear on the sky; the individual CCDs are labeled in the corners. A 25 percent intensity gradient is clearly present, running from the image bottom (dark) to top (bright). There are also a half dozen or so donuts which are caused by pinholes in the F122M filter. The intensity scale ranges from 0.93 (black) to 1.18 (white).

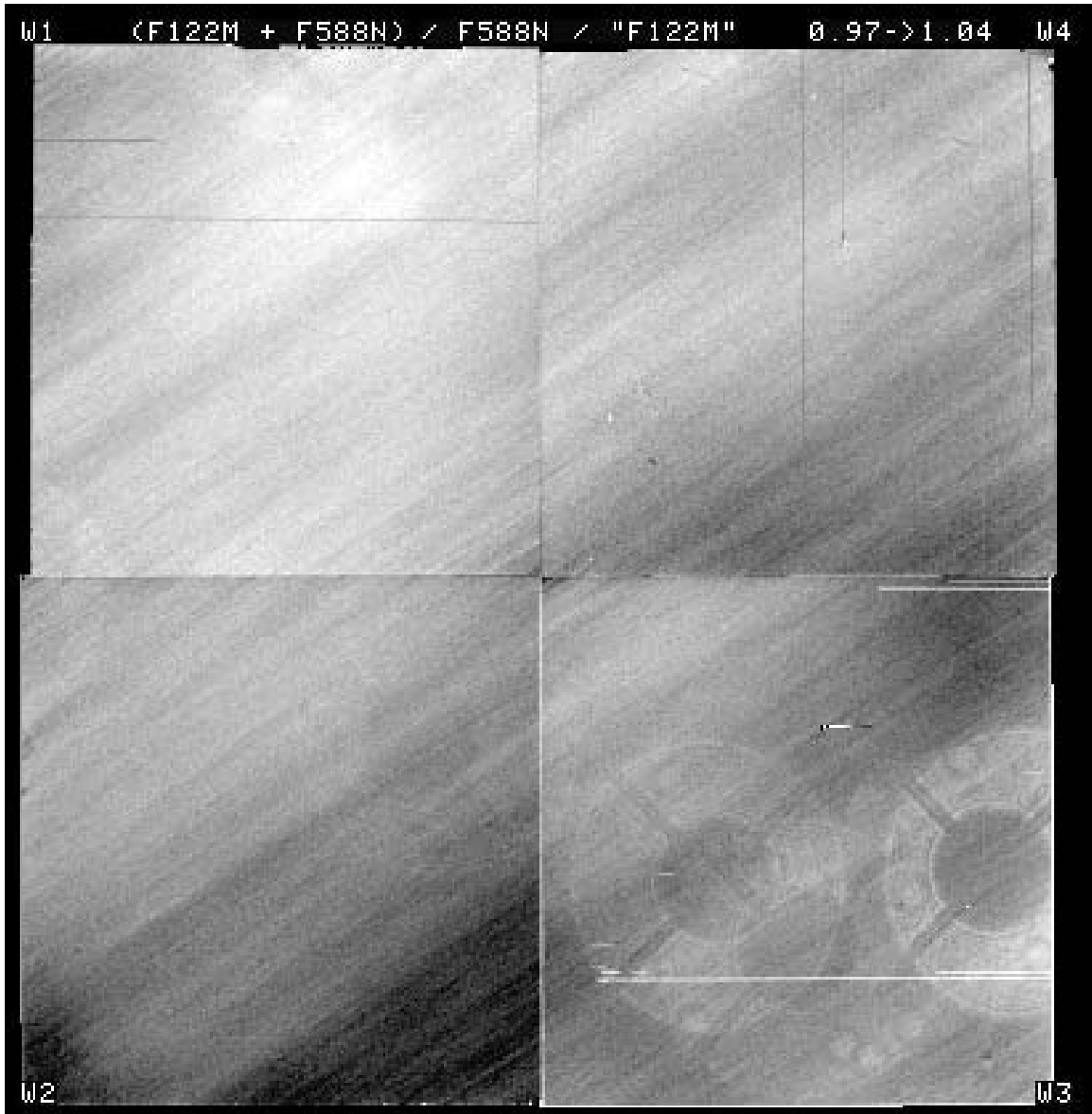


Figure 6: Example of using F122M pattern derived from F502N flat to correct a (F588N+F122M) flat. A 4 percent peak-to-peak gradient remains, as well as 0.5 percent donuts. Residual streaks from the Earth-cals are now evident at the 1 to 2 percent level. The intensity scale ranges from 0.97 (black) to 1.04 (white).

As we will soon see, this procedure does not always work so well. It worked very well for F502N and F588N, because the filters have similar wavelengths, similar constructions, and are in the same filter wheel (wheel 7) within the Selectable Optical Filter Assembly (SOFA).

Another success story is the application of Figure 5 to the F555W broad-band filter flat. We can correct the CDBS (F555W+F122M) flat using Figure 5, and then compare the result against the F555W super-sky flat generated by the Medium Deep Survey group (Ratnatunga, et al., this volume). Our corrected F555W flat and the sky flat are consistent to 2 percent RMS over the central 600×600 pixels of each CCD. (The CCD

edges show slightly larger errors, such that the difference over the entire WFC field is 3 percent RMS.) Again, this works well since F502N and F555W are close in wavelength, and are adjacent in the SOFA (wheels 7 and 9, respectively). Clearly, the materials already exist in the CDBS to largely eliminate the neutral density filter patterns for some filters.

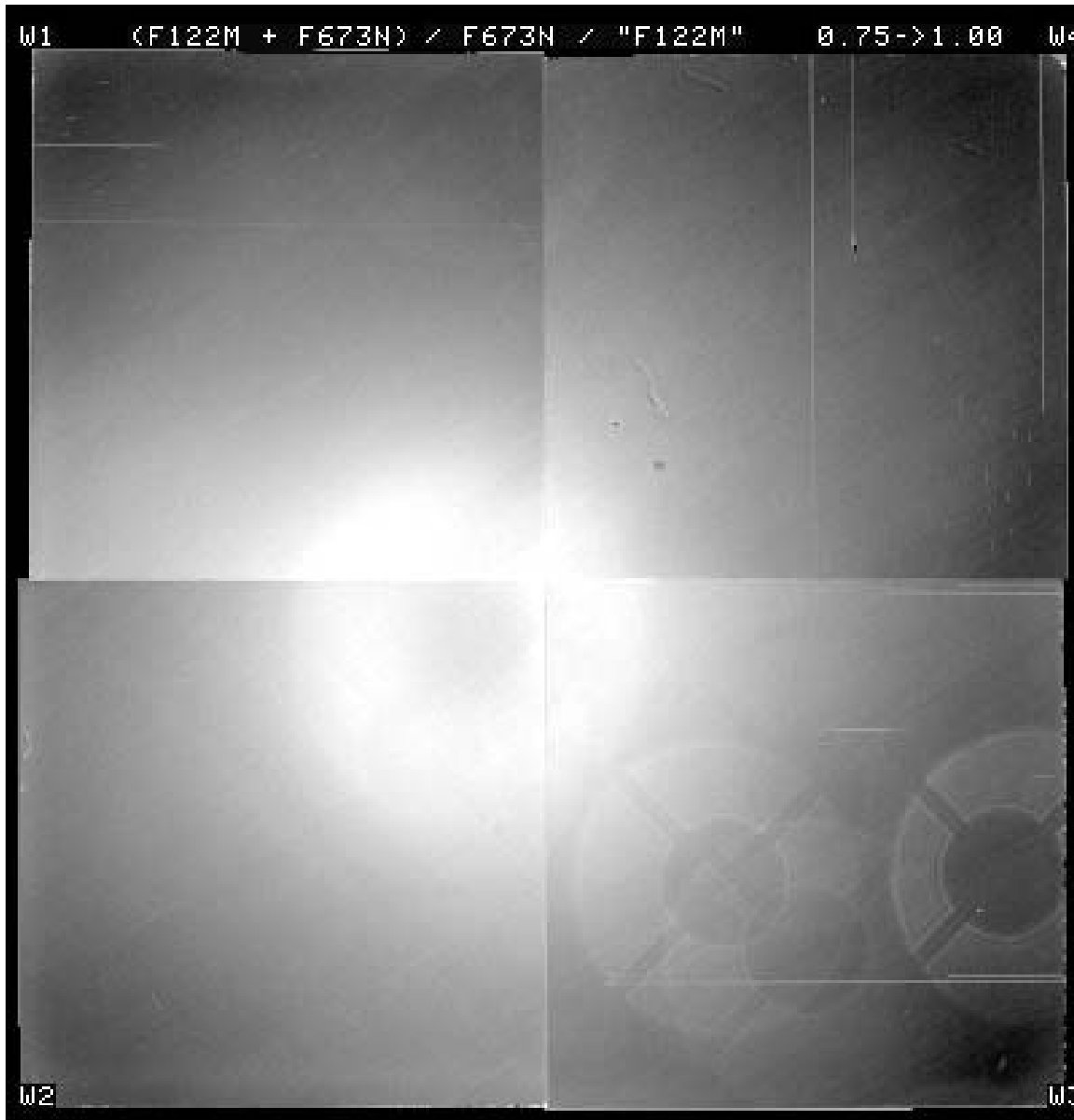


Figure 7: Example of using F122M pattern derived from F502N flat to correct (F673N+F122M) flat. Reflections cause a 30 percent bright spot near the pyramid apex, and hence the procedure fails for F673N. The intensity scale ranges from 0.75 (black) to 1.00 (white).

But things are never so simple as one would like. While we have been successful in deriving the pattern from F502N, and then correcting F588N and F555W with the derived pattern, there are cases where this procedure fails. For example, if we attempt to correct a (F673N+F122M) flat using Figure 5, we obtain the result shown in Figure 7. Obviously this has not worked very well; there is a 30 percent high spot in the center of the image. This high spot results from a reflection off the convex surface of F122M, which is quite strong because F673N is immediately above F122M inside the SOFA (wheels 1 and 2, respectively). This procedure also fails to correct (F889N+F122M). Reflections cause ~25 percent errors, and are due in part to very different wavelengths compared to F502N, different filter constructions (double vs. single interference filters), and different locations in the SOFA (wheel 12 vs. wheel 7). Fortunately, good flats exist for both the bare F673N and F889N filters, so that F122M pattern removal is merely an academic exercise. However, this does emphasize that caution is needed when using the above procedure.

In summary, the F122M filter pattern can be removed to a few percent accuracy using ratios of narrow-band flats. But successful application of this method requires that the filters have similar wavelengths, similar locations in the SOFA, and similar constructions.

Residual streaks in Earth flats.

The STREAKFLAT program is used to remove streaks, which are caused by Earth features, from the flat fields. This program requires about eight input Earth-cals with a wide range of streak angles to successfully remove the Earth features (i.e. reduce streaks below 1 percent level). Due to atmospheric haze the streaks tend to be strongest in the red, and weaker in the blue, so that more or fewer input files might be required at extreme wavelengths.

Long Earth exposures are best, since more averaging occurs along the direction of spacecraft motion. *HST* moves about 40 WFC fields per second, so that little averaging occurs at the shortest ~0.1 second exposures.

An example of a worst case scenario is the F785LP flat currently installed in the pipeline and CDBS. This is a far red filter and 0.1 second exposures were used, so that individual Earth-cals are expected to have very strong streaks. Furthermore, as the header for this flat shows, only four Earth-cals with similar streak angles were used with STREAKFLAT. Given all this, one can expect trouble. As Figure 8 shows, the resulting calibration flat has 15 percent residual streaks which will impose similar errors on the calibrated science data.

Observers can check for similar problems in other calibration flats by examining the headers for those files. The headers list the observed Earth-cals for each flat, and their streak angles.

Trouble is likely if there are only a few input files, or if they all have similar streak angles. Exposure times for the Earth-cals can be checked in either the O/SV Report (Hester 1992) or by querying STARCAT. Exposures much less than 1 second also suggest possible trouble. The ultimate solution is to take more Earth-cals and generate new calibration flats; this work is currently underway.

Jeff Hester's reciprocity effect.

CCD artifacts appear different in very short exposures (<1 second) and very long exposures (c.f. Hester 1992). For example, comparison of 0.1 and 0.3 second flats show 2 percent errors. Hence, short Earth-cal exposures (<1 second) will do a poor job of flattening long science exposures, and should generally be avoided. Again, observers can check the exposure times for the calibration flats as outlined above.

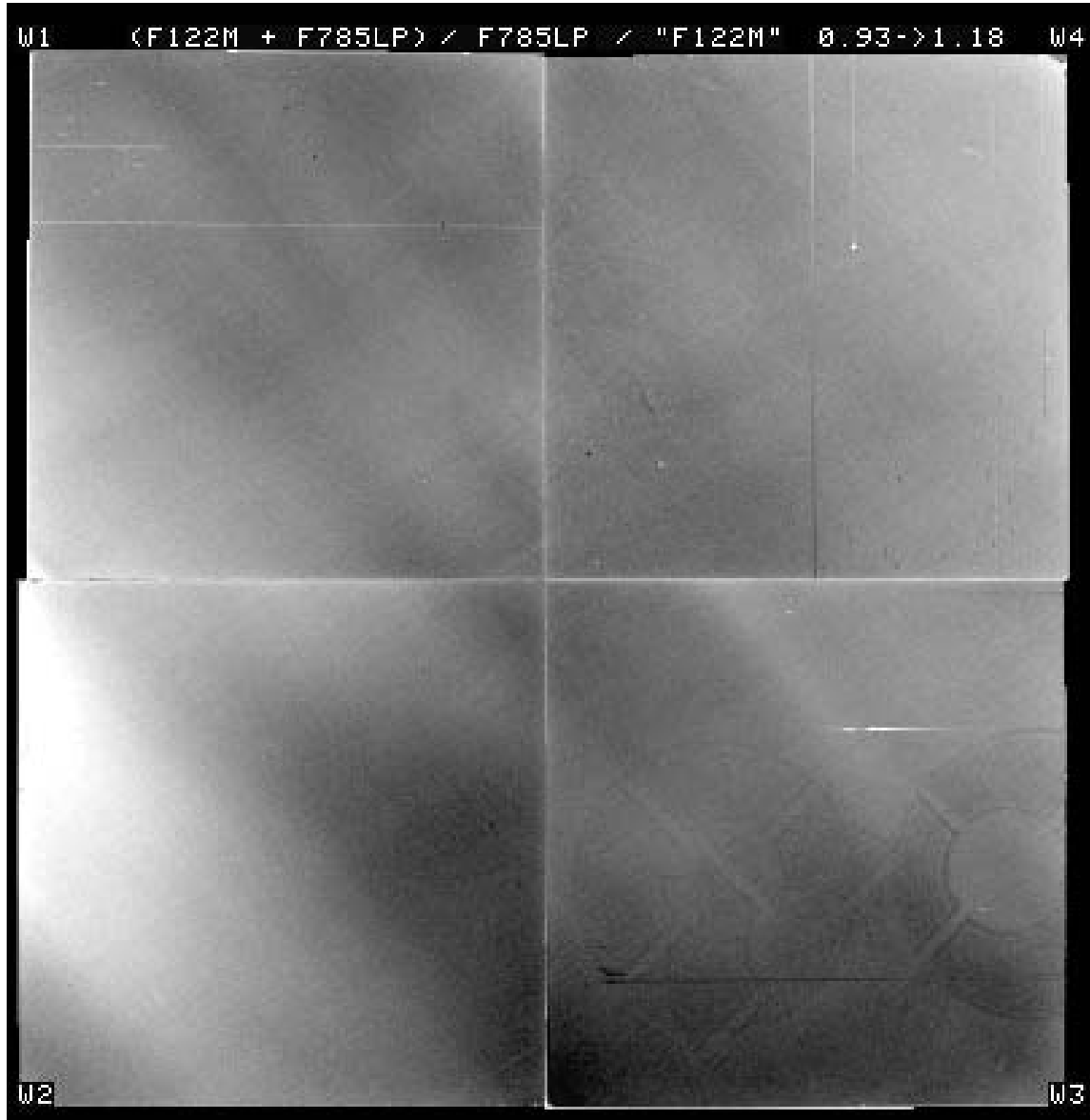


Figure 8: F785LP flat showing strong, broad residual streaks. The F122M pattern has been divided out. The intensity scale ranges from 0.93 (black) to 1.018(white).

Persistent measles.

These features, shown above in Figure 2, appeared in February 1992 and thus are absent from flats currently in the CDBS. They cause ~1 percent errors in the WFC and most of PC6 at F555W. Larger errors of 2 to 5 percent appear in some parts of PC6 and much of the other PC chips, with PC8 being the most serious. Delta flats can be used to locate the measles relative to the targets, and will show whether they will impact the scientific results. The Delta flats can also be multiplied into the science images as a correction; a Deltaflat close in time and wavelength to the observation should be used. In general, these corrections will work best for extended targets, where the internal flats and science data have similar illumination patterns. We may attempt to deliver improved Delta flats for use with the Cycle 3 closure flats.

Scattered light and flat field edge droop.

Earth flats and internal flats taken when the CCD windows are heavily contaminated will show reduced intensity at the chip edges, but most science data (uncrowded star fields, small galaxies) will not show this effect. The intensity error can be up to about 8 percent at the CCD edges at 4000 Å, but will be only about 5 percent at 5500 Å, and less than 1 percent at 8000 Å. Short wavelength images requiring precise flat fielding may be corrected by comparing internal flats at those wavelengths and close in time to the Earth-cal observations and science observations. Some estimate of the effect, and an empirical correction, can then be derived and applied to the calibrated science data.

VI. Advice to Observers

It is important for observers to recognize the characteristics of their own data, so they may concentrate only on those problems which limit their particular science goals. For example, if you have low signal-to-noise data, then you should probably ignore flat field problems altogether. In most cases there is little sky background, so that errors in flat fielding do not affect object detection. So, for faint targets, it is probably more profitable to concentrate on improving bias, preflash, and dark current subtraction.

For high signal-to-noise data involving small targets at the WF2 or PC6 default aperture positions, one can ignore neutral density filter gradients and patterns, as well as edge-droop effects. One should look at both the flats and Delta flats to check that there are no strong features on the target. If several observations with different pointings are available, their results can be compared to check small-scale errors in the flats and corresponding errors in the photometry.

Situations involving wide-field imaging (e.g. star clusters) will be more difficult. Observers should first check whether the F122M filter was used when observing the calibration flat for their data; this can be checked in the STEIS memo on calibration reference files (Baggett and MacKenty 1993b). If the F122M filter was used, they can attempt to remove its pattern using flats nearby in wavelength (e.g. Figure 5). And again, they should look for strong features (dust, etc.) near their targets in the flats

and Delta flats, and perhaps multiply the Deltaflat into their image as a (partial) correction.

We also emphasize that it is important to experiment and try different flat fields, etc. For many filters there are several flats in the CDBS; these are sometimes taken with and without neutral density filters, or use long vs. short exposures. There are also pre-launch flats, and while these will lack the OTA illumination pattern, they may have some benefits. The spectral properties of the target should also be considered, for example, line emission sources observed in broad-band filters might flatten better with the appropriate narrow-band flat. In summary, given the various problems and complications impacting WFPC flat fielding, it is probably true that there is no single correct way to flatten the data; instead it is a matter of choosing the compromises which give an adequate result without undue effort.

VII. Future Plans

We are in the process of obtaining about 1300 new Earth-calibration exposures as part of the Cycle 3 closure calibration. These include observations of most filters alone, and many crossed with both the F122M and F8ND filters. Our goal is to deliver a complete set of new calibration flats for most filters in 1994. We will attempt to remove the neutral density patterns wherever possible, by using both ratios derived from the Earth-cals and from sky flats. The beautiful work on sky flats by the MDS groups provides a powerful tool for deriving and checking removal of the neutral density patterns. We may also attempt to derive sky flats in other filters besides F555W and F785LP, provided there is sufficient data in the archive.

Finally, we emphasize that input from the user community is welcomed and solicited, regarding not only flat fielding, but all aspects of WFPC calibration. The user community, as a group, have unparalleled expertise and resources, and it is our sincere hope these considerable capabilities may be brought to bare on difficult aspects of WFPC calibration.

VIII. Further Information

Additional information regarding the WFPC flat fielding can be found in:

- Image headers for flat field calibration files. These contain descriptions of how the reference files were derived.
- Selected WFPC Instrument Science Reports and Memos, available from STScI Science Instruments Branch.
- Space Telescope Electronic Information Service (STEIS) Memos, which are available by anonymous FTP to internet node stsci.edu. These contain up-to-date information on calibration reference files, etc.
- STSDAS Calibration Guide, available from STScI User Support Branch.

- WFPC Handbook, available from STScI User Support Branch.
- WFPC Final Orbital / Science Verification Report, 1992, ed. S. Faber, available from STScI User Support Branch.
- WFPC Instrument Science Reports and Memos, available from STScI Science Instruments Branch.

References

- Baggett, S. M. and MacKenty, J. W. 1993a, WFPC Deltaflat Corrections, (available on STEIS).
- Baggett, S. M. and MacKenty, J. W. 1993b, WFPC Reference Files Currently in the Calibration Data Base, (available on STEIS).
- Hester, J. 1992, in WFPC Final Orbital / Science Verification Report, ed. S. Faber, (available from STScI User Support Branch).
- MacKenty, J. W. and Baggett, S. B. 1992, Measle Contamination and Compensation with Delta Flat Fields, (WFPC Instrument Science Report 92-04, available from STScI Science Instruments Branch).
- MacKenty, J. W. 1992, Hubble Space Telescope Wide Field and Planetary Camera Instrument Handbook, v. 3.0, (available from STScI User Support Branch).

Flat-Fielding and Photometric Accuracy of the WFC with F555W and F785LP

Andrew C. Phillips¹, Duncan A. Forbes¹ and Matthew A. Bershad¹

Abstract

Deep F555W and F785LP exposures with the Wide Field Camera (WFC) show gradients in the sky background at a level of 10–20 percent following pipeline calibration. These gradients also appear in stellar photometry and thus must be the result of inaccurate flat-fielding. Applying corrections to the flat-field frames based on the background structure leads to an improved internal accuracy of ~4 percent for single-measurement photometry, compared to the ~10 percent accuracy suggested by previous studies. Re-analysis of calibration photometry leads to new zero-points for F555W and F785LP which have internal consistency at a level of ~1.2 percent, based on comparison between the chip-to-chip offsets and the sky levels observed in corrected images.

I. Introduction

Early long-exposure WFC images obtained as part of the *Medium Deep Survey* (MDS) key project showed structure and gradients in the sky background at a level of ± 10 percent following pipeline calibration. It was originally believed that this structure was an additive component arising from scattered earthlight, but this is unlikely because:

- the structure appears similar in images of different exposures, epochs and pointings (i.e., different orientations of the telescope with respect to the sun and earth); and
- the structure is quite different in the two passbands we used; while changes in amplitude might be expected from scattered light, large changes in *spatial* structure are unlikely.

Furthermore, Hester (1992) [IDT Report] strongly cautions that there are problems with the accuracy of the broad-band flat-fields.

We have found photometric evidence that the pipeline calibration frames, C191513JW.R6H (F555W) and C1915143W.R6H (F785LP), are in error by as much as 20 percent (peak-to-peak) across a single WFC chip. We have derived a first-order correction to these errors and have re-analyzed the IDT Report photometry (Hunter et al. 1992, in the Final Orbital/Science Verification Report) to derive new zero-points. A more detailed description of this investigation is given in Phillips et al. (1993).

1. Lick Observatory, University of California at Santa Cruz, Santa Cruz, CA 95064

II. Scattered Light or Flat-Fielding Errors?

We examined multi-orbit F555W and F785LP images of a high galactic, low ecliptic latitude field acquired in January 1992, as part of the MDS. The sky background in each filter/CCD combination was fit interactively with a bi-cubic spline surface fit, carefully rejecting all objects. We estimate these fits are correct within 1–2 percent. The F555W surface fits for WF1–WF3 were modified to crudely remove the doughnuts or pupil images (Hester 1992); the F785LP surface fit had a correction applied to remove the odd-even pattern in the pipeline flat.

Is the background structure multiplicative or additive? To address this question, we selected an MDS field in the SMC which contained numerous well-exposed stars, and which was observed on two occasions, 19 and 21 November 1992. The two sets of observations were offset by about 17 arcsec (~ 170 pixels), allowing us to perform differential photometry between different areas of the chips. We examined the worst case – the WF2/F785LP combination – and selected 17 relatively isolated stars which appeared in both sets of observations. Aperture photometry was performed with the IRAF APPHOT package.

Ratios of the photometric measures for each star from November 19 and from its offset position on November 21, are compared to the ratio of the surface fits values in the two corresponding positions. Figure 1a shows the ratio of the sky values in the overlapping fields compared to the ratio of the F785LP surface fit. There is a clear linear correlation present, confirming what we have qualitatively noted above: the structure in the background is fairly constant over time, in this case the 10 months from January to November 1992. Figure 1b shows the ratio of the count rate for each star in a 1.0 arcsec radius aperture vs. the surface fit ratio. These ratios have been corrected for PSF variations using model PSFs created with Tiny Tim (Krist 1992). *The correspondence between object photometry and background structure proves the structure is multiplicative and is due to incorrect flat-fielding.*

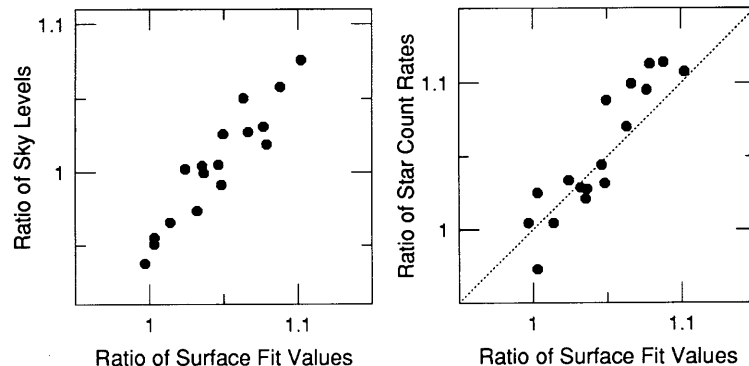


Figure 1a: Ratio of sky values vs. ratio of surface fit values for WF2/F785LP. The sky values are from annular sky apertures around each star and may be somewhat contaminated by other objects, but this should be removed in the ratio to first order. The ratio is formed from the 19 November vs. 21 November observations. The ratio in the surface fit is formed from the corresponding (offset) positions of each star on the two dates. **Figure 1b:** Ratio of the stellar fluxes vs. ratio of surface fits, as in Figure 1a.

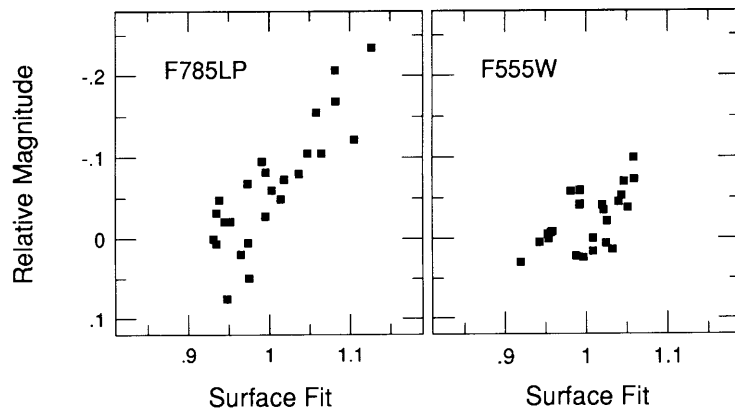


Figure 2: Photometry of HD151406 vs. normalized surface fit at different positions across WF2. Shown are *F785LP* (left) and *F555W* (right).

As another test, we obtained archived images taken as part of the WFPC PSF Calibration Program (see Baggett & MacKenty 1993). In these images, the bright star HD151406 ($V \approx 9$) was imaged in a 5×5 grid of positions across WF2. We performed aperture photometry using a large aperture, and compared the resulting stellar magnitudes to the surface fits at the appropriate position on the chip, shown in Figure 2. There is a very clear correlation between the photometry and the surface fit in *F785LP*; in *F555W* the correlation is also present. The dispersion in Figure 2 is 0.036 (*F555W*) and 0.040 (*F785LP*) magnitudes, implying that single-measurement photometry to ≤ 4 percent is more representative than the ~ 10 percent limit on accuracy found by Hunter et al. (1992) and Holtzman et al. (1991).

III. New WFC Zero-Points

The surface fits provide a first-order correction to the pipeline flat fields. Knowing something about the systematic errors involved, we can re-analyze the calibrating photometry in the hopes of improving the zero-points. We selected the ω Cen photometry of January 1992 (Hunter et al. 1992); because it was acquired within a few days of our surface fit data, we are assured that contamination effects will be the same in both. The Hunter et al. photometry is given in their Table 12.12. We find that most of the data follow the expected linear relationship between photometry and corrections derived from the surface fits. However, we find all stars less than 50 pixels from the edge of the pyramid shadow tend to be discrepant, so we have excluded these stars in our analysis. In the *F785LP* data, we have also excluded the short exposure measurement of star 1655 because it differs from its long exposure counterpart by over 0.25 magnitudes. There is still evidence of smaller anomalies in the remaining data set.

Hunter et al. weight their averages by the formal DAOPHOT measurement errors, which in *F785LP* are typically ≤ 0.01 mag. Some of the *F555W* error estimates are equally small. However, the dispersion we find is considerably larger than these errors. Under these circumstances, it is inappropriate to use weighted averages based on the formal error estimates. We have therefore combined the data with equal

weighting, and applying the same contamination values as Hunter et al. we derive new zero-points, shown in Table 1. Zero-points have been calculated using the original (uncorrected) Hunter et al. photometry (column 3) and with the surface-fit corrections applied (column 4). Between these two equivalent sets, we see a significant improvement in the dispersion when the corrections are applied.

Table 1

Chip (1)	Filter (2)	C^{IDT} (3)	$C^{\text{IDT}}(\text{corr})$ (4)	C^{F93} (5)	$-\Delta\Sigma(\text{Sky})$ (6)	$\Delta C^{\text{IDT}}(\text{corr})$ (7)	ΔC^{F93} (8)
WF1	F555W	22.881(.062)	22.902 (.024)	22.80(.04)	-0.098	-0.083(.007)	-0.11(.01)
WF2	F555W	23.033(.033)	23.036 (.039)	22.97(.05)	0.059	0.052(.010)	0.06(.01)
WF3	F555W	23.059(.089)	23.040 (.061)	22.98(.03)	0.072	0.056(.017)	0.07(.01)
WF4	F555W	23.002(.089)	22.959 (.042)	22.89(.04)	-0.034	-0.025(.015)	-0.02(.01)
WF1	F785LP	21.562(.032)	21.564 (.041)	21.46(.13)	0.023	0.039(.011)	-0.14(.03)
WF2	F785LP	21.599(.079)	21.635 (.035)	21.62(.10)	0.107	0.110(.010)	0.02(.03)
WF3	F785LP	21.457(.101)	21.436 (.086)	21.61(.05)	-0.077	-0.089(.020)	0.01(.01)
WF4	F785LP	21.473(.077)	21.465 (.072)	21.70(.04)	-0.053	-0.060(.026)	0.10(.01)

1. CCD Chip
2. Filter
3. Recalculated zeropoints (and dispersions) from the uncorrected data in Table 12.12 of Hunter et al. (1992)
4. New zeropoints derived from corrected photometry, as described in text
5. Zeropoints from Freedman et al. (1993); the F555W values are actually for a V -band conversion
6. Sky offsets relative to mean value, in negative magnitudes
7. Column (4), relative to mean value (errors are standard deviation of the mean for the zeropoint value)
8. Column (5), relative to mean value (errors are standard deviation of the mean for the zeropoint value)

V. Sky Offsets – A Validity Check

While the sky brightness itself cannot be used to determine *absolute* zero-points, it can be used to independently measure the zeropoint *offsets* between the four chips, since the sky background should have the same value everywhere. The sky offsets are shown in Column 6 of the table (relative to the average of the four chips), along with the offsets from the re-analyzed IDT photometry and the Freedman et al. zero-points (Columns 7 and 8). The new (corrected) zero-points are now in excellent agreement with the observed sky offsets, with an average difference of 0.012 and 0.011 magnitudes rms in F555W and F785LP; the differences are at the level expected from the standard deviation of the mean for the zero-points. This gives us confidence that we are analyzing the data correctly, and that the calibration has an *internal* accuracy of better than 2 percent.

Conclusions

- The accuracy of the flat-field calibration of WFC is considered by examining the sky in long MDS exposures. Large-scale gradients of order 10–20 percent are found in F555W and F785LP following pipeline calibration.

- Stellar photometry shows a correlation with the background variations, demonstrating that the variations are due predominately to errors in the flat-fielding.
- Correcting the photometry in the IDT report (Hunter et al. 1992) for the flat-field errors leads to an improvement in the dispersion in zeropoint measurements within each CCD. New zero-points have chip-to-chip offsets which are consistent with the observed sky levels to within 1.2 percent rms.

Researchers wishing to do relative photometry to better than 0.1 magnitude with the WFC will need to make appropriate corrections for the flat-fielding errors. With such corrections, it appears that photometry as good as 1–2 percent should be achievable.

The ideal way to determine the flat-field calibration is to median or otherwise filter and combine a large set of unregistered or independent frames, creating a so-called super sky flat. This effort, using a 100 image data set, is currently underway by the MDS group (Ratnatunga et al., this volume).

References

- Baggett, S. M., and MacKenty, J. W. 1993, *WFPC Instrument Science Report 92-10*, STScI, Baltimore.
- Freedman, W., et al. 1993, *ApJ* (in press)
- Hester, J. 1992, in *WFPC Final Orbital/Science Verification Report*, ed. S. Faber (Baltimore: STScI), Chapter 6
- Holtzman, J., et al. 1991, *ApJ*, 369, L35
- Hunter et al., D., Faber, S., Light, R., and Shaya, E. 1992, in *WFPC Final Orbital/Science Verification Report*, ed. S. Faber (Baltimore: STScI), Chapter 12
- Krist, J. 1992, *The Tiny Tim User's Manual* (Internal STScI document)
- Phillips, A. C., Forbes, D. A., Bershad, M. A., Illingworth, G. D. and Koo, D. C. 1993, submitted to *AJ*

Calibration of *HST* WFPC Images for Quantitative Analysis of Faint Galaxy Images

Kavan U. Ratnatunga¹, Richard E. Griffiths¹, Stefano Casertano¹
Lyman W. Neuschaefer¹ and Eric W. Wyckoff¹

Abstract

Accurate *V* and *I* flat fields for the Hubble Space Telescope Wide Field Camera have been obtained using the sky background in images taken for the Medium-Deep Survey, a Key Project. These super-sky flat fields have pixel-to-pixel rms variations of about 2.2 percent in *V* and 2.4 percent in *I* and are uniform to better than 3 percent peak-to-peak over almost all the exposed area. Super-sky flat fields can increase photometric accuracy of WFC images by about a factor of 3 with respect to Earth flats and because of the low level of illumination are better suited for quantitative study of faint images in deep exposures.

I. Introduction

The pipeline calibration established by the STScI for Wide Field and Planetary Camera (WFPC) images (MacKenty et al., 1992b) addresses the needs of the majority of primary observers, who typically have small observation sets with well exposed images for their targets of interest. The Medium Deep Survey (MDS) Key Project (Griffiths, et al., 1993) includes observations of a large number of random fields extending over multiple years and focuses on the properties of the faintest measurable objects found serendipitously. Accordingly, much effort in the early stages of the MDS project has been devoted to improving upon the pipeline calibration and selecting the optimum set of procedures to minimize observational errors. This is particularly important for quantitative analysis of faint extended sources with low signal-to-noise ratio.

While a primary (non-WFPC) observation executes a long uninterrupted integration, up to 40 minutes of parallel observation time are often available during each *HST* orbit. Noise in these observations is typically dominated by the CCD read noise: even for the longest single-orbit observations, the Poisson noise from the photon counts in the sky background contributes less than the read noise. In order to minimize the total noise and to improve the efficiency of scheduling parallel observations for the MDS, each orbit is used for a single WFPC exposure, between 20 and 40 minutes in duration, taken with the F785LP (*I*) or the F555W (*V*) filters. In a few cases, over 10 exposures were taken towards a single pointing; these fields include the deepest WFPC exposures taken so far with *HST*. The images contain mainly background sky counts, and our goal is to extract information on the faint stars and galaxies present.

1. Johns Hopkins University, Baltimore, MD 21218

The STScI WFPC pipeline calibration is based on a sequence of operations (MacKenty et al., 1992a; and see this volume), each of which removes some image artifact at the price of introducing a certain amount of extra noise. Briefly, the observed image is first corrected for the Analog to Digital Converter (ADC) error (Lauer 1989) using a lookup table. Next, a bias level is subtracted, together with the expected dark current for the time between CCD erasure and readout. Finally, flux calibration is ensured by multiplying the image by the inverse of the instrument response (flat field).¹

Bias, dark and flat field frames all contain some measure of noise. The STScI calibration frames were created with the overall goal of achieving a noise contribution below one ADU (Analog-Digital Unit), which is smaller than the typical single-exposure read noise (about two ADU). However, if, as in the case of many MDS fields, several exposures with the same pointing are combined to reduce the image noise, the calibration noise does not decrease in the same way, since the same transformations are applied to each image in the stack. Therefore the noise introduced by the standard calibration process may dominate the total noise if more than three exposures with the same pointing are combined. Similarly, any systematic problems in the calibration, such as the gradients in the flat field that have been reported by Phillips et al. (1993, and this volume), will not be reduced and will become more significant in the presence of a smaller level of noise.

Because of the MDS focus on the quantitative study of the faintest observable objects, we have aimed our calibration strategy at achieving the lowest noise level possible, while at the same time improving the stability of the process and the photometric accuracy of our results. To this end, we have obtained new dark, bias, and flat field frames, taking into account possible time variations in each, and also additional corrections for the Charge Transfer Efficiency error. As a result, we have reduced the calibration-induced noise by 0.3 mag and the variation in the CCD response by a factor of at least 3.

In this contribution we discuss in detail our new super-sky flat fields, which are perhaps of general use. The other steps in our calibration strategy are discussed in a companion paper (Ratnatunga et al., 1993). The super-sky flat fields have been obtained using the sky background in a large number of MDS images, and appear to be essentially free from the problems found in Earth and internal flats, such as large-scale gradients, streaks, and other sharp features. At the same time, because they have been obtained at count rates similar to our science data, there is no concern about variations in the pixel-to-pixel response of the camera between high and low levels of illumination. These flat fields are substantially more uniform on both small and large scales than those obtained in the pipeline calibration, and allow much more accurate photometry even for faint objects.

1. A comprehensive review of these steps and the errors associated with the calibrations is given in the article by Biretta in this volume.

II. The Super-Sky Flat Field

a) Sky Background vs. Bright Earth Images

The standard pipeline approach to flat fields is to obtain exposures of the bright Earth as the *HST* field of view streaked across it (MacKenty et al., 1992a). These have the advantage of very low photon noise, because of the large signal accumulated in a short time. At the same time, they present several potential problems, especially for our goal of obtaining accurate photometry of faint objects.

First, the surface brightness of the Earth is not constant; as the spacecraft moves during the exposure, this produces streaks at a characteristic angle. The streaks can to some extent be removed via software developed by the WFPC IDT (Faber 1991). An improved version of this software has been implemented in STSDAS. In the IDT version of the software, some of the image processing was done with integer computations, which left a residual pattern identified by Phillips et al. (1993) using a subset of the MDS F785LP images. This problem was completely resolved by restacking the original Earth flats with the STSDAS version of the software. In some cases, however, the number of streaked flats available is insufficient for proper removal of the streaks, especially if the streak angles are similar.

Second, the surface brightness of the Earth is so high that the signal has to be reduced somehow to avoid saturation in the wide filters even in short exposures. For the F555W filters, for example, this has been achieved by coupling it with the F122M filter; the latter has a red leak that acts as a neutral-density filter, with an effective signal reduction of about 8 magnitudes. However, it is now apparent that the red leak is not uniform across the field of view; this introduces variations of up to 30 percent (peak-to-peak) in the system throughput. For the F785LP filter, flats created with and without the F122M filter are significantly different, which confirms that the latter filter is at least partly responsible for the problems.

Third, large doughnut-like features are seen, particularly in the *V*-band (MacKenty et al., 1992b, Hsu and Ritchie 1993); these appear to be images of the secondary mirror assembly, due either to pinholes in the filter or to back-reflected light.

The net result of these problems is the existence of severe problems in the flat fields, including large gradients and large-scale non-uniformities (of order 10–15 percent in each chip) and other sharp features such as doughnuts, all of which become apparent as (artificial) variations of the sky background when the flat fields are applied to sufficiently deep exposures. Some of these problems have already been pointed out and partly corrected by Phillips et al. (1993) using the first set of MDS exposures.

Another, more fundamental problem which may specifically affect faint images is that the back-illuminated CCDs in the WFPC are prone to quantum efficiency hysteresis effects (Janesick et al., 1985; Griffiths 1985). The camera was UV-flooded at the end of 1990, and during the course of the subsequent *HST* safings and decontamination episodes, the CCDs may have experienced some loss of the charge introduced by the solar UV-flood: this loss is highly non-uniform, with the corners of the CCDs and small, protruding areas on the CCD surfaces losing charge more rapidly than other areas. The effective QE in these areas, as measured in the Earth

flat with a high level of illumination, can be quite different from the effective QE for the low-level illumination present during the MDS observations. Consequently, in those areas, the Earth flats are not directly applicable to the faint images in which we are most interested. Conversely, Earth flats may be more appropriate than ours for bright images with high signal levels.

b) Flat Fields from the Sky Background

The MDS team has used a completely different approach from Earth flats to measuring the pixel-by-pixel variation of instrumental response. We have taken advantage of the fact that a large fraction of our observations contain essentially uniform sky, with a few weak sources scattered randomly across the field. This allows us to build a super-sky flat from the data themselves (see, e.g., Tyson 1990). The basic assumption is that the background sky level is spatially constant through each observation, once individual objects have been removed. This obviates both of the main problems with the earth flats, since no additional filter is required, and the flats are obtained from observations at the same count levels as our science data.

Ideally, the super-sky flats should be assembled from data taken with the camera under constant environmental conditions, i.e. at the same level of contamination of the field-flattening lenses covering the CCDs. Frames accumulated in Cycle 2 between 08/08/92 and 08/02/93 approximately meet this criterion. Care has been taken to ensure that the fields selected for the super-sky flats did not include data frames for which the background had a high level of scattered earthlight (recognized by their high absolute levels and shadowing caused by mirror support structures).

Although approximately constant in each observation, the sky background does vary from observation to observation, depending on ecliptic latitude, Sun Angle and average Earth Limb Angle. Different observations need to be scaled to a common mode with appropriate weights. For this purpose, we had to modify the STSDAS COMBINE task, in which we found a multitude of serious and non-trivial errors which were especially problematic when combining and scaling images according to exposure time and/or mode.

The final stack used to determine the super-sky flat includes 79 frames for the F785LP filter and 56 frames for the F555W filter. No more than three images with the same pointing have been included in either stack. Since the images all have different pointings, at each pixel a clipping algorithm has been used to eliminate the high values, which could be due to cosmic rays or to astronomical objects. (Note that this process cannot generally be used with primary observations, which would be likely to contain target objects positioned preferentially at the center of a CCD or of the overall field.)

Table 1: Characteristics of Super-Sky Flat

Filter	F555W	F785LP
Images	56	79
Mean Exposure (sec)	1650	2350
Mean Counts (ADU)	18.2	18.8
Expected rms error (raw)	2.8%	3.3%
Measured rms error (raw)	3.1%	3.4%
Final measured rms error after combining with Earth flat	2.2%	2.4%

The mean properties of each flat field are tabulated in Table 1. With an average sky background of 18 ADU, and 50–80 independent frames, a major contributor in the noise of the final flat-fields is the noise in the calibration frames, especially the dark. After the improvements in our calibration procedures, we obtain a pixel-to-pixel variation of about 3.1 percent in V and 3.4 percent in I . The rms noise expected from read, dark, and other known sources of noise is 2.8 percent and 3.3 percent respectively, very close to the measured values; this indicates that there are no significant unexplained sources of noise.

Although these flats appear already much better than the Earth flats, there is still room for some improvement. The Earth flats, with their larger signal, have a lower fractional pixel-to-pixel variation on small spatial scales. We have attempted to use this valuable small-scale information by applying a simple filtering algorithm, in which each pixel value is determined by multiplying a smoothed version of the super-sky flat by a destreaked, flattened Earth flat. The final flat fields thus produced have an rms pixel-to-pixel variation of 2.2 percent in V and 2.4 percent in I (rms), and are free from all the artifacts present in the Earth flats, such as gradients, doughnuts, streaks. The quality of the pipeline flat fields can be gauged by flattening them with the higher-quality super-sky flats; the result is shown in Fig. 1 in the form of a contour map.

c) Photometric Zero Point

The removal of the large-scale gradient present in the pipeline flats also improves significantly the photometric quality of the WFC. We estimate that, after including all sources of error, photometry with the WFC can be accurate to about 0.03 mag over all four chips, edges and other obvious (small) defects excluded. Because systematic effects in the flat fields are reduced, there is no need for separate photometric zero-points for the four CCDs, which were required to compensate for the different responses assigned to different chips.

The best values for the zero points to be used with our super-sky flat fields are 22.84 ± 0.01 in the V band and 21.47 ± 0.02 in I . These values are in acceptable agreement with those obtained by Phillips et al. (1993) from a subset of MDS fields, and also with those derived by Freedmann et al. (1993).

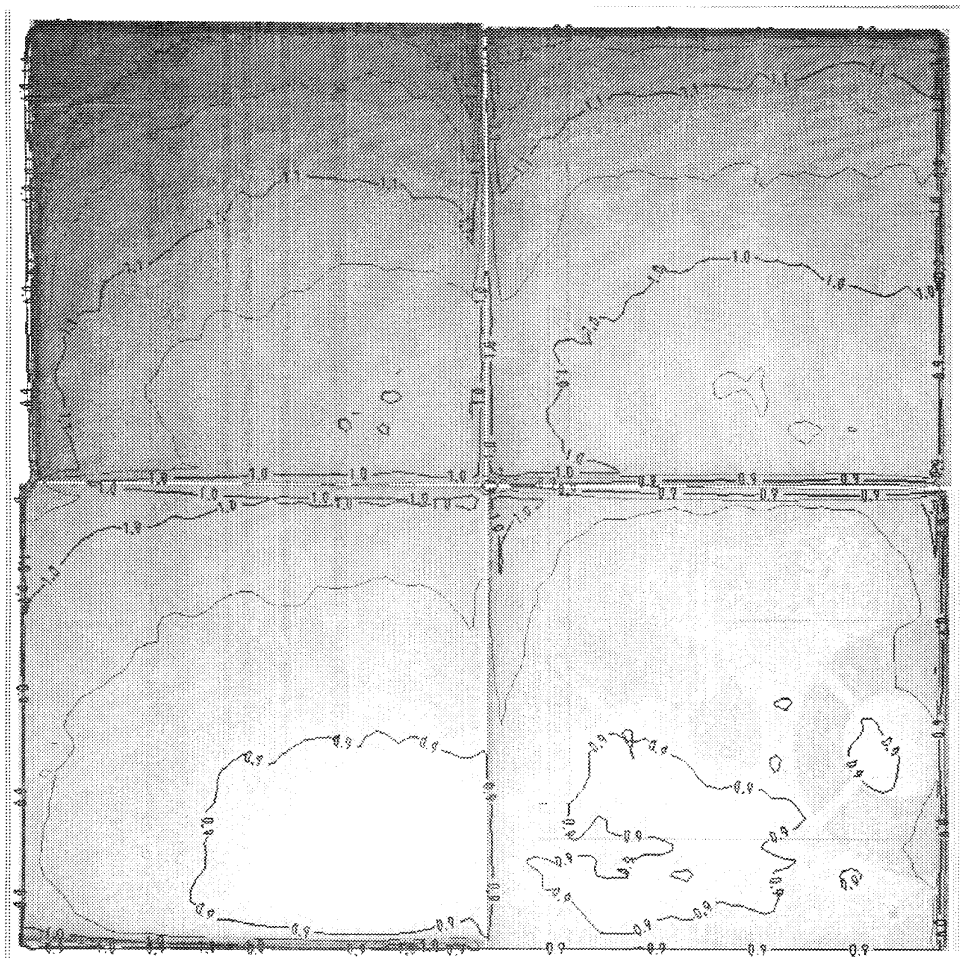


Figure 1: The large gradients and doughnuts in the pipeline F555W flat appear clearly when the pipeline flat is corrected with the super-sky flat.

d) Sky Brightness, Scattered Light, and Stacking of Images

Since super-sky flats are based on the assumption that the background sky brightness is constant across the field of view, special care must be exercised to ensure that no contamination from other sources of light is present. This includes large-scale variations from large nearby objects, such as bright galaxies (small objects in the field of view are excluded from the image-to-image comparison, and average out because of their random placement), scattered light, and gradients in the sky brightness itself.

The sky brightness depends on where the telescope is pointed. The main contributors to the background light are zodiacal, which depends on ecliptic angle, airglow, and scattered light, which depend on Sun angle and Earth limb angle. However, a change in overall sky brightness is benign for us, as long as the optical path through the telescope is the same, since it only offsets the image by a constant (after flat fielding). The concern would be a measurable gradient in the sky brightness in a single field, that is, over scales of order 3 arcmin.

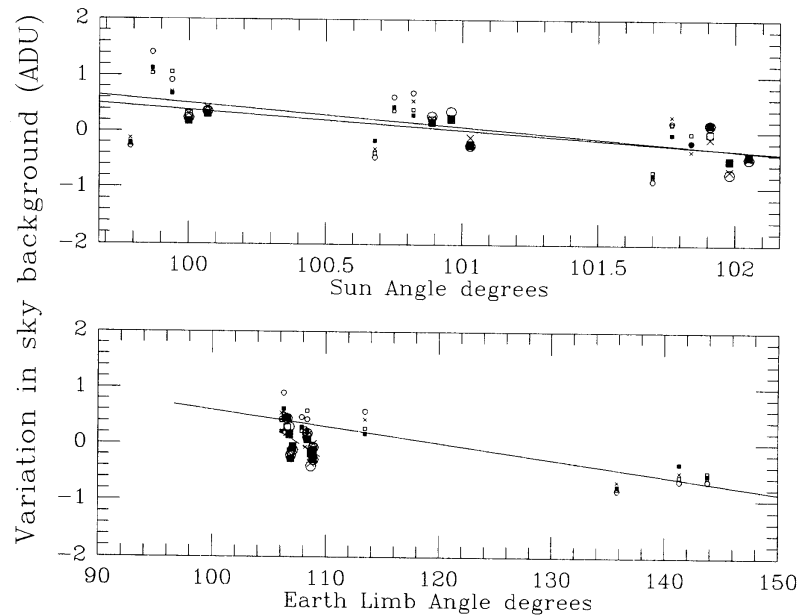


Figure 2: Change in the sky background among several observations of the MDS field near 3C273 in the three days of observation. The sky background level is determined in each exposure from the mode of the observation, separately for each CCD. Top: variation in sky background as a function of Sun angle. Bottom: residual as a function of Earth limb angle, after removal of a linear term in Sun angle. Within the 0.25 ADU precision of each measurement, the background is the same for all CCDs, indicating that any scattered light is distributed uniformly over the four chips and that any overall gradient is negligible.

We have attempted to put limits on any gradient in sky brightness in two different ways. First, we find no measurable variations in the sky brightness of individual images at the 1 percent level (peak-to-peak in 100-pixel squares), after reduction with our super-sky flats and object removal. This is the case even for images with very different sky background levels, including one taken at only 51° Sun angle which has a background 4 times higher than all others. Second, we have measured the change in the sky background among several observations of the MDS field near 3C273. In the three days of observation, the Sun angle increased from 100° to 102° . Most of the observations were taken at an average Earth limb angle of 105° , with some taken at 140° . The sky background level was determined in each exposure from the mode of the observation, separately for each CCD, with an error of 0.25 ADU (see Fig. 2). Within the precision of the measurement, the background is the same for all CCDs, indicating that any scattered light is distributed uniformly over the four chips and that any overall gradient must be small. Furthermore, the variations with Sun angle and Earth limb angle are small, consistent with 1 percent and 0.2 percent per degree respectively in this range. Both point at very small variations over the 3 arcmin scale of individual images. We conclude that, even if scattered light is present, as it almost certainly is, it is transmitted through the Optical Telescope Assembly just like all other light to a sufficiently good approximation (as far as our flats are concerned), and thus it introduces no adverse effect in either images or super-sky flats.

A final, related consideration concerns the stacking of images of the same field.

Coincidence routines, used to remove cosmic rays and other imperfections, typically rely on expecting the same signal at the same position. When the calibration is carefully conducted, the day-to-day variation in sky background is significant with respect to the noise, and therefore it must be corrected to avoid false rejections. At the same time, the typical sky level must be retained in order for the noise model to predict the image noise properly. Ideally, the measured signal should be used to determine the noise contribution from each image in the stack, while the corrected signal (flat-fielded and sky-subtracted) should be used in combining the images. Proper implementation of this method requires in principle retaining a separate noise image, which is not possible with current STSDAS software.

On the other hand, if all images in the stack have the same pointing, the flat-field correction can be applied after stacking, and an acceptable compromise is to correct images by a small additive constant to bring them to a common sky background. The mode offset option in the image combination tasks would be very effective for this purpose. Unfortunately, in their current (November 1993) incarnation, the relevant STSDAS tasks appear to suffer from several limitations, restrictions and bugs which have made our path fairly treacherous. We recommend careful evaluation, especially of issues of scale and weight calculation, combination of substacks, and proper noise model, before using the current STSDAS tasks. Even after removing existing bugs, the current incarnation of the image-combination software in STSDAS cannot properly deal with the stacking of overlapping images with different pointings, for which flat-field corrections must be applied before stacking, and therefore the information on the noise at each pixel is lost. A better program, which computes an error image as well as the combined image, is required for this case to be addressed properly.

III. Conclusions

Detection and quantitative study of faint objects in WFPC images is possible if the appropriate effort is put into the calibration process. The camera is sufficiently stable for good photometric performance (at the 3 percent level or better). However, especially for faint objects, calibration is an important source of both noise and systematic effects which have proved rather stubborn. In order to achieve a better performance in both sensitivity and photometric stability, we have augmented the standard STScI pipeline calibration with some additional procedures. Noise in the bias and dark frames has been reduced by judicious filtering, which includes removing known patterns and smoothing over scales where nothing but noise appears to be present.

A more significant improvement is given by the use of so-called super-sky flat field images, obtained from a combination of the sky background at many different pointings, instead of Earth flats. The latter suffer from streaks and non-linearity, and also from large-scale inhomogeneities at the 15–20 percent level which are difficult to eliminate. Super-sky flats are shown to be repeatedly flat at the 1 percent level over scales of several pixels, and are better-suited for faint objects because of the lower level of illumination compared with the Earth flats. Earth flats are useful in combination with super-sky flats to remove the high-frequency noise component to which the sky background, with its lower signal level, is more sensitive.

Our calibration procedures improve significantly both photometric accuracy and sensitivity for faint images. Photometric accuracy is 0.03 mag, or a factor of 5 better than that obtained with standard procedures, mainly because of the use of super-sky flat fields. Sensitivity is improved by about 0.3 mag, corresponding to about a factor 2 in observing time, thanks to the reduced noise in the calibration files, especially bias and dark.

The improved calibration files have been made available to the community through STEIS.

This work is based on observations taken with the NASA/ESA Hubble Space Telescope, obtained at the Space Telescope Science Institute, which is operated by the Associations of Universities for Research in Astronomy, Inc., under NASA contract NAS5—26555. Coordination and analysis of data for the Medium-Deep Survey is funded by STScI grants GO 2684.0X.87A and GO 3917.0X.91A. We acknowledge the helpful support of the STScI WFPC reduction team in acceding to our frequent requests for additional calibration data, and for extensive and illuminating discussions on various aspects of the calibration process.

References

- Faber, S. M., et al, 1991, 'Final Orbital/Science Verification Report for the Wide Field and Planetary Camera'
- Freedman, W. L., et al, 1993, preprint
- Griffiths, R. E., 1985, Wide Field and Planetary Camera Instrument Handbook, version 1.0, STScI publication
- Griffiths, R. E., et al., 1993, ApJ, submitted
- Janesick, J., Elliott, T., Daud, T., McCarthy, J., and Blouke, M. M., 1985, Proc. S.P.I.E. 570, 46
- Hsu, J. C., and Ritchie, C. E., 1993, Proc. S.P.I.E., in press
- Lauer, T. R., 1989, PASP 101, 445
- MacKenty, J. W., Sparks, W. B., Ritchie, C. E., and Baggett, S. M., 1992a, in 'Science with the Space Telescope,' eds. P. Benvenuti and E. Schreier, p. 595
- MacKenty, J. W., et al., 1992b, 'Wide Field and Planetary Camera Instrument Handbook,' version 3.0, April 1992
- Phillips, A. C., Forbes, D. A., Bershady, M. A., Illingworth, G. D., and Koo, D. C., 1993, AJ, submitted
- Ratnatunga, K. U., Griffiths, R. E., Casertano, S., Neuschaefer, L. W., and Wyckoff, E. W., 1993, AJ, submitted
- Tyson, A. J., 1990, in 'CCDs in Astronomy', A.S.P. Conference Series Vol. 8, ed. G. H. Jacoby, p. 1

Introduction to WFPC Photometry

John A. Biretta¹, Sylvia M. Baggett¹, John W. MacKenty¹,
Christine E. Ritchie¹ and William B. Sparks¹

Abstract

We briefly review photometric analysis and calibration of WFPC images. We discuss absolute calibration using SYNPHOT, and various photometric problems peculiar to WFPC data.

I. Introduction

This paper provides a brief introduction to photometric analysis of *HST* Wide-Field Planetary Camera data. We review a number of resources available to aid photometric analysis, and describe various problems and solutions peculiar to WFPC data. The measurement of raw counts on the images is severely impacted by the spherically aberrated PSF, but PSF fitting and core aperture photometry appear to offer effective solutions. The SYNPHOT synthetic photometry package provides a powerful tool for absolute photometric calibration; we briefly describe its ingredients and usage. A number of problems compromise photometric accuracy. Most of these are rooted in either contamination (throughput variations, measles, scattered light), the use of earth flats (ND filter patterns and residual streaks), or PSF variations (with time and field position). Most of these problems can be minimized or eliminated with some effort.

II. Extraction of Photometric Information from Images

The extraction of photometric information is made difficult by the spherical aberration and the resulting point spread function (PSF) wings. The PSF core, defined to be 0.2 arcseconds in diameter, contains only about 15 percent of the light for a stellar source. A much larger aperture 4 or 5 arcseconds in diameter must be used to measure all the light (Figure 1). Hence there are several competing factors: one would like to measure only the PSF core in order to maximize the signal-to-noise ratio, minimize crowding problems, and ease background subtraction. But on the other hand, a large aperture encircling all the light is required to guarantee photometric accuracy.

Two methods for extracting photometric information have been successfully applied to WFPC images – PSF fitting and core aperture photometry. PSF fitting uses a model PSF and least squares fitting to determine total counts and positions of stellar

1. Space Telescope Science Institute, Baltimore, MD 21218

objects. The model PSF can be either an analytic function or an empirical function extracted from the image itself. Galaxies can be fit also by convolving an appropriate galaxy model with the model PSF before fitting to the image. For this method the signal-to-noise ratio is automatically optimized by choosing an appropriate weighting function for the image pixels. Crowded fields can be dealt with by simultaneously fitting overlapping objects, and the sky level can be simply included in the fit. There are several popular software packages for PSF fitting. The DAOPHOT package by Stetson is described in another paper in this volume. Another package, DoPHOT (Schechter, Mateo, Saha 1993) includes iterative object classification with analytic PSF fitting. The accuracy of this method will generally be limited by the accuracy of the model PSF.

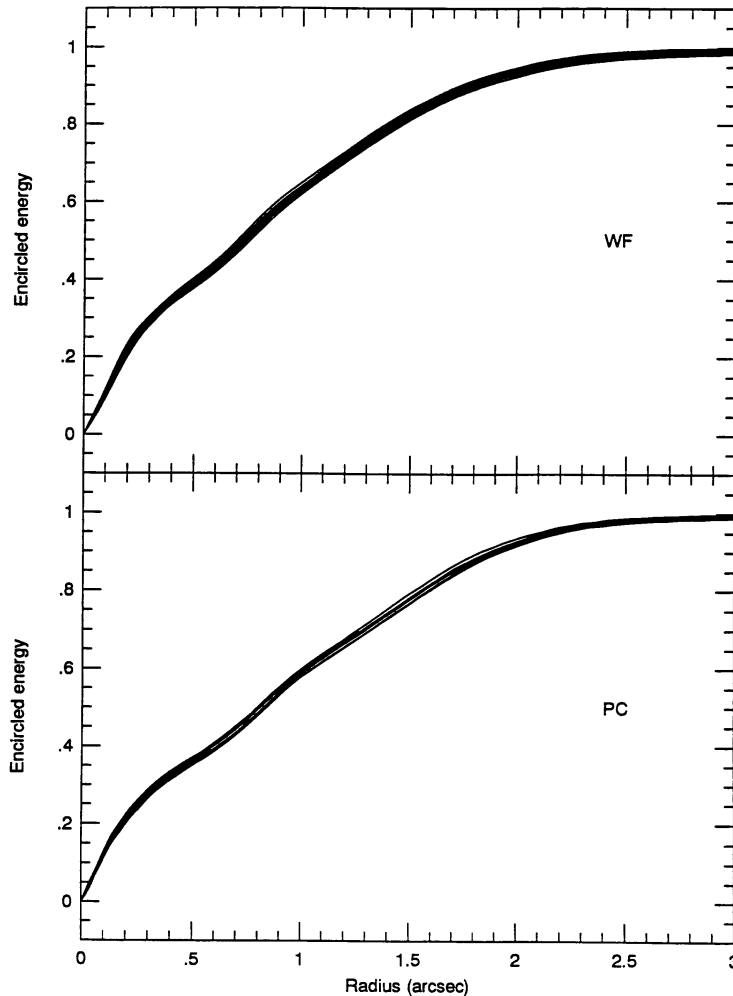


Figure 1: Plots showing encircled energy as a function of aperture radius for the Wide Field (top) and Planetary (bottom) Cameras. From Holtzman (1992).

Core aperture photometry involves measuring only the counts within the PSF core (<0.2 arcsecond radius aperture), and then later correcting the core counts to a larger aperture. The correction may be determined empirically from measurements on bright stars in uncrowded fields, or from measurements on model PSFs. The use of a small aperture serves to both optimize the signal-to-noise ratio and minimize

crowding problems. The accuracy will be limited both by undersampling of the observed PSF by the detector pixels (especially for WFC data), and by variations in the ratio of PSF core light to PSF total light (see section 4 below).

The PSF fitting and core aperture photometry have been shown to give results consistent to about 0.06 magnitudes on bright stars ($m < 18.5$), and a little poorer on faint ones, for the Wide Field Camera (Gilmozzi 1990).

At this point it is appropriate to mention the WFPC PSF library. A library of over 900 observed PSFs is maintained in the Calibration Data Base System (CDBS), which may be accessed through the normal data archive retrieval system. These are short exposures of single bright stars, and cover most of the area of WF2 and the four PC detectors. Most of the observations were made through the F555W and F785LP filters, but small amounts of data are available for twelve other filters. Detailed information on the PSF library is given in Baggett and Mackenty (1993). The TIM and Tiny Tim programs may also be used to compute model PSFs; these are reviewed in other papers in this volume.

III. Absolute Photometric Calibration with SYNPHOT

The SYNPHOT synthetic photometry program is part of the STSDAS package, and is originally based on the XCAL program by Keith Horne. It first derives an effective response function for the total *HST* + WFPC + filter system by multiplying together all the transmission and detection efficiency curves for the relevant components. This response function is then convolved with model spectra to predict observed count rates. Observations can then be calibrated by comparing the predicted and observed count rates for an appropriately chosen model spectrum.

The package is very powerful, in that it allows all possible observation modes to be crossed with a huge variety of model spectra. The *HST* and WFPC throughputs and efficiencies are derived from ground-based measurements which are adjusted to reflect the actual on-orbit performance. Model spectra available in the package include observed stellar spectra, as well as, model power-law, black body and polynomial spectra. The observed spectra include *HST* standard stars and atlases such as the Gunn-Stryker stellar spectral atlas. Other effects, such as reddening, may also be included in the model spectrum. Response curves for standard filter sets are included (e.g. Johnson U, B, V, R, I) so that model spectra may be scaled to arbitrary magnitudes on other systems.

The photometric calibration routinely provided in the calibration pipeline is based on the results of synthetic photometry with the SYNPHOT package. A rough calibration is placed in several keywords in the calibrated data binary header (part of the .COD file); these keywords may be examined with the IMHEAD task in IRAF. This calibration is derived assuming a model spectrum having constant F_λ (defined in units $\text{erg cm}^{-2} \text{sec}^{-1} \text{Angstrom}^{-1}$). The instrument mode assumed for the SYNPHOT calculation is given by the PHOTMODE keyword (e.g. PHOTMODE="PC,5,F,DN,F1042M,OPEN,CAL"), and should be identical to the mode used for the observation. The four keywords containing the resulting calibration are thus:

PHOTFLAM: inverse sensitivity, defined as F_{λ} (in units of $\text{erg cm}^{-2} \text{sec}^{-1} \text{Angstrom}^{-1}$) for a count rate of 1 DN sec^{-1} .
 PHOTZPT: zero-point magnitude (Space Telescope Magnitude at $F_{\lambda}=1$).
 PHOTPLAM: pivot wavelength for the filter in Angstroms.
 PHOTBW: RMS filter bandwidth in Angstroms.

The Space Telescope Magnitude system (STMAG) is based on flux per unit wavelength, or units of F_{λ} , with the zero point set such that Vega has magnitude zero in the Johnson V passband.

```

cl> stsdas
st> hst_calib
hs> synphot
sy> calcpHOT counts wfpc,f555w "rn(bb(5000),band(v),18.6,vegamag)"
Number of modes = 1
Mode = wfpc,wf,2,f555w,cal
      Pivot      Equiv Gaussian
Wavelength      FWHM
5468.423        1199.32      wfpc,wf,2,f555w,cal
Spectrum:      rn(bb(5000),band(v),18.6,vegamag)
      E(B-V)      (COUNTS s^-1 hstarea^-1)
      0.          412.4875
sy>

```

Figure 2: Sample SYNPHOT run for WFPC. Input format is appropriate for SYNPHOT version Nov. 1993. From Bushouse (1993)

Observers may also derive detailed calibrations which are tailored to their target spectra using SYNPHOT. Figure 2 shows a sample run of SYNPHOT program CALCPHOT which computes the expected count rate for a model spectrum. Once in the SYNPHOT package, the single command line "CALCPHOT ..." produces the output shown. Here a calibration is derived for observations made on detector WF2 using the F555W filter. The model spectrum is a 5000 degree Kelvin blackbody re-normalized to a magnitude $V=18.6$ in a system where Vega has $V=0$, and the result is a count rate of $418 \text{ DN second}^{-1}$. Observers should get a copy of the latest and greatest SYNPHOT manual by Bushouse (1993), and check that they have recent versions of the SYNPHOT photometry tables in their STSDAS installation.

We note that the keyword CAL must be specified in the OBSMODE when deriving SYNPHOT calibrations for flat fielded images. The absence of this keyword indicates the data are not flat fielded, and are in units of raw counts.

We now briefly discuss derivation of the SYNPHOT efficiency curves for WFPC. A more complete discussion is given by Sparks, Ritchie, and MacKenty (1992). The

SYNPHOT calibration is based on observations of the UV photometric standard star BD+75325, which were taken on 5 February 1992 immediately following a decontamination. This is sometimes referred to as the “baseline epoch for photometric calibration.” Ten filters covering the range 1900 to 10400 Angstroms were used with detectors WF2 and PC6. Other ingredients to the calibration were ground-based measurements of the WFPC filter throughput curves and distributed quantum efficiencies (DQE) of all detectors, as well as measurements of the inter-chip flatfield corrections from on-orbit measurements. From these ingredients two sets of improved DQE curves were derived for all eight CCDs, one set applicable to un-flatfielded data, and one set applicable to fully calibrated data. These revised curves are incorporated in the current SYNPHOT tables. Some indication of the accuracy of this calibration is provided by the residual scatter in the sensitivities between different filters. This residual scatter is about 6 percent over all the CCDs at wavelengths longer than 3000 Angstroms, and somewhat less, about 4 percent, for data on WF2 and PC6. It is possible that improved flat fielding could reduce this scatter.

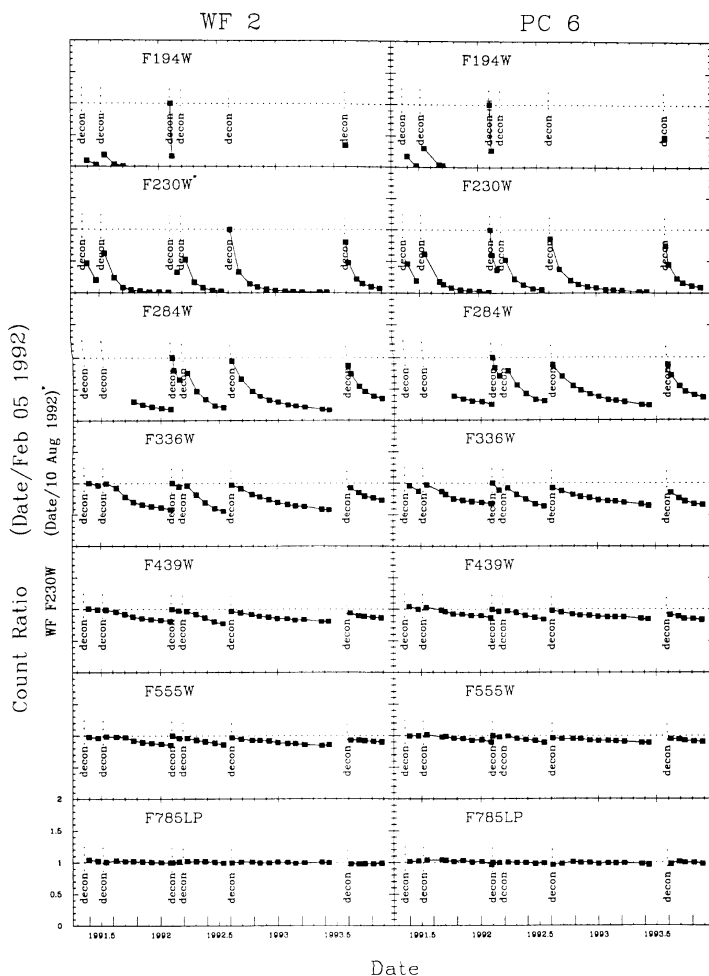


Figure 3: Relative throughput as function of time. Throughput is defined to be unity on 5 February 1992. The left set of panels show the center of WF2, while the right set show the center of PC6. Each small panel shows a different filter, with wavelength increasing from the top to bottom panels. Times of decontamination events are indicated by “decon.” From Ritchie.

IV. Problems Limiting Photometric Accuracy

The WFPC SYNPHOT calibration assumes that all detector pixels have the same response as the centers of detectors WF2 and PC6 on 5 February 1992. Any factors which cause this to be untrue will impact the photometry. We now consider several specific effects which limit the accuracy of the photometry.

Time Dependent Throughput Variations

A quasi-uniform contamination layer builds up on the CCD windows between decontaminations. This molecular layer greatly reduces the instrumental throughput at UV and blue wavelengths. Weekly observations of a photometric standard star on WF2 and PC6 are made to track these variations, and typical results are shown in Figure 3. Since the SYNPHOT photometry and Figure 3 data are both relative to the same date, 5 February 1992, one can simply read the throughput reductions off the graph and apply them to calibrated data.

We will soon incorporate these throughput variations into SYNPHOT by adding the keyword CONT to the OBSMODE. For example:

```
OBSMODE = PC, 6, F555W, DN, CAL, CONT#49020
```

tells SYNPHOT to include appropriate throughput corrections for contamination on date MJD=49020 (Sparks and Ritchie 1994).

Flat Field Effects

Neutral Density Filter Pattern. The red-leak in the F122M filter has been used as a neutral density filter when taking many of the earth flats for broad band filters (e.g. filters F555W, F606W, F675W, F702W, F725LP, F814W, F850LP, etc.). This neutral density filter is non-uniform, and introduces a 30 percent peak-to-peak brightness gradient across all four WFC CCDs. Since this pattern appears in the flats, but not in the actual data, it introduces a corresponding error in the photometry. The Planetary Camera CCDs only view the center of this filter, so the effective gradient is only about 10 percent. There are also donuts where the flats are 2 percent too bright, which are caused by pinholes in the F122M filter.

These patterns introduced by the flats will have little effect on photometry for small targets at the WF2 and PC6 default aperture positions, since the standard stars are also observed there. But there can be a large impact on wide-field photometry. One solution is to derive the F122M filter pattern and then remove it from the images. The pattern can be derived by computing the ratio of narrow band filter flats observed with and without F122M, or by comparing the earth flats using F122M to sky flats.

The neutral density filter patterns also have some impact on the SYNPHOT baseline photometric calibration. The photometry observations on 5 February 1992 were calibrated using flats taken with and without the F122M (and also F8ND) filters, which, since the flats are normalized to unity, introduces a ~6 percent scatter in the

WFC photometric calibration data, and a somewhat smaller in the scatter in the PC. This scatter causes ~3 percent errors in the final photometric calibration, depending on the wavelength and CCD.

Residual Streaks in Earth Flats. The flat fields are derived from observations of the sunlit earth. In cases of short earth exposures (<1 sec) at red wavelengths, these flats will contain streaks caused by the combined effects of spacecraft motion and earth features. While specialized software is used to remove these streaks, it is not always successful, and residual streaks can appear in the flats. These residual streaks have an amplitude of a few percent in many filters, with the worst cases showing streak amplitudes of about 15 percent. The solution is to avoid short exposure earth flats, especially in the red and far-red. If none are available, one should consider using narrow band flats at nearby wavelengths, as these tend to have long exposures.

Short Exposure Reciprocity Effect. The CCD artifacts look different in exposures <1 second and >> 1 second. Apparently there is some change in the QE at very short exposures. The size of this effect is a few percent. The solution is to avoid using short exposure flat fields for long exposure images. This can be accomplished by using ND filters to observe the flats (which have other problems noted above), or use of sky flats, or by using narrow band flats at nearby wavelengths.

Persistent Measles. Decontaminations after February 1992 have been unable to remove all contaminants from the CCD windows. Contaminants consistent with 10 to 15 μm particles remain on the windows, and cause diffractive features (i.e. "persistent measles") about 10 PC pixels in diameter to appear in the images. The amplitude of these features is about 1 percent in intensity for the WFC and most of PC6 in filter F555W. Larger errors, 2 to 5 percent, are seen on some of PC6 and over much of the other PC chips, with PC8 being the worst. The features are relatively stable, though some changes are seen across decontaminations. The easiest solution is to use DELTAFLATs to locate these features, and then decide if they will impact the target. The DELTAFLATs may also be used to correct the data, though this will only be partially successful, since the particles are out of focus. DELTAFLAT corrections will tend to be more successful on extended targets whose illumination pattern more closely matches the internal flats.

Scattered Light and Flat Field Edge Droop. Earth flats and internal flats taken when the windows are heavily contaminated (quasi-uniform layer) show flat field edge droop due to scattering of light by the contaminants. The flats appear bright in the centers, since the scattering angle is small and the photons are detected in nearby pixels. The flats are low at the edges since scattered photons fall outside the CCD detector. Most science data does not show this effect, since only small regions of the window are illuminated, and the scattered photons are simply lost into the background noise. Hence, the application of flats and DELTAFLATs can introduce errors into the data. These effects will cause errors up to about 8 percent at the CCD edges at 4000 Angstroms. At 5500 Angstroms the errors are less than 5 percent, and at 8000 Angstroms less than 1 percent. One can attempt to evaluate this effect for a given flat, by comparing internal flats near the time of the flat field observations, with those taken when the instrument is relatively uncontaminated.

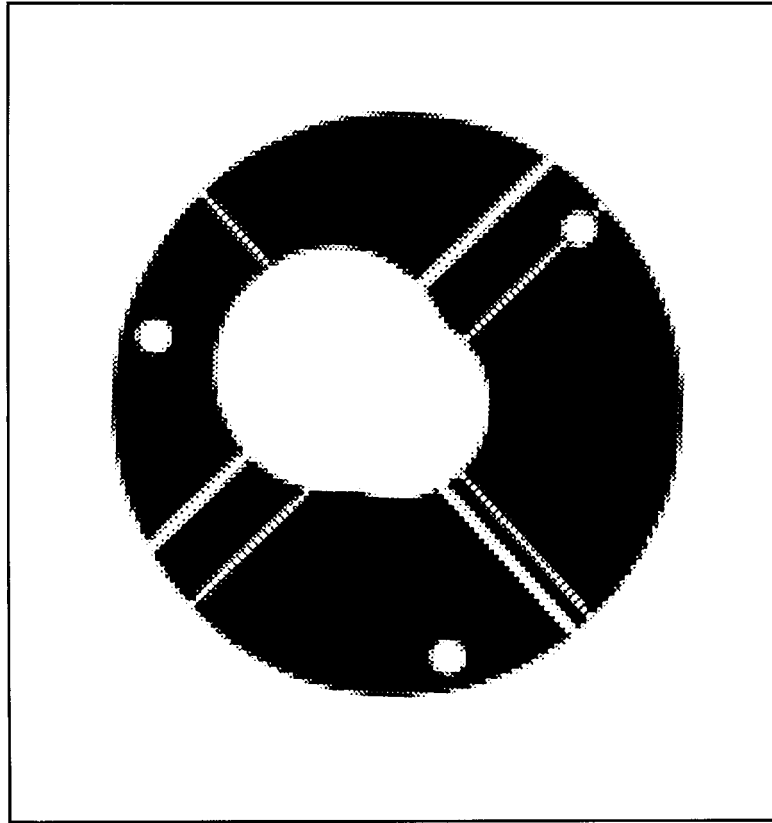


Figure 4: Effective OTA pupil seen by corner of typical WFC CCD. The large circular shadow of the camera secondary, together with its three support posts, have moved significantly off axis. From Holtzman 1992.

PSF Variations.

Variations in the Point Spread Function (PSF) will impact the extraction of photometric information from the images. The PSF varies with both detector position and time.

Variations with Field Position. The PSF varies across each CCD due to vignetting in the CCD camera repeater optics. This has several effects, one of which is to alter the intensity of the PSF core relative to the wings. In the centers of the CCDs, the shadow of the camera relay secondary mirror envelopes the telescope (OTA) secondary mirror shadow, so that the total obscuration is minimized. However, in the CCD corners, the shadow of the camera secondary moves off axis, so that a larger region near the center of the OTA primary mirror is obscured (Figure 4). Since the PSF core and wings are formed by different areas of the primary mirror, this vignetting will alter the relative intensity of the core and wings. (We note that while flat fielding does correct the reduction in *total counts* cause by this vignetting, it does not correct variations in the *relative intensities* of the PSF core and wings.) Variations are also seen in the detailed structure of the PSF wings (tendrils, etc.) as the camera secondary support shadows move and interact with other obscurations in the system.

Images also show a tendency for the PSF core to become elliptical away from the pyramid apex. These PSF variations must be addressed in order to obtain accurate photometry over a wide field of view. Variants of both DAOPHOT and DoPHOT are capable of handling spatially variable PSFs.

Variations with Time. Large changes in the PSF can occur at OTA focus adjustments, which are periodically made to compensate for shrinkage of the OTA mechanical structure. Small variations in the focus (as well as small position shifts) are also seen on time scales near the orbit period. This is sometimes referred to as OTA breathing and is believed to be caused by thermal expansion effects in the OTA. A final effect is that the solar array induced jitter can cause images to trail slightly. This primarily occurs at terminator crossings, but events elsewhere in the orbit are not unknown. These later two effects have short timescales, and will compromise comparison of PSFs on different data frames, or comparisons between data and model PSFs. For observations obtained in fine-lock tracking mode, the Fine Guidance Sensor data can be used to derive a jitter map showing the pointing errors; this can in turn be used to alter the model PSF.

References

- Baggett, S. B. and MacKenty, J. W. 1993, The WFPC Observed PSF Image Library, (WFPC Instrument Science Report 93-03, available from STScI Science Instruments Branch).
- Bushouse, H. 1993, Synphot User's Guide, (available from STScI Science Software Branch).
- Gilmozzi, R. 1990, Core Aperture Photometry with the WFPC, (WFPC Instrument Science Report 90-07, available from STScI Science Instruments Branch).
- Holtzman, J. 1992, in WFPC Final Orbital / Science Verification Report, ed. S. Faber, (available from STScI User Support Branch).
- Schechter, P. L., Mateo, M. L., and Saha, A., 1993, P.A.S.P. 105, 1342.
- Sparks, W.B., Ritchie, C.E. and MacKenty, J.W. 1992, The Absolute Efficiency of the WFPC, (WFPC Instrument Science Report 92-09, available from STScI Science Instruments Branch).
- Sparks, W.B., and Ritchie, C.E. 1994, Time Dependent Synphot Calibration, (WFPC Instrument Science Report 94-xx, available from STScI Science Instruments Branch), in preparation.

The WFPC Photometric System

William A. Baum¹

Abstract

WFPC passbands differ substantially from those of other photometric systems. This paper deals with (1) the calibration of those passbands, (2) the choosing of filters for a photometric system, (3) transformability to other photometric systems, (4) hazards in astrophysical interpretation of WFPC photometric data, and (5) in-flight calibrations of WFPC2 needed to deal with those problems.

For color-magnitude and color-color diagrams of stellar populations, the three recommended WFPC2 filters are F336W, F555W, and F814W. What is needed in addition to conventional flat fields and photometric calibrations is a simple test of the system to see whether those calibrations yield correct astrophysical results. A few short exposures on an already well studied population such as 47 Tucanae would be a very valuable part of the in-flight calibration process.

I. Calibration of the Passbands

Standard star sequences were calibrated from Chile in 1985 using a CCD camera in which the chip and filters were identical in type to those now aboard the *HST*. Results are contained in Harris et al. (1991; 1993) and can be found in data files accessible through the Space Telescope Science Institute.

These ground-based observations included 15 of the potentially most useful WFPC passbands, ranging in nominal wavelength from 336 nm to 1042 nm. The 15 selected passbands are identified in Harris et al. (1991). Following tradition, the zero points of the magnitude scales were adjusted to make A0V stars be of equal magnitude in all passbands, and they were made consistent with Johnson-Cousins *UBVRI* zero points by fitting to Landolt's (1973, 1983) *UBVRI* standards in Kapteyn Selected Areas around the equator.

Standard WFPC sequences were then created in two fields to which the *HST* can be pointed for periodic in-flight calibration. They are located in the outskirts of the globular clusters Omega Centauri and NGC 6752, and are described in Harris et al. (1993). Each calibration field is about 4 arcmin in diameter, and each provides magnitudes in the 15 WFPC passbands for more than 60 standard stars, including a few that are blue. The standard stars lie mainly between 15th and 19th magnitude

1. Astronomy Department, University of Washington, Seattle, WA 98195

in the F555W passband. That magnitude range was chosen to ensure high signal-to-noise data, without saturation, for conveniently short exposures in all 15 passbands. With the exception of data for F336W and F1042M, the standard stars have internal errors averaging less than 0.02 mag. WFPC2 retains 14 of the original 15 calibrated WFPC1 passbands. F725LP is the only one that was dropped.

Most of these selected WFPC passbands are wider than their counterparts in other standard color systems, because the WFPC team decided early-on to seek the highest possible signal level while accepting a slight reduction in astrophysical purity. For example, F555W (the most popular WFPC filter) is 1.9 times wider than Johnson V , and F569W (the purported substitute for V) is 1.4 times wider than Johnson V . There is, however, a medium-width filter, F547M, which is only 0.8 as wide as Johnson V , and which transforms to V with almost no color-index dependence.

II. The WFPC Photometric System

As a practical matter, a photometric system should be based on only a few filters — not 14. We therefore need to consider what subset of the 14 should be chosen for a WFPC Photometric System. For many of our GTO programs, including the study of stellar populations with color-magnitude diagrams and color-color diagrams, the filters originally preferred by the WFPC1 team were F336W, F555W, and F785LP. But, because of the spherically aberrated PSF, most of the WFPC1 team's stellar population programs were postponed. In reviving those programs using WFPC2, we now recommend F814W in place of F785LP, because the infrared response of the WFPC2 chips differs somewhat from that of the WFPC1 chips. Thus, the filters of choice for stellar populations are now those shown in the following table:

Table 1: The WFPC Photometric System

	WFPC2 Passband	$\bar{\lambda}$ (nm)	$\delta\bar{\lambda}$ (nm)	$\int QI d\lambda/\lambda$ (percent)
Ultraviolet	F336W	334	38	0.33
Blue	F439W	430	47	0.47
Visual	F555W	541	124	2.50
Red	F675W	671	88	2.16
Infrared	F814W	794	153	1.96

These five passbands are WFPC analogs of $UVBRI$, but are certainly not equal to them. In some HST -WFPC programs, only F555W and F814W are being called for. In others, F336W is included. If a blue band is to be added, F439W is the only available candidate. For adding a red band, the choice of F675W may be more debatable. A popular alternative to F675W for red is F702W because of greater width and higher throughput, but F702W much more strongly overlaps F814W and is therefore more redundant with it. Another popular passband of great width and high throughput is F606W, which is being used for deep surveys.

There has been much thrashing about in reviewing the choice of F336W for the ultraviolet, because F300W (a new option available with WFPC2) will be more sensitive for the detection of hot stars. On the other hand, F300W cannot be directly tied to ground-based photometry nor be easily linked to existing color-magnitude relationships. Moreover, a theoretical color-color diagram using F300W does not appear to offer any astrophysical advantage over one using F336W. In addition, F300W may be inherently harder than F336W to calibrate accurately, because the calibration of F300W will depend on the photometry of WFPC2 frames containing only a single spectrophotometric standard star. The current majority view of the WFPC1 team is to use F300W for detecting the presence of hot stars, but to retain F336W for color-magnitude and color-color diagrams.

That may change. The ultraviolet imaging capability of WFPC2 adds another dimension to the exploration of stellar populations and star-forming regions. Passbands like F300W, F255W, and F160W may thus be candidates for incorporation into an extended WFPC Photometric System, despite calibration problems. Indeed, more than one such system may evolve.¹

III. Transformations

We have calculated transformations between the 15 calibrated WFPC passbands and the five standard Johnson-Cousins *UBVRI* passbands by plotting our ground-based WFPC-system observations (Harris et al. 1991) against Landolt's (1973, 1983) data for the same Selected Area stars. The internal consistency of repeat observations clearly indicates that part of the scatter in those plots (particularly for the ultraviolet) must be due to intrinsic differences in stellar spectra. Least-squares quadratic fits to the data yield transformation formulae that probably represent abundances near solar values, while discordant stars differ somewhat in metallicity. To help quantify the second-order terms of the transformations, we also calculated theoretical magnitudes based on Gunn-Stryker (1983) spectra. The following quadratic transformation formulae pertain to the range $0.0 < (B - V) < 1.0$ for dwarfs, and to $0.0 < (B - V) < 1.0$ for giants. The exception is the transformation for F336W, which is not valid for stars bluer than $(B - V) = 0.4$.

$$F336W = U + 0.077 (U - B) + 0.018 (U - B)^2 - 0.114$$

$$F439W = B - 0.092 (B - V) + 0.017 (B - V)^2$$

$$F547W = V - 0.009 (B - V) + 0.001 (B - V)^2$$

$$F555W = V + 0.077 (B - V) - 0.025 (B - V)^2$$

$$F569W = V - 0.087 (B - V) - 0.001 (B - V)^2$$

$$F606W = V - 0.322 (B - V) - 0.004 (B - V)^2$$

1. Users preparing *HST* observing programs should contact a WFPC2 instrument scientist at STScI for information on recommended filters and be aware of information in the Handbook and Newsletter.

$$\begin{aligned}
 F622W &= R + 0.200 (V - I) + 0.013 (V - I)^2 \\
 F675W &= R - 0.163 (V - I) + 0.023 (V - I)^2 \\
 F702W &= R - 0.153 (V - I) - 0.006 (V - I)^2 \\
 F791W &= I + 0.050 (V - I) - 0.008 (V - I)^2 \\
 F814W &= I + 0.058 (V - I) - 0.027 (V - I)^2 \\
 F725LP &= I + 0.029 (V - I) - 0.033 (V - I)^2 \\
 F785LP &= I - 0.055 (V - I) - 0.034 (V - I)^2 \\
 F850LP &= I - 0.032 (V - I) - 0.066 (V - I)^2 \\
 F1042M &= I - 0.064 (V - I) - 0.116 (V - I)^2
 \end{aligned}$$

The dependence of these transformations on the nature of the stellar population (i.e., the dependence on abundances) is theoretically predictable but has not yet been observationally checked. Existing ground-based observations of some open clusters, particularly M11, may help. M11 has roughly solar metallicity, whereas [Fe/H] is -1.5 in NGC 6752, and it ranges from about -2.2 to -0.8 in Omega Centauri (Noble et al. 1991).

A second set of transformations is needed to connect in-flight WFPC observations to the established ground-based WFPC system, and the problem is very complicated. No two CCDs are exactly alike. Spectral response may vary across the CCD surface, and flat-field errors may also be significant. Even in the absence of quantum efficiency hysteresis, the throughput of a channel may vary with time, temperature, and contamination history. For stellar photometry with WFPC1, there have been additional complications due to the spherically aberrated PSF, to its non-uniformity over the field, and to its dependence on telescope focus and collimation. These problems and the sources of error are dealt with in other papers at this Workshop.

The zero points of the magnitude scales are consequently much less well known for WFPC1 observations than for the ground-based calibration. Attempts to pin down the zero points of WFPC1 were reported by the WFPC team in Chapter 12 (Hunter et al. 1992) of the *Final Orbital/Science Verification Report* and by Holtzman et al. (1991). Efforts are continuing, as for example, by Phillips et al. (1993).

Although most sources of error will be less for WFPC2 than for WFPC1, we will still have to cope with some residual PSF variation over the field, with flat-field errors, and probably with residual secular effects. Except for differential measurements, the desired accuracy of 0.02 mag for WFPC2 photometry will not come easily.

IV. Hazards in Astrophysical Interpretation

Although transformations have to be made in order to compare *HST*-WFPC results with existing *UBVRI* data in the literature, it is a serious mistake to transform WFPC observations to *UBVRI* at the start, before performing astrophysical analysis. One potential pitfall has to do with the dependence of transformations on stellar abundance differences, which I have already mentioned. It is therefore important to

use theoretical isochrones and luminosity functions associated with the *WFPC Photometric System* itself, such as those investigated by Edvardsson and Bell (1989). However, those models need to be expanded to provide a broader choice of Z and Y , and they particularly need to include metal-rich populations.

Another potential pitfall has to do with the ratio of interstellar extinction to color excess. It is incorrect to transform WFPC observations to Johnson-Cousins *UBVRI* and use the canonical extinction ratios associated with *UBVRI* passbands. One must instead use the ratios that pertain to the passbands of observation. The importance of this extinction pitfall caught our attention in the analysis of WFPC1 observations of the Galactic bulge, where the interstellar extinction is very large and regionally variable (Baum et al. 1992, Holtzman et al. 1993). We can use passband data from the *HST WFPC2 Instrument Handbook* (Burrows et al. 1993), together with the relations given by Cardelli et al. (1989), to evaluate this effect for WFPC2 observations. We find that the extinction for F555W will be nearly 2.5 times the color excess $E(\text{F555W}-\text{F814W})$, whereas the extinction for Johnson-Cousins is only about 2.0 times the color excess $E(V - I)$.

V. Augmentation of the WFPC2 Calibration

The flat fields and standard-star calibrations that are already planned for WFPC2 will probably be adequate for much of the proposed WFPC science but could be improved for stellar population studies. Many WFPC2 programs are affected. Stellar population targets lie in star clusters, the Galactic bulge, the Magellanic Clouds, dwarf spheroidals, dwarf irregular galaxies, M31, M33, and various other nearby galaxies. The problem is that age and metallicity determinations are sensitive to having the zero-points of the magnitude scales be precisely the same as those assumed in constructing the theoretical isochrones. Consider, for example, an old metal-rich population such as one finds in the Galactic bulge, and assume exposures suitable for the turnoff region. The isochrone fit then depends to a large degree on the color indices of the turnoff and the subgiants. Using the WFPC isochrones of Edvardsson and Bell (1989), we see that an error of only 0.01 mag in the color index scale corresponds to errors on the order of 1 Gyr in age and/or 20 percent in metallicity.

The best way of improving confidence in WFPC isochrone fitting is for the calibration program to include some WFPC2 observations of a population whose age and metallicity we already have some confidence in and are willing to adopt for reference. An ideal isochrone reference target would be the exceptionally well studied globular cluster 47 Tucanae (NGC 104). A field of suitable star density in 47 Tuc would have to be selected, and approximately the following exposure times would be needed:

WFPC2 Passband	F336W	F439W	F555W	F675W	F814W
47 Tuc exp. (sec)	700	135	20	25	30

At least two such exposures should be taken in each of these passbands in order to deal with cosmic rays.

There may be alternatives to 47 Tucanae, but our calibration field in Omega Centauri cannot be used for this purpose, because of the spread in its metallicity (Noble et al. 1991).

References

- Baum, W.A., Light, R.M., Holtzman, J., Hunter, D., Kreidl, T., O'Neil, E.J.Jr., and Groth, E.J. 1993, in Galactic Bulges (IAU Symposium 153), edited by H. Dejonghe and H. Habing (Kluwer), in press
- Burrows, C.J. and many co-authors, 1993, Hubble Space Telescope Wide Field and Planetary Camera 2 Instrument Handbook, version 1.0 (STScI, Baltimore)
- Cardelli, J.A., Clayton, G.C., and Mathis, J.S. 1989, ApJ, 345, 245
- Edvardsson, B. and Bell, R.A. 1989, MNRAS, 238, 1121
- Gunn, J.E. and Stryker, L.L. 1983, ApJS, 52, 121
- Harris, H.C., Baum, W.A., Hunter, D.A., and Kreidl, T.J. 1991, AJ, 101, 677
- Harris, H.C., Hunter, D.A., Baum, W.A., and Jones, J.H. 1993, AJ, 105, 1196
- Holtzman, J.A., Groth, E.J., Light, R.M., Faber, S.M., Hunter, D., O'Neil, E.J.Jr., Shaya, E.J., Baum, W.A., Campbell, B., Code, A., Currie, D.G., Ewald, S.P., Hester, J.J., Kelsall, T., Lauer, T.R., Lynds, R., Schneider, D.P., Seidemann, P.K., and Westphal, J.A. 1991, ApJ, 369, L35
- Holtzman, J.A., Light, R.M., Baum, W.A., Worthey, G., Faber, S.M., Hunter, D.A., O'Neil, E.J.Jr., Kreidl, T.J., Groth, E.J., and Westphal, J.A. 1993, AJ, 106, 1826
- Hunter, D., Faber, S., Light, R., and Shaya, E. 1992, in WFPC Final Orbital/Science Verification Report, edited by S.M. Faber (STScI, Baltimore), Chapter 12
- Landolt, A.U. 1973, AJ, 78, 959
- Landolt, A.U. 1983, AJ, 88, 439
- Noble, R.G., Dickens, R.J., Buttress, J., Griffiths, W.K., and Penny, A.J. 1991, MNRAS, 250, 314
- Phillips, A.C., Forbes, D.A., Bershady, M.A. 1993, poster paper at this *HST* Calibration Workshop

Systematic Errors in WFPC Photometry

Robert M. Light¹

I. Introduction

The unusual character of the WFPC point spread function (PSF) leads to many peculiarities in the photometric behavior of reduced data. The most obvious effect on the PSF is that approximately 85 percent of the total light of a point source is spread into a halo that covers many hundreds of pixels. Only the central few pixels contain information at fairly high S/N levels. Beyond the problem of adding up all of the flux in a noisy picture, there are several sources of error, including a subtle by-product of spherical aberration, that can lead to systematic errors in the accuracy of photometry in WFPC frames.

II. Errors in Processed Data

One source of error in the production of photometry concerns how well the pipeline reduced the data. Currently, the dominant error introduced by WFPC data reductions are problems with the flat fields. No matter how well you measure the brightness of a source on a frame, if the flat field has variations of 10 – 30 percent, your photometry will be no better than that (see Biretta, this volume). Fortunately, with the accumulation of large numbers of deep exposures in uncrowded regions, a sky-flat can be produced for the WFC (see papers by Phillips et al.; Ratnatunga et al., this volume). Although the similar production of a PC sky flat is very unlikely, the errors in its flat fields are less horrific due to the smaller PC field of view.

The proper flat-fielding of a chip and the ability to combine photometry from different chips depends upon the accuracy of the cross-chip normalization. These normalizations, which should correct for the variation in the overall sensitivity of the chips, are affected by flat-field variations within and among the chips. Depending on how the normalizations are calculated, the effects may be as large as 5 – 10 percent; see the offsets in Figure 4. With the improved sky flats, this error should be reduced.

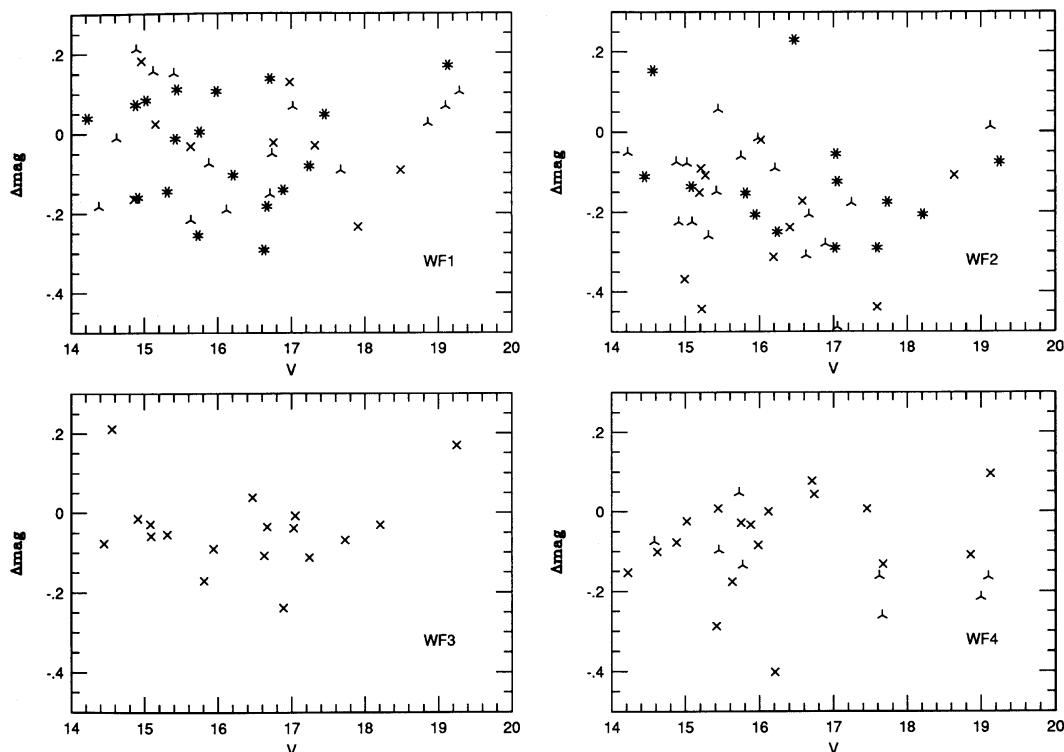
Other possible sources of photometric error, such as the A-to-D correction and flipped parity of the odd-even noise pattern in the bias (possibly in older data), are much smaller than those introduced by the flat fields. However, these may become significant, especially for extended field, low surface brightness applications, given the use of more accurate flats.

1. Caltech/IPAC, Pasadena, CA 91125

III. The PSF and Photometric Measurements

Another potential source of errors is the shape and variability of the PSF. Of course, how you produce your photometry determines how seriously you are affected by such problems. The two popular photometry methods are aperture and PSF-fit photometry. The latter is preferred for most fields observed with the *HST* because of their crowded or complex nature. However the numbers from PSF-fit techniques, which measure the flux within a small radius around the center of the source, must somehow be tied to calibrations of some standard system, which are measurements of the total count rate. The connection between them, the so-called aperture corrections, are a major source of systematic error in the calibration of WFPC PSF fluxes.

Figure 1. NGC 188 Standards



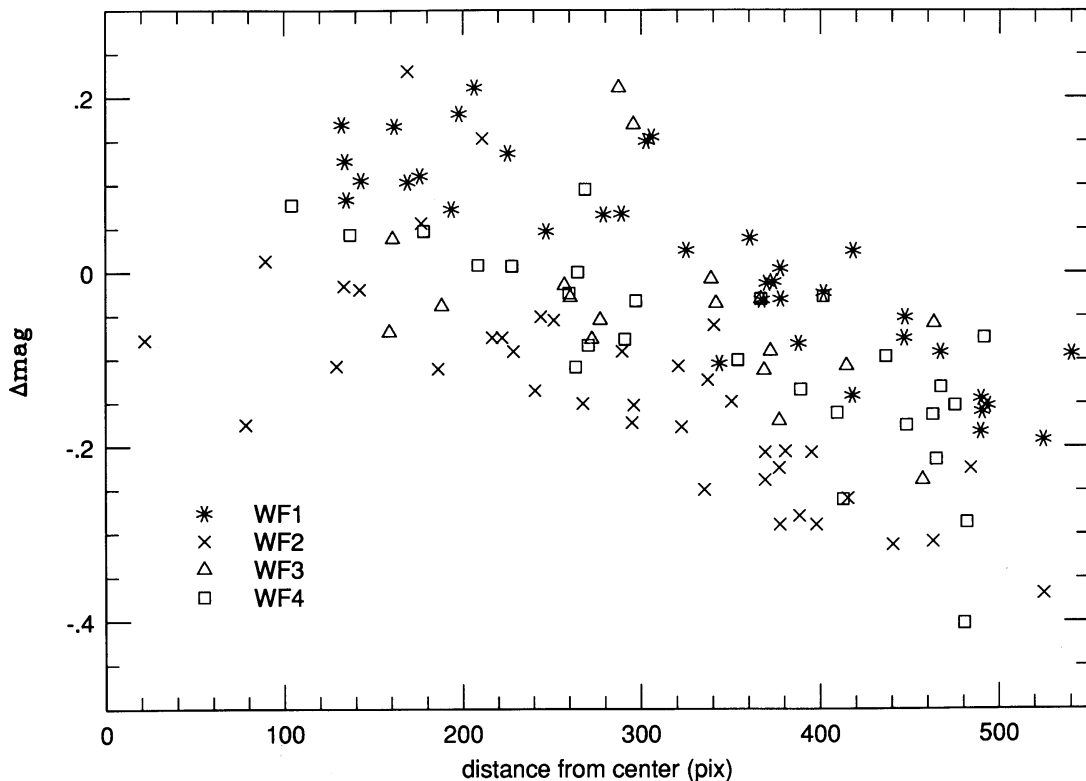
The following analysis of the WFC photometry was made using three fields in the open cluster NGC 188, taken in August 1992 and processed with the current STScI pipeline (i.e. no sky-flat correction). There are a large number of fairly isolated stars, with known magnitudes from the ground (Caputo et. al, 1990) populating most of the chips. The comparison to ground truth is vital, considering the complex nature of the aperture corrections and the flat fields.

The differences between ground photometry, converted to the WFPC F555W standard system, and raw instrumental magnitudes returned by a PSF-fit algorithm are shown in Figure 1. Each panel is a different chip, plotting the difference in magnitude versus the Caputo V measurement for the stars. The different symbols denote from which of the three pointings the data was derived; there do not seem to be any significant trends with such timing. The most striking feature of the plots is

the large dispersion in magnitude differences, much greater than the errors quoted by Caputo, and equally large in bright stars as well as faint. Some of the scatter must come from variations in the flat fields, but there are other sources of error.

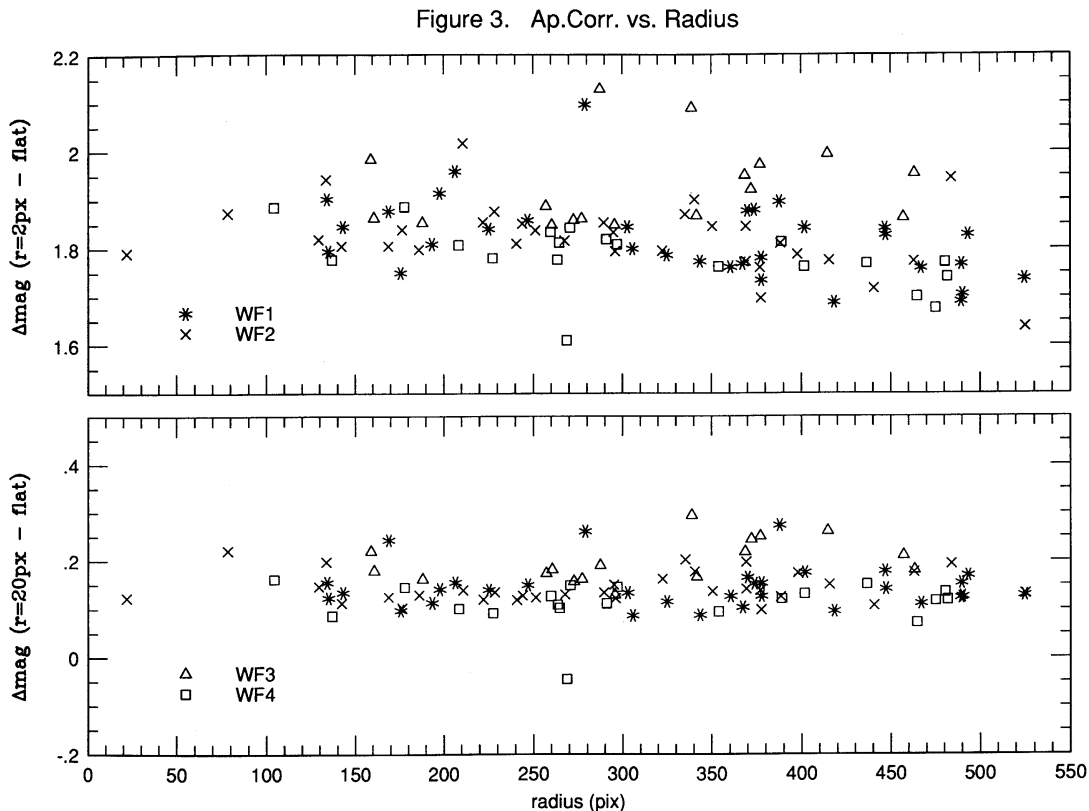
If errors arise from PSF structure and variation, they should correlate well with the distance from the center of symmetry of each chip. Figure 2 shows the same differences in magnitude plotted versus distance from the center of symmetry. Each chip is plotted as a different symbol. There is a clear correlation between delta magnitude and the distance from the centers of symmetry, in the sense that stars further from chip center are measurably brighter. The slopes of the relations, and their similarity among the chips, is highly suggestive of a PSF artifact. (The offsets in the zero points of the relations may indicate errors in the flat-field normalizations.)

Figure 2. NGC 188 radial correlation



If this is a real feature of the PSF, it should also show up in the aperture corrections. Photometry of NGC 188 stars was performed through several apertures; these numbers were compared to total magnitudes measured via curves of growth. The results for two apertures, narrow (2 pixel) and wide (20 pixel) radii, are shown in Figure 3. The correlation seen in the small aperture photometry decreases with increasing aperture width. In the widest case (20 pixels, containing over 80 percent of the total flux), there is no significant correlation. Thus the core of the star may become overly bright but the total brightness of the point source is conserved no matter where it may lie on a single chip.

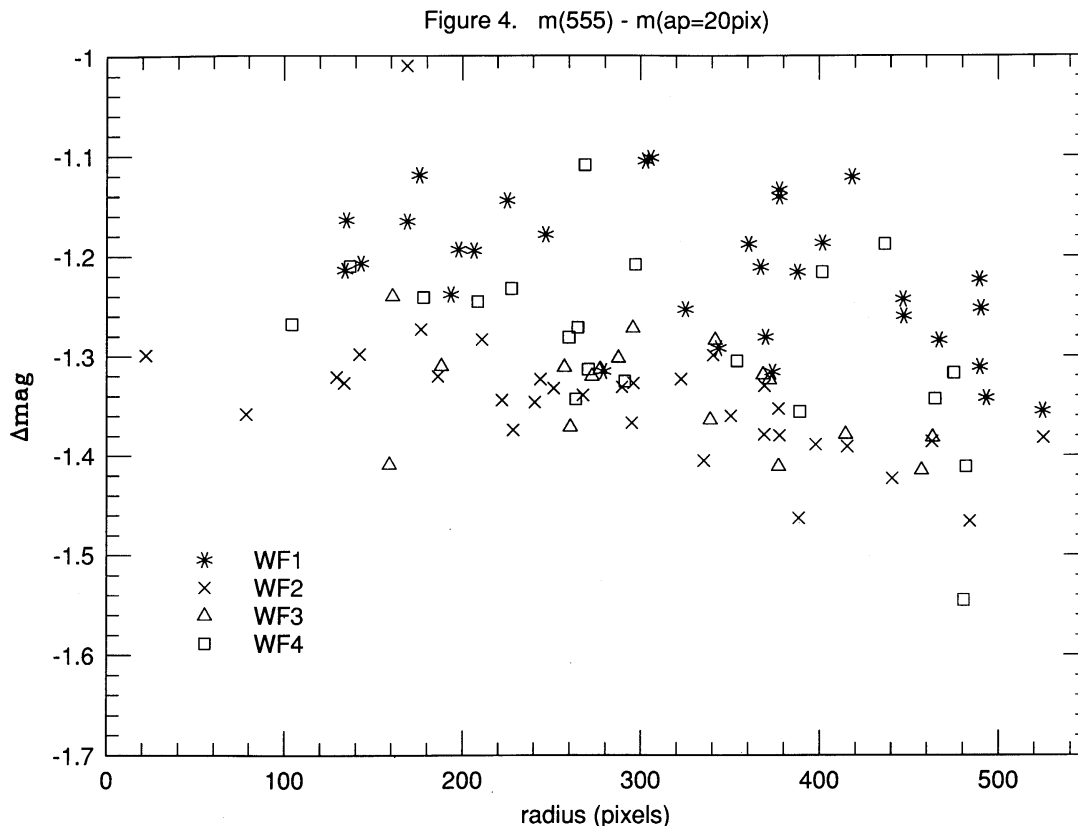
This effect has been mentioned before as the core-halo effect (see Holtzman et al., 1991, and the WFPC OV/SV Final Report). The PSF becomes vignettted towards the



edge of a chip, greatly affecting the halo of the light distribution. The core of the PSF tends to be unaffected by this removal of light, so its brightness is more constant over the field of view. However, when the flat field (an aggregate of many overlapping PSFs) is applied, the total light of the star is restored, in effect removing the effects of the vignetting. Thus the cores of stars near the edge will be over-corrected and appear too bright relative to the total magnitude of the star.

The size of the effect in small apertures is on the order of 0.1 magnitudes, perhaps greater when measurements are more strongly biased to the central pixels of a PSF, for example PSF-fitting with DAOPHOT. Obviously the assumption of a simple aperture correction applied to all photometry in a single chip will lead to large systematic errors. A simple radial fit to the aperture correction curve may help cut the error in half. However, to truly minimize this effect, an empirical mapping of aperture corrections should be applied. Given that an appropriate dataset may not exist, it may be possible to compute a suite of PSF models, for example, by using Tiny Tim, plot aperture correction curves and normalize them to some real measurements, say, the aperture corrections at the centers of symmetry in the chips.

Even with appropriate aperture corrections, there may be other problems. Figure 4 shows the difference between ground truth and the large aperture measurements in NGC 188. As mentioned in the previous section, the offsets in zero-points between chips most likely indicate problems with the cross-chip normalization. There still seems to be a slight trend with distance from the centers of symmetry. This may be due to structure in the flat fields, which is somewhat (but not strongly) radially dependent, or perhaps to the flat fields imperfectly correcting for vignetting because of their different illumination pattern. If so, a sky flat would also help this problem.



IV. Contamination and Overall Calibration

A major concern to calibration, especially in the blue bandpasses, is the presence of contamination. The presence of a volatile substance on the front window of the CCD has two significant effects: 1) the diffraction of light about small enhancements (pockets) of contaminants (measles), and 2) the attenuation of incident flux, especially to the blue. The pockmarks known as measles are especially problematic if they land near the center of an object with a point-source-like light distribution. The scale of a measles is not much different from the core of a PSF, and thus will significantly perturb any attempt to fit a PSF. Such a problem may affect photometry by 5 – 10 percent or more.

The effect of the attenuation of flux is well-studied and discussed in detail in several STScI WFPC reports and in this volume. An important implication of the loss of flux is how rapidly it may affect photometry. The following table gives estimates of the time it will take for contamination buildup to result in a 10 percent loss of flux.

Filter	F194W	F230W	F336W	F439W	F555W	F785LP
Time	(hours)	(1-3 days)	30d	80d	140d	400d

These numbers are indicative of the general trends seen in the WF2 and PC6 chips; they may not be representative of the initial falloff after a decontamination or of variations between chips. There may be slight variations in the contaminants left of different chips, after different decontaminations. However, given the limited

information in the monitor (centers of WF2 and PC6), a significant effect is not seen.

The successful calibration of WFPC photometry depends on the proper application of several corrections. Many of the problems in understanding the state of the WFPC instrument response and the PSF have become better understood after the accumulation of data (deep exposures for flat fields, contamination monitor, etc.) and intensive modeling. However our understanding of all effects on photometry is almost certainly incomplete, and residuals of a few hundredths of a magnitude in this or that correction may conspire to limit the overall photometric accuracy to worse than 0.05 magnitudes.

References

- Caputo, F., Chieffi, A., Castellani, V., Collados, M., Martinez Roger, C., and Paez, E., 1990, *A.J.*, 99, 261.
Holtzman, J. A., et al, 1991, *ApJ Letters*, 369, L35.

Reduction of WFC Images with DAOPHOT III

Peter B. Stetson¹

Abstract

New additions to the DAOPHOT family of stellar-photometry software are described, and results of their application to WFC imagery are presented.

I. Introduction

For almost exactly ten years, I have devoted a major fraction of my professional efforts to the development of software for extracting stellar photometry from digital images. The agglomeration of code that has resulted may be referred to by the generic name DAOPHOT, but that term includes a number of generations and a myriad of modifications. DAOPHOT Classic (Stetson 1987) was the first photometry package—as far as I know—to incorporate the concept of the hybrid point-spread function (PSF): the model PSF of an image is first approximated by a continuous analytic Gaussian function, and the brightness residuals from that fit are stored as a look-up table of corrections from the analytic first approximation to the true model PSF. When the brightness value for a given pixel at a particular point in the stellar profile is to be predicted, the analytic first approximation is numerically integrated over the area of that pixel, and then a correction to the true PSF is obtained by interpolation within the look-up table. The hybrid PSF succeeds because the look-up table provides the flexibility to cope with asymmetric or irregular PSFs, while the analytic first approximation, representing most of the flux in the profile, provides the high-order spatial derivatives needed for accurate interpolation in critically sampled or slightly undersampled grids. PSFs which varied with position in the digital image were soon encountered; this was dealt with by replacing the one look-up table of corrections from analytic to true PSF with three tables, which allowed the empirical correction at each point in the profile to be represented by a first-order Taylor expansion as a function of position in the frame.

As we moved into the *HST* era, it became necessary to deal with even more severely undersampled and spatially complex PSFs than we had seen before. DAOPHOT II: The Next Generation (Stetson, Davis, & Crabtree 1990) was written before we learned of the spherical aberration in *HST*, but it has fortuitously turned out to be comparatively effective in dealing with the aberrated PSF as well (Stetson 1991, 1992). DAOPHOT II: TNG allows the user a choice of analytic first approximations — a Gaussian function (as before), two different Moffat functions, a Lorentz function (this is the best for *HST*), and the sum of a Gaussian function with a Lorentz function

1. Dominion Astrophysical Observatory, Herzberg Institute of Astrophysics, National Research Council of Canada, 5071 West Saanich Road, Victoria, British Columbia V8X 4M6

(this is seldom used). In addition, six look-up tables of corrections allow for a PSF which varies as a quadratic function of position in the frame. Various other differences in detail, most notably in how the average PSF is estimated from a large number of stars at various positions and magnitudes in the science frame, were incorporated at about the same time. For instance, I made it possible to include centrally saturated stars in the PSF; the saturated pixels near the peak of the profile are ignored, but the unsaturated outskirts can improve the signal-to-noise ratio in the extended wings of the model PSF.

II. DAOPHOT III: This Time It's Personal

More recently, I have undertaken some further refinements of the DAOPHOT approach to stellar photometry; these have been found helpful in reducing images obtained with the aberrated *HST*, and I would like to describe them here.

First and most trivially, the maximum number of look-up tables containing the Taylor expansion of the corrections from the analytic first approximation of the PSF to the true PSF has been increased from 6 to 10, to allow encoding the stellar profile as a cubically varying function of position.

Second, in developing the empirical PSFs to be used in the reduction of the images of M81 obtained for the *HST* Extragalactic Distance Scale Key Project (Freedman, et al. 1994; Hughes, et al. 1994), I found that there were not enough bright, unsaturated, isolated stars in any one field to define a good empirical PSF. In a first crude attempt to deal with the problem, I summed median-averaged images of the M81 major-axis fields observed with chips WF1 and WF2, to produce a single image with twice the surface density of bright-ish stars. From this image I derived a single quadratically varying PSF which was then used in the reduction of the images obtained with all four detectors. In my second attempt, for each of the four WFC chips I summed the median-averaged image of the M81 major-axis field with the averaged-image of the so-called V30 field on a chip-by-chip basis. These summed images permitted me to estimate a separate quadratically varying model PSF for each of the four chips.

This approach has some advantages and some drawbacks. The first advantage is obvious: it doubles the number of stars that can go into the definition of each PSF. Since the image of each field is itself an average of individual exposures obtained at different epochs, the derived PSF is appropriate for some sort of average of the various focus settings and jitter histories of the individual exposures. It is not clear whether this is an advantage or disadvantage. (I can say, however, that in my experience, the changes in the PSF due to the breathing of the telescope and the tracking wander during the integration are not dominant sources of photometric error, when compared to other obvious problems of *HST* photometry.) The averaging of the various images of each field reduces the effect of readout and Poisson noise, but the unavoidable subpixel offsets of the various exposures does broaden the core of the resulting PSF. And at the same time as the summing of two different fields doubles the number of available PSF stars, it also doubles the degree of crowding they are subject to.

I have attempted to deal with the drawbacks while retaining the advantages of determining the model PSF from a multiplicity of images, by creating a new stand-alone module which I have named MULTIPSF. MULTIPSF is merely the old PSF routine from within DAOPHOT, with the addition of a third dimension. While the PSF routine derived a model point-spread function from stellar images recorded in a two-dimensional digital image, MULTIPSF derives a single model PSF from stellar images recorded in a stack of two-dimensional images. As was always the case with DAOPHOT, a provisional model PSF is used to fit the stars in each image, and then the neighbor stars are subtracted from each image leaving selected bright stars more or less isolated in their frames, for the derivation of an improved model PSF. If the spacecraft has been moved between exposures, or if entirely different fields have been imaged, the various frames will contain stars sampling the PSF in different portions of the focal plane. The spatial variation of the PSF will therefore be better constrained than it could have been by any one of the input images. Nevertheless, the stars used to define the PSF are not more crowded than before, because the model is derived from the individual images in the stack, rather than from their sum. Readout and Poisson noise are still beaten down by the inclusion of numerous stars in a multitude of frames in the model PSF, but the core radius of the derived PSF is not spuriously broadened, again because the individual exposures are employed, not their average.

The third and largest component of DAOPHOT III is a program which I call ALLFRAME. As described in Stetson (1994), ALLFRAME is the culmination of a sequence of increasingly sophisticated model-profile fitting packages consisting of the DAOPHOT routines PEAK and NSTAR, and the stand-alone programs ALLSTAR and ALLFRAME. PEAK performs fits of the model PSF to stars contained in a digital image one star at a time. NSTAR performs simultaneous profile fits to small groups (≤ 60 stars) of mutually blended star images. ALLSTAR extends the scope of NSTAR to the simultaneous derivation of photometric parameters for all stars contained in a given digital image. ALLFRAME carries this process to the logical limit: it performs simultaneous profile fits for all stars contained in *all* the images of a given patch of sky. In doing so it maintains a single, self-consistent list of program objects and of their positions, and solves for an independent magnitude for each star at each epoch. At present, ALLFRAME also determines an independent value for the sky brightness underlying each target, but it is conceivable that in the future the sky-brightness models for the different frames could be coupled in some way.

ALLFRAME offers several distinct advantages for stellar photometry:

- It maintains a consistent star list for all frames. When different exposures of a given field are reduced independently, and their photometric results are then combined *ex post facto*, it often happens that a blob of light is reduced as a single star in some frames and as a blended double in others. When the results are combined, the single star is identified with one component of the double in the other, and the result is a spurious variable star (if the frames are in the same filter) or a ludicrous color (if the frames are in different filters). With ALLFRAME, a blended double is always a blended double, always with the same position angle and separation.
- It uses all available data for all stars. PEAK, NSTAR, and ALLSTAR are

instructed to discard any detection which is significant at less than a three-sigma level. They must do this to prevent individual bright stars from being reduced as tight clusters of stars of dubious reality, and to prevent the diffuse sky brightness from being represented by millions of faint stellar profiles, one for each noise peak in the background. This has the obvious consequence that if a star appears as a 3.1σ detection in one frame and a 2.9σ detection in the next, it is retained in the former and discarded in the latter. The final average magnitude for the star is based on only half the data—predominantly the overestimated half. ALLFRAME retains every object that is a three-sigma detection in the combined data for all frames, and uses all data for that object from every frame in which it lies.

- ALLFRAME has fewer degrees of freedom. Rather than deriving an independent position for each star in each frame, it solves for a single position per star, and transforms that to the coordinate system of each frame. This results in higher photometric precision, especially in crowded fields.
- ALLFRAME does a better job of recognizing and then disregarding blemishes and cosmic rays. A defect in the wings of a stellar image would normally influence the determination of the star's centroid. By requiring the centroid of the blemished profile to be consistent with that star's position in all of the other frames in which it appears, the contamination is made more apparent and can be ignored.

III. Test 1: IC 4182

Besides the aforementioned work on the M81 data for the Key Project, I have analyzed two public-domain datasets from WFC. The first of these, the IC 4182 data from program 2547, *Calibration of Supernovae of Type I as Standard Candles* (A. Sandage, PI), is an example of a comparatively simple problem in relative *HST* photometry: the telescope pointing and roll angle were virtually identical (to within about four pixels, peak-to-peak) at all epochs. This means that systematic errors in the model PSF and in the flat-field corrections will cancel out (I used data that had been subjected only to the pipeline calibration procedures): apparent epoch-to-epoch variations in stellar magnitude should be real, or should reflect the response of the reduction software to the inherent precision of the data.

The data set consisted of 19.5 cosmic-ray splits in the F555W filter, and two C-R splits in F785LP, totalling 43 separate exposures with each of the four WFC chips. All exposures were in the range of 1900-2100 sec, and in the four subfields I determined magnitudes for a total of some 48,000 stellar objects. The total number of individual stellar models actually fit was 1,790,780. The root-mean-square repeatability of the individual stellar magnitudes for stars measured in at least 19 of the 39 F555W-band images (after the removal of a single zero-point constant for each frame intended to allow for the epoch-to-epoch sensitivity variations in the camera) is approximately 0.03–0.05 mag from the magnitude level at which saturation sets in to a level roughly three magnitudes fainter. Below that, the standard deviation increases as an exponential function of apparent magnitude, passing through 0.3 mag maybe five magnitudes below saturation.

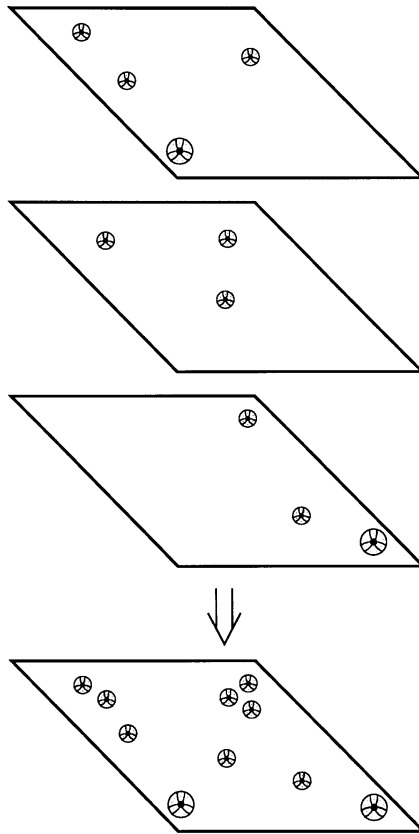


Figure 1: MEDPIC

However, it must be remembered that in 39 exposures of order 2000 seconds apiece, most of the stars in the field will have been involved in a cosmic-ray event at least once. The root-mean-square estimator of the photometric repeatability will be greatly inflated by the inclusion of the spurious magnitude estimates obtained from these contaminated images. A careful astronomer with a lot of time to spare would sort through the results and identify and eliminate those measurements that are obviously and hopelessly incorrect, and would derive the mean magnitudes and the estimates of precision from only those observations that seem to be valid. For my present purposes, I will estimate the photometric precision of my results using a statistic that is more robust against the presence of extreme outliers, and is more sensitive to the spread in the residuals of more typical observations: 1.2533 times the mean absolute residual. If the error distribution were truly Gaussian, this would have the same expectation value as the root-mean-square statistic, but since each the first power of each residual is used rather than the square, the rare extreme outliers have much less influence on the result.

When this more robust estimator of precision is used, the magnitude level at which a particular photometric repeatability is achieved is at least a magnitude fainter than when the root-mean-square residual is employed. The frame-to-frame repeatability is in the range 0.03–0.05 mag to about five magnitudes below the saturation level,

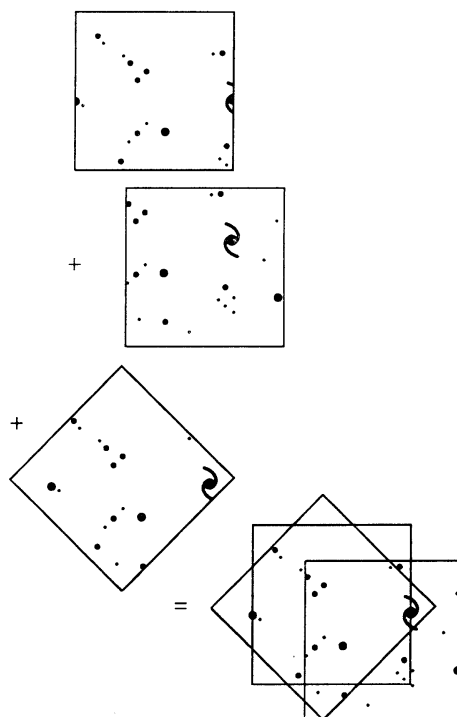


Figure 2: ALLFRAME

and the data are repeatable to ± 0.3 mag more than six magnitudes below saturation.

The use of ALLFRAME also permits the measurement of stars nearly two magnitudes fainter than the older one-frame-at-a-time packages. ALLSTAR retains only those stars that are three-sigma or greater detections in each input frame; as just mentioned, using the robust estimator this precision is achieved roughly 6.5 magnitudes below saturation in the F555W images of IC 4182. ALLFRAME is able to retain stars that have lower precisions in individual frames, provided that they are significant to of order 3σ in the aggregate of all frames. Adding the additional criterion that stars must have been recoverable in at least 19 of the 39 F555W exposures, I find that the star list extends to somewhat more than eight magnitudes below the saturation level. Stars at the detection limit are precise only to ± 0.8 mag per frame, but by the time 19–39 independent magnitude determinations have been averaged, the standard error of the mean magnitude at the detection limit is ~ 0.2 mag.

IV. Test 2: NGC 1850

A large number of frames of the Large Magellanic Cloud cluster NGC 1850 were obtained during the course of programs 3008, *WFPC SAT Observation: Young Cluster Photometry*, (J. Westphal, PI); 3367, *WFPC Astrometric Calibration, Plate Distortion, Pointing Assistance Calibration*, (R. Gilmozzi, PI); and 4161, *Mapping the Position Dependence of the WFPC PSF — Verification*, (R. Gilmozzi, PI). These observations provide a far more stringent test of photometric precision with *HST* and whatever

software package you may be using, because they were taken with a wide variety of center positions and roll angles — any given star can occur at different places on different chips at the various epochs. This will test the quality of both the flat-fielding (again, I reduced pipeline-calibrated data) and the model PSF. Unfortunately, at the present time I have no way to evaluate the relative importance of these two sources of systematic error, but future analyses based on new flat fields and utilizing comparisons with ground-based results may eventually resolve the ambiguities.

The data set for NGC 1850 includes 17 individual exposures in the F555W filter, with exposure times ranging from 10 sec to 1100 sec; 10 exposures in F785LP, again from 10 sec to 1100 sec; and two 1100 second exposures in F439W. Of course, each exposure consists of actual data frames from each of the four WFC detectors. Final photometric data were extracted for a total of 16,441 stars in the NGC 1850 field appearing in at least two of the 116 individual frames; 353,598 individual model profiles were actually fit.

The robust error estimates for the NGC 1850 results were considerably poorer than for IC 4182: at no magnitude level was the frame-to-frame repeatability consistently better than 0.10 mag. Since the exposure times ranged over more than two orders of magnitude, it is not possible to reference the precision to any particular saturation magnitude. Nevertheless, in the global combination of results the limiting precision of 0.10 mag was obtained over about a four-magnitude range. Since for each star this figure includes results from 10 second frames where everything is faint to 1100 second frames where many stars are saturated, a better figure of photometric merit might be derived from frames with a single exposure time. The data set for NGC 1850 includes seven 300 second exposures, each one taken with a different pointing of the telescope. If I then take the photometric results for each star that appeared in at least 4 (so that the sigmas will be reasonably well-defined) and not more than 7 (to eliminate stars split between frames by the edges of the pyramid mirror) of the 300 second exposures, and compute their photometric scatter with respect to the mean of all available data, the precision is still no better than 0.10 mag at any magnitude level. However, this level of precision is achieved over about a five-magnitude range, from about one magnitude above saturation to four magnitudes fainter than saturation. Fainter than this, the photometric error grows exponentially with magnitude, passing through ± 0.3 mag some six magnitudes below the saturation level. Again, at this point I have no way of knowing whether the errors are dominated by the flat fields or by the model PSF, but I suspect the former.

Acknowledgments

I am grateful to the goofy bunch of guys at the Canadian Astronomy Data Centre, located at the Dominion Astrophysical Observatory in Victoria, for their assistance in acquiring some of these public-domain data; and to Jeremy R. Mould, lately of Caltech, for his moral and financial support in carrying out this work.

References

- Freedman, W. L., Hughes, S. M., Madore, B. F., Mould, J. R., Lee, M. G., Stetson, P. B., Kennicutt, R. C., Turner, A., Ferrarese, L., Ford, H., Graham, J. A., Hill, R., Hoessel, J. G., Huchra, J., & Illingworth, G. D. 1994, to appear in ApJ
- Hughes, S. M. G., Stetson, P. B., Turner, A., Kennicutt, R. C., Jr., Hill, R., Lee, M. G., Freedman, W. L., Mould, J. R., Madore, B. F., Ferrarese, L., Ford, H. C., Graham, J. A., Hoessel, J. G., & Illingworth, G. D. 1994, submitted to ApJ
- Stetson, P. B. 1987, PASP, 99, 191
- Stetson, P. B. 1991, in Third ESO/ST-ECF Data Analysis Workshop, eds. P. J. Grosbøl & R. H. Warmels (Garching: ESO), 187
- Stetson, P. B. 1992, in Astronomical Data Analysis Software and Systems I, eds. D. M. Worrall, C. Biemesderfer, & J. Barnes, PASP Conf. Ser. 25, 297
- Stetson, P. B. 1994, submitted to PASP
- Stetson, P. B., Davis, L. E., & Crabtree, D. R. 1990, in CCDs in Astronomy, ed. G. H. Jacoby, PASP Conf. Ser. 8, 289

Ground-Based Calibration of WFC ALLFRAME Stellar Photometry in M81

Shaun M. G. Hughes¹, Peter B. Stetson², Anne Turner³, Robert C. Kennicutt Jnr³
Robert Hill⁴, Myung Gyoon Lee⁵, Wendy L. Freedman⁴, Jeremy R. Mould¹
Barry F. Madore¹, Laura Ferrarese⁶, Holland C. Ford⁶, John A. Graham⁷
John G. Hoessel⁸ and Garth D. Illingworth⁹

Abstract

The Distance Scale Key Project for the Hubble Space Telescope, which aims to obtain reliable Cepheid distances to a set of galaxies that will be used to calibrate a variety of secondary distance indicators, relies on an accurate calibration of Cepheid magnitudes. The first and nearest of these galaxies is M81, which was observed for 22 epochs with the current aberrated Wide Field Camera, over 1991 to 1992. The ALLFRAME program (based on DAOPHOT-II) was used to obtain the *HST* magnitudes from which 30 Cepheids were identified (Freedman et al 1994). Their mean magnitudes were then calibrated to standard magnitudes via ground-based observations, obtained with the *CFHT* and Palomar 200-inch telescopes (Hughes et al 1994). This was done by establishing secondary standards in each of the WFC fields, in Johnson *V* and Cousins *I*, allowing a direct transformation from ALLFRAME magnitudes to calibrated *V* and F785LP magnitudes, giving mean *V* ~ 23 magnitudes accurate to $\sim \pm 0.1$ mag. The stellar populations in M81 have been analyzed in terms of the luminosity functions and color magnitude diagrams (CMD) derived from these data, from which we identify numerous supergiants, and a CMD morphology similar to M33.

I. ALLFRAME WFC Photometry

The two WFC fields included V30, a known Cepheid (Sandage, personal communication), and the major axis of M81. The Cepheids were identified from 22 F555W epochs. A mean reddening (Freedman et al, 1992) was determined from 6 F785LP epochs. All WFC exposures were acquired during *HST* Cycles 1 and 2, and passed through STScI's calibration pipeline (Lauer 1989; and this volume).

-
1. Caltech, Pasadena, CA 91125
 2. DAO, Victoria, BC, VX8 4M6 Canada
 3. University of Arizona, Tuscon, AZ 85721
 4. Carnegie Observatories, Pasadena, CA 91101-1292
 5. Seoul National Observatory, 151-742 Seoul, Korea
 6. Johns Hopkins University, Baltimore, MD 21218
 7. Carnegie Institute of Washington, Washington, DC 20015
 8. University of Wisconsin, Madison, Madison, WI 53706
 9. University of California, Santa Cruz, 95064

The photometry was derived from DAOPHOT II (Stetson 1992) and ALLFRAME Stetson (1994, this volume), which takes advantage of the multi-epoch nature of the photometry. ALLFRAME successively fits a point-spread function (PSF) model (with residuals which vary quadratically as a function of chip coordinates) to a list of stars for each epoch WFC frame, and any pixels that deviate from the mean are down-weighted, thereby minimizing the effects of bad pixels and cosmic rays (Stetson 1987).

For the major axis field, one PSF was used for each filter, determined from median images. For the V30 field, the PSFs were modelled on a grid of artificial stars produced by Tiny Tim (J. Krist, STScI) for each chip and filter. Tiny Tim was also used to search for variations in the PSF from epoch to epoch (due to slight changes in focus), but the differences were found to be marginal, so only one grid of stars was produced for each chip and filter, at a mean epoch (1992 Jan 20).

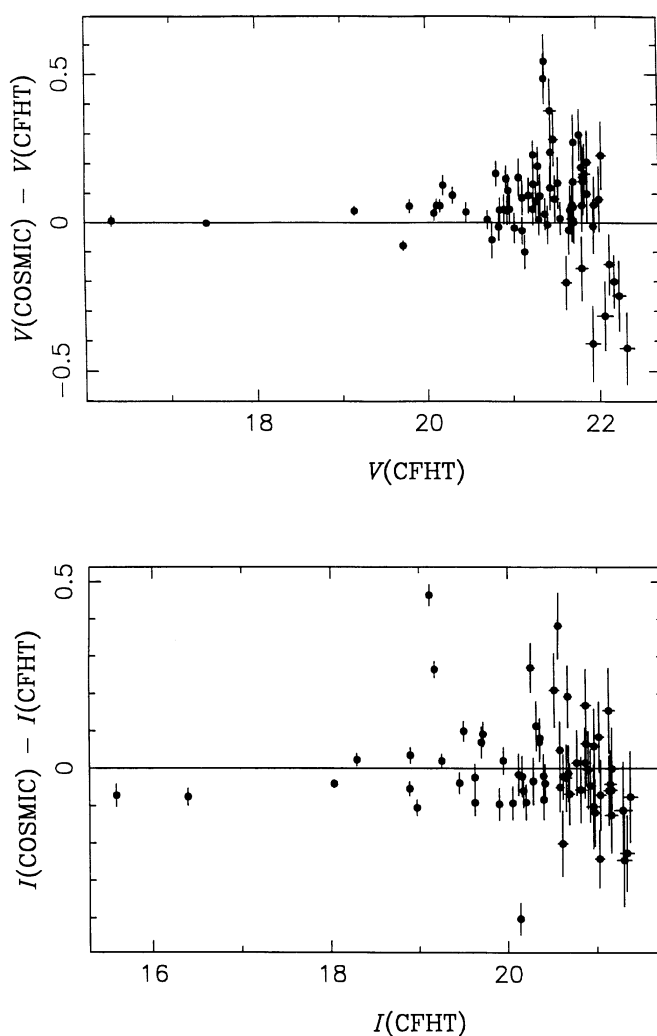


Figure 1: The difference in V and I magnitudes derived from independent exposures, for stars in the overlap region between the Palomar 5m (COSMIC) V30 field taken on 1992 June 8, and the $CFHT$ field taken on 1988 Jan 20.

Table 1: Calibration of WFC Photometry

Chip	N	$V - F555W_{ALF}$	$F785LP - F785LP_{ALF}$
—V30 field—			
1	8	3.40 ± 0.03	2.38 ± 0.17
2	11	3.62 ± 0.05	2.69 ± 0.12
3	15	3.64 ± 0.03	2.73 ± 0.04
4	15	3.51 ± 0.04	2.81 ± 0.05
—Major axis field (June 8)—			
1	6	3.39 ± 0.03	2.76 ± 0.22
2	3	3.57 ± 0.07	2.74 ± 0.18
3	2	3.50 ± 0.10	2.42 ± 0.33
4	5	3.50 ± 0.08	2.64 ± 0.09
—Major axis field (June 9)—			
1	6	3.51 ± 0.07	2.80 ± 0.14
2	3	3.63 ± 0.14	2.84 ± 0.15
3	2	3.61 ± 0.14	2.53 ± 0.35
4	5	3.64 ± 0.05	2.80 ± 0.07

Table 2: Calibration of Mean WFC Photometry

Chip	N	$V - F555W_{ALF}$		$F785LP - F785LP_{ALF}$	
		Ground-based	FW92	Ground-based	FW92
1	18	3.44 ± 0.03	(3.51)	2.61 ± 0.11	(2.70)
2	17	3.61 ± 0.04	(3.68)	2.73 ± 0.08	(2.73)
3	19	3.62 ± 0.03	(3.66)	2.69 ± 0.05	(2.59)
4	25	3.53 ± 0.04	(3.57)	2.78 ± 0.04	(2.61)

II. Calibration of WFC Photometry

Calibration of WFC photometry onto a standard system is by no means straightforward, as spherical aberration causes variations in the shape of the PSF across each chip (Faber & Westphal 1992, hereafter FW92). Also, none of the WFC flatfields are entirely flat (Phillips et al 1993), and there exists a time variation of detector sensitivity due to contamination of up to 0.15 mag in F555W (Ritchie & MacKenty 1993). To account for these effects, we established a set of 65 secondary standards in the two M81 fields, obtained from ground-based photometry of the brighter stars. V and I photometry from the *CFHT* of half the V30 field was verified

to ± 0.02 mag by independent observations on the Palomar 1.5m and the KPNO 4m. The Palomar 5m COSMIC camera was used to image both fields on 1991 June 8 and the major axis field on June 9. Although not perfectly photometric, the accuracy of the V and Gunn I photometry can be gauged by the scatter in the overlap region with the $CFHT$ exposures, see Figure 1. The mean COSMIC- $CFHT$ photometry for the 8 secondary standards in common was $+0.05 \pm 0.03$ mag in V , and -0.01 ± 0.03 mag in I . The color term in converting F555W to V is minimal (~ 0.02 mag) over the color range of the Cepheids (0.60 to 1.65 in F555W-F785LP), but as F785LP to I is large (~ 0.14 mag), we converted the secondary standards' I to F785LP (Harris et al 1991).

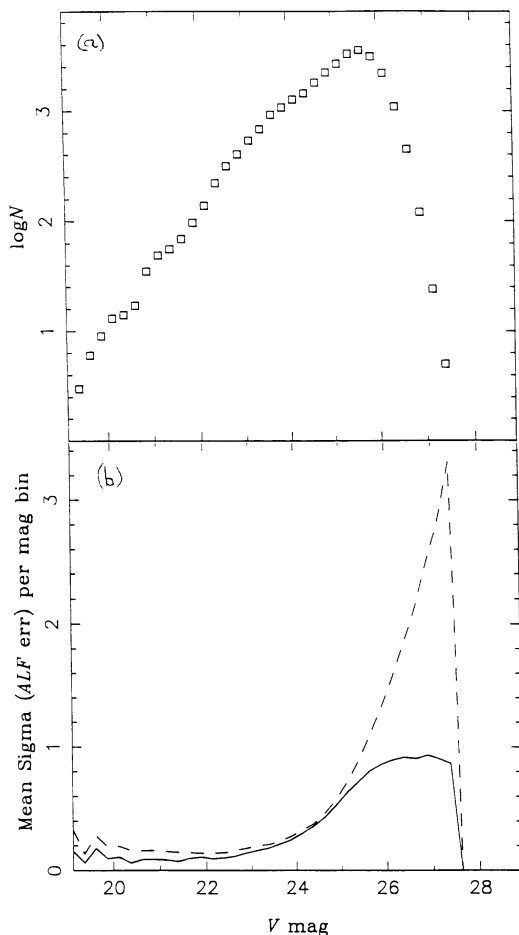


Figure 2: (a) Calibrated V luminosity function of stars that were recovered in all 22 F555W epochs in all chips and in both M81 fields, and which had rms dispersions about their mean of less than 3 standard deviations (as these are likely to have been severely contaminated by cosmic ray hits). (b) The solid line is the mean rms dispersion about the mean of the 22 epoch magnitudes of the stars in (a), for each of 50 magnitude bins. The dashed line is the mean single-epoch uncertainty given by ALLFRAME in the same magnitude bins. The uncertainties in the calibration from the secondary standards are included.

We tried various methods to account for the differences in zero points between the photometric sets (COSMIC and $CFHT$ for V30, and two nights of COSMIC for the major axis) seen in Table 1, by correcting for the differences between the empirical and Tiny Tim PSFs, and fitting surfaces to the flat field corrections (Phillips et al

1993), but none systematically reduced the field-to-field differences. Therefore, we combined the three sets, to give a mean offset between the standard and ALLFRAME photometry given in Table 2, which are comparable to what we can derive from FW92 (the figures in parentheses).

III. Stellar Populations

When the $V-F555W_{ALF}$ corrections in Table 2 are applied to the ALLFRAME photometry, we derive the luminosity function (LF) in Figure 2a. The recovery rate of simulated stars showed the completeness limit of the M81 WFC fields to be $V=25$ mag, corresponding to the position of the LF turnover. The uncertainties in these magnitudes are shown in Figure 2b, which plots the mean rms dispersion and mean ALLFRAME uncertainties from the 22 F555W epochs. Close agreement is seen down to $V \leq 25$, beyond which the ALLFRAME uncertainties and rms dispersions start to lose meaning, as they are for magnitudes clearly beyond the limit of WFC. The slope of the LF of blue stars ($V-I < 0.24$ mag) is $\sim 0.57 \text{ mag}^{-1}$, similar to other nearby late-type galaxies (Freedman 1985).

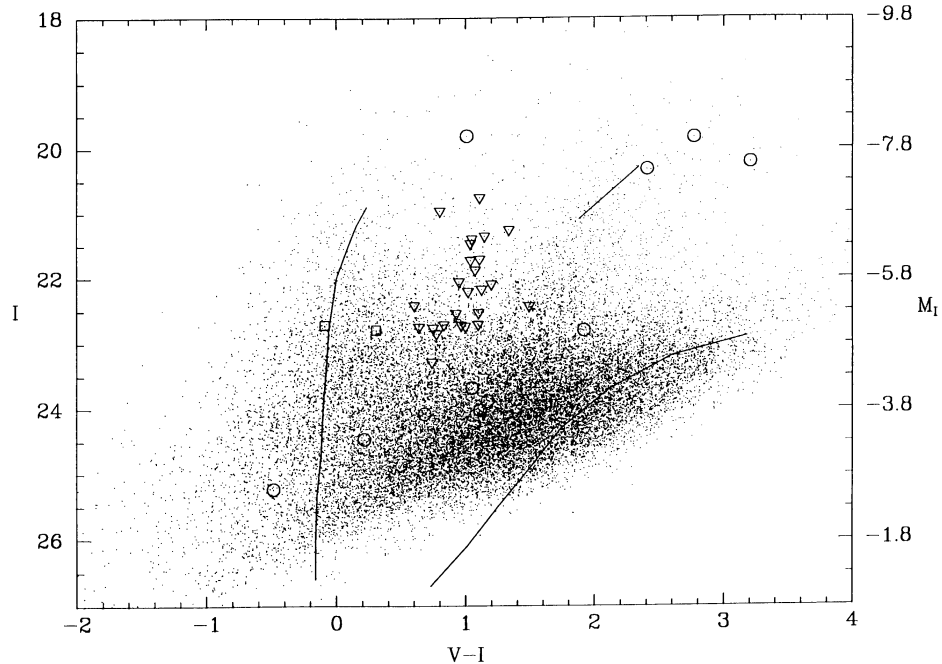


Figure 3: I vs. $V-I$ color magnitude diagram for all 26,082 stars detected in V and I in M81. Lines represent main sequence, red giant and red supergiant loci from Shapley III in the LMC (Reid et al 1987). Open triangles are Cepheids (see Freedman et al 1994). Open squares are eclipsing variables, and open circles are long-period variable candidates. The absolute magnitude scale is shown on the right, based on a distance modulus of 27.80 mag to M81.

Features in the combined CMD for both fields (Figure 3) are aligned with loci derived from the upper main sequence, red supergiants, and red disk giants of Shapley Constellation III in the LMC (Reid, Mould & Thompson 1987). The CMDs of the M81 fields are also very similar to that measured for the disk of M33 (Wilson, Freedman, & Madore 1990). This similarity is not surprising, as the three galaxies contain an

abundance of HII regions and young star forming regions, which dominate the CMD in this luminosity range.

As expected, the Cepheids (triangles) occupy the instability strip in the CMD. Two eclipsing binaries (squares) are located in the blue plume. Four long-period variable (LPV) candidates (circles) with $V-I > 1.5$ mag are likely red supergiant LPVs. To measure their periods (100 to 900 days), further (red) exposures of these fields are being taken in *HST* cycles 3 and 4 to extend the baseline. The blue faint LPV candidates may be R CrB variables, and the one bright LPV candidate with $V-I \sim 1.0$ mag may be a long period Cepheid. Although giants are probably detected (especially in our stacked images), they lie too close to the magnitude limit of our data to be reliably measured.

Conclusions

The mean V magnitudes of the 30 Cepheids found in M81 ranged from 21.6 to 23.8 (and their periods ranged from 10 to 55 days), corresponding to single epoch magnitude uncertainties (Figure 2b) of 0.1 to 0.3 mag, respectively. The uncertainties in the mean V magnitudes should therefore be in the range 0.02 to 0.06 mag (but will depend on their position and environment, and how well their light curve is sampled). But the aim is to get a distance for M81, and the accuracy in the zero point of a line of best fit to the $P-L$ relation of all 30 Cepheids is 0.06 mag, but the uncertainties due to reddening, ALLFRAME photometry, calibration, and Cepheid metallicity give a total error of 0.2 mag, equivalent to a total error of 10 percent in the distance to M81.

The bright stellar populations observed in M81 are similar to those in M33 and the star formation regions of the LMC.

References

- Faber, S. & Westphal 1992 WFPC SV Report (FW92)
Freedman W. L. 1985, ApJ, 299, 74
Freedman W.L., et al 1992, ApJ, 396, 80
Freedman W.L. et al 1994, ApJ, in press.
Harris H.C., Baum W.A., Hunter D.A., Kreidl T.J. 1991, AJ, 101, 677
Hughes S.M.G. et al 1994, ApJ, in press.
Lauer T.R. 1989, PASP, 101, 445
Phillips D. et al 1993, submitted to AJ
Reid N., Mould J., & Thompson I. 1987, ApJ, 323, 433
Ritchie C.E., & MacKenty J.W. 1993, *WFPC Instrument Science Report 93-02*, STScI.
Stetson P.B. 1987, PASP, 99, 101
Stetson P.B. 1992, in *3rd ESO/ST-ECF Data Analysis Workshop*, ESO Conference and Workshop proceedings No.38, eds. P.J.Grosbol and R.H.Warmels, p187.
Wilson, C. D., Freedman, W. L., and Madore, B. F., 1990, AJ, 99, 149

Core PSF Photometry from Wide Field Camera Images

Lukas Labhardt¹

I. Introduction

This contribution reports on the reduction and photometric calibration of WFC images taken during *HST* observing Cycles 2 and 3. The program (PI: A. Sandage) consists of a series of experiments designed to determine the Cepheid distances to galaxies that have produced prototypical supernovae of type Ia. The goal is the calibration of the absolute B and V magnitudes of normal SNe Ia at maximum light and freed of absorption effects. The current Cepheid program is an empirical test of the reliability of SNe Ia as distance indicators for an accurate and unambiguous determination of H_0 (see also Sandage & Tammann 1993). Before turning to calibration issues and a presentation of our analysis techniques, we summarize the scientific results obtained so far.

The first SN to be calibrated in this program was SN 1937C in the parent galaxy IC 4182. Twenty-eight Cepheids were discovered and used for the determination of a reddening-free distance modulus of $(m - M) = 28.36 \pm 0.09$ (Sandage et al. 1992; Saha et al. 1994). Our second target NGC 5253 produced the two SNe 1895B and 1972E. Its distance modulus is $(m - M) = 28.06 \pm 0.06$ (Sandage et al. 1994) based on eleven Cepheids with unambiguous periods. Combining the individual values for the absolute magnitudes of the three type Ia SNe covered by our program so far gives mean values of $\langle M_B(max) \rangle = -19.55 \pm 0.08$ and $\langle M_V(max) \rangle = -19.58 \pm 0.09$.

II. Relevant Calibration Issues

The practical realization of this program consists of several reduction steps (see Labhardt et al. 1993; Saha et al. 1994), some of which involve crucial calibration issues

- preliminary processing in the standard STScI data processing pipeline depends on the reliability of the images used for bias subtraction and flat field correction. The standard flat fields generated from short exposures of the sunlit Earth differ from sky flats recently constructed from long Medium Deep Survey exposures (Phillips et al. 1993 and this volume; Ratnatunga, this volume).
- temporal and spatial variations of the PSF both affect the instrumental photometric zero-point. A meaningful search for variable stars measured at different epochs requires the same photometric scale to be maintained throughout the whole experiment (see next section).

1. Astronomical Institute, University of Basel, CH-4102 Binningen, Switzerland

- zero-point corrections put the instrumental magnitudes on the *HST* photometric system. The nominal zero-point corrections given by Hunter et al. 1992 in the SV Report differ from more recent determinations (Freedman et al. 1993; Phillips et al. 1993).
- the actual distance determination makes use of empirical period-luminosity relations, defined in a ground-based photometric system. This necessitates the transformation of *HST* magnitudes to a standard system like the Johnson-Kron-Cousins system. The transformations given by Harris et al. (1991) are only valid for solar abundances and cover a limited color range.
- the determination of the apparent magnitude at maximum of a SN may include transformation of original photometry to modern systems and fitting of the available data with a standard template light curve.

The Cepheid program aims at obtaining the mean magnitudes of the discovered Cepheids with an overall accuracy of ± 0.10 mag and to determine their periods to 10 percent accuracy. In the following we concentrate on the stellar photometry.

III. Core PSF Photometry

In pursuit of a time-critical observing schedule, repeated images of a field in one of the two target galaxies were taken with the Wide Field Camera in the F555W and F785LP passbands. A summary of the two observing campaigns is given below. The back-to-back exposures were combined to remove cosmic ray events.

Target	Observing Dates	F555W	F785LP
IC 4182	27 Jan – 12 Mar 1992	19 epochs (2 x 4200s) 1 epoch (1 x 4200s)	2 epochs (2 x 4200s)
NGC 5253	31 May – 19 Jul 1993	18 epochs (2 x 3600s) 2 epochs (2 x 2100s)	5 epochs (2 x 3600s)

Two independent teams utilizing different software for crowded-field photometry reduced the aberrated *HST* images and searched for variables. Both groups used an analytical model PSF to fit the dominating core of the severely undersampled WFC PSF. This part of the stellar image contains most of the S/N and is least affected by the variation of the WFC PSF across the field. No effort was undertaken to follow the field dependence of the PSF. Tests performed on images of the LMC cluster NGC 1850 taken during Science Verification with different field positioning and orientation showed that the combined effect of flat field uncertainties and PSF variations is less than 0.07 mag rms. In our experiments, all images were taken in the same telescope position and orientation, so the photometry of any particular star is unaffected by spatial variations of the PSF.

At STScI a variant of DoPHOT (Schechter et al. 1993) for iterative object location and analytic model fitting (elliptical Gaussian profile) was applied. This program also performs object classification. The model parameters were derived for every chip and epoch separately, accounting for the time dependence of the PSF. By correcting for an additive term, the relative instrumental photometry obtained for every star on all the individual images was tied to the photometry of a template image constructed of stacked frames.

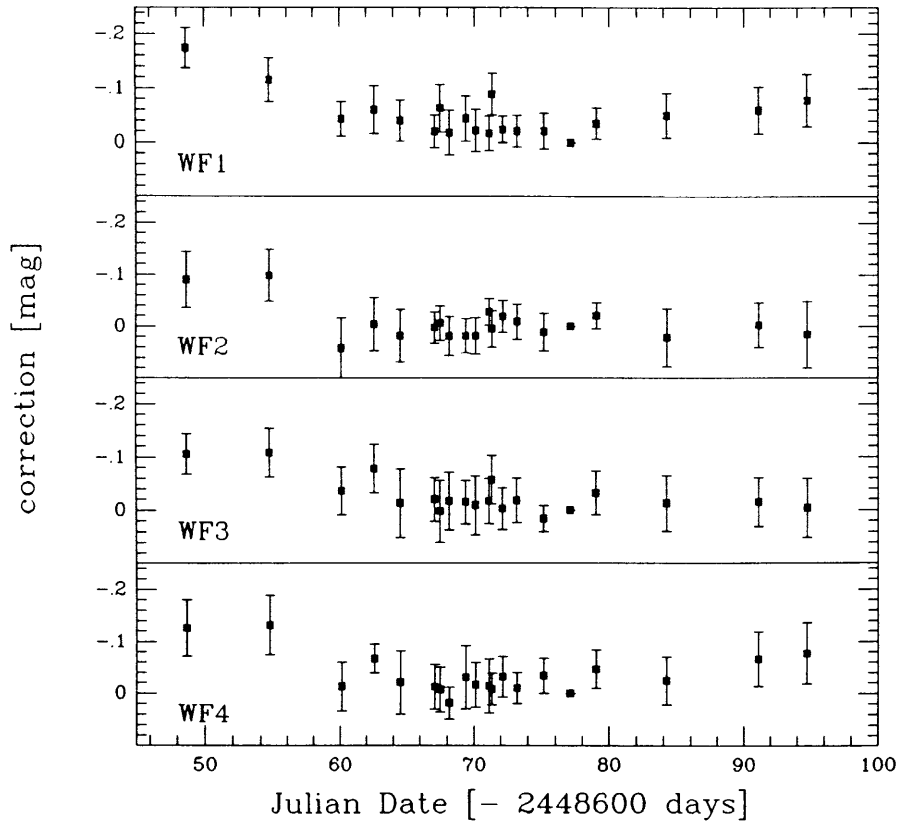


Figure 1: ROMAFOT magnitude corrections for all four chips relative to epoch 16. The values are based on 13 to 25 bright stars from F555W images of IC 4182.

In Basel the ROMAFOT (Bounanno et al. 1979, 1983) package as implemented in the MIDAS environment was used. It performs non-linear best fits of a Moffat function, offers interactive inspection of both the profiles and the residual image, and accepts the subsequent definition of additional stellar components and/or holes for optionally improving the local fit. Object lists generated from coadded images included unwanted spikes due to the aberration problem of the telescope and many spurious events (low-level cosmic rays). The majority of them could be excluded by fitting the PSF with floating parameters and using the resulting profile width as a powerful discriminator to distinguish between stars, extended objects, point like CR hits, and the like. In order to define an average core PSF for each filter and campaign, we examined the few isolated stars available in the least crowded part of the field. The FWHM of the core PSF is typically 1.9 pixels for F555W and 2.1 pixels for F785LP. The adopted PSF was kept fixed for all images. Temporal changes of the PSF were examined by plotting the magnitudes of individual stars versus epoch. In the IC 4182

data we discovered a significant pattern of systematic fluctuations larger than 0.02 mag rms (Figure 1). This is obviously due to the history of decontamination events and focus adjustments which occurred in the course of the first campaign (see MacKenty, this volume). Subsequent correction of all instrumental magnitudes for every epoch and chip/filter combination led to homogeneous instrumental photometry. For IC 4182, the statistical error of the magnitudes, averaged over all epochs, is typically well below 0.10 mag for F555W < 24.5 mag and F785LP < 23.0 mag. In the case of NGC 5253, the errors are larger due to the more extreme crowding.

IV. Zero-Points

The zero-point calibration of the WFC magnitudes depends on the camera, filter, flat field, contamination, and the digital aperture used for the photometry. This part of the calibration process is the most crucial of our program because it strongly affects the accuracy of our distance determination. Two different techniques can be used and checked against each other:

- rely on the work of the IDT (Hunter et al. 1992), and/or
- use independent ground-based observations.

Either direct aperture photometry of truly isolated stars or (partial) growth curves of relatively isolated stars lead to the determination of the actual fraction of detected light covered by the PSF. The full aperture referred to in the SV Report has 80 pixels diameter. The corresponding mean aperture corrections derived for the ROMAFOT magnitudes are given below, normalized to an exposure time of 1 sec.

Target	F555W	F785W
IC 4182	7.42 ± 0.01	7.17 ± 0.01
NGC 5253	7.36 ± 0.02	7.16 ± 0.01

The total magnitudes were calibrated by applying the zero-points given in Table 12.15 of Hunter et al. (1991).

Because more than 1 year has elapsed between the determination of the SV zero-points and the time of our recent observations (NGC 5253), and the last decontamination has taken place in August 1992, we were aware that the telescope photometric system might have changed. Therefore, archived images of two of the regularly monitored calibration stars, taken at a time closest to our data, were reduced. A zero-point correction of -0.14 mag was found for F555W relative to the SV Report. No correction was needed for the F785LP zero-point.

An independent check with ground-based data (J. Tonry, private communication to A. Saha) for 15 uncrowded stars on three of the four WFC chips shows agreement in zero-point between the transformed values and *HST* magnitudes to 0.01 mag in

F555W (by this time corrected from the SV system by -0.14 mag) and -0.03 mag in F785LP.

The *HST* magnitudes obtained independently at Basel and STScI for all stars measured in common are in agreement to within the measuring errors quoted above. The residuals calculated for individual images attest a very consistent determination of the photometric zero-points. Systematic differences amount to only a few hundredths of a magnitude. They become larger at the fainter magnitudes due to unavoidable matching errors that are caused by the different magnitude limits of the object lists generated at STScI and in Basel.

V. Summary and Conclusions

Confronted with the complicated image structure produced by the WFC of the spherical aberration impaired *HST*, crowded-field photometry becomes even more difficult. We relied on a well designed observing strategy and reduction procedures that evolved from those developed for ground-based data. Very reliable photometry down to limits imposed by photon statistics was obtained by fitting an analytic model to the dominating core of the PSF. Spatial variations of the PSF, combined with flat field errors, affect the relative stellar photometry by less than 0.07 mag rms. Images taken at the time of frequent decontamination events and focus adjustments show significant temporal changes of the PSF, that correspond to magnitude offsets of up to 0.15 mag for a given epoch. The determination of aperture corrections depends on the availability of an adequate number of well isolated stars that are bright but do not saturate the chip. Subsequent zero-point calibration of the instrumental total magnitudes was based on the SV Report (Hunter et al. 1992) and/or independent ground-based calibration. Several recent studies revealed discrepancies between the two techniques, caused by an unknown combination of various instrumental effects. However, the overall photometric errors of order of 0.1 mag are acceptable for our scientific program.

In order to overcome the shortcomings in the calibration of WFC images, the following consequences arise

- the flat fields used in the standard data processing pipeline should be replaced by appropriate sky flats,
- the stellar monitoring program should include all chips, and not only one region of a particular chip,
- photometric sequences like the one in ω Cen should be observed regularly and for different telescope position and orientation.

Acknowledgments

I am indebted to all collaborators in this program, especially to Abhijit Saha and Hans Schwengeler. Support was provided in part by the Swiss National Science Foundation.

References

- Buonanno, R., Corsi, C.E., De Biase, G.A., & Ferraro, I. 1979, in *Image Processing in Astronomy*, ed. G. Sedmak, M. Capaccioli, & R.J. Allen (Trieste: Osservatorio Astron. di Trieste), 354
- Buonanno, R., Buscema, G., Corsi, C.E., Ferraro, I., & Iannicola, G. 1983, *A&A* 126, 278
- Freedman, W. L., Hughes, S.M., Madore, B.F., Mould, J.R., Lee, M.G., Stetson, P.B., Kenicutt, R.C., Turner, A., Ferrarese, L., Ford, H., Graham, J.A., Hill, R., Hoessel, J.G., Huchra, J., & Illingworth, G.D. 1994, *ApJ* in press
- Harris, H. C., Baum, W. A., Hunter, D. A., & Kreidl, T.J. 1991, *AJ* 101, 677
- Hunter, D. A., Faber, S. M., Light, R., & Shaya, E. 1992, in *Wide Field / Planetary Camera Final Orbital / Science Verification Report*, ed. S.M. Faber (Baltimore: STScI), chapter 12
- Labhardt, L., Schwengeler, H., & Tammann, G. A. 1993, *ST-ECF Newsletter* 19, 13
- Phillips, A.C, Forbes, D.A., Bershad, M.A., Illingworth, G.D., & Koo, D.C. 1993, Submitted to *AJ*
- Saha, A., Labhardt, L., Schwengeler, H., Macchetto, F.D., Panagia, N., Sandage, A., & Tammann, G.A. 1994, *ApJ* in press
- Sandage, A., Saha, A., Tammann, G.A., Panagia, N., & Macchetto, D. 1992, *ApJ* 401, L7
- Sandage, A., Saha, A., Tammann, G.A., Labhardt, L., Schwengeler, H., Panagia, N., & Macchetto, F.D. 1994, *ApJL* in press
- Sandage, A., & Tammann, G. A. 1993, *ApJ* 451, 1
- Schechter, P.L., Mateo, M., & Saha, A. 1993, *PASP* in press